OPTICAL METAMATERIALS: DESIGN, CHARACTERIZATION AND APPLICATIONS

BY

PRATIK CHATURVEDI

B.Tech., Indian Institute of Technology Bombay, 2004
M.S., University of Illinois at Urbana-Champaign, 2006

DISSERTATION

Submitted in partial fulfillment of the requirements
for the degree of Doctor of Philosophy in Mechanical Engineering
in the Graduate College of the
University of Illinois at Urbana-Champaign, 2009

Urbana, Illinois

Doctoral Committee:

Assistant Professor Nicholas X. Fang, Chair
Associate Professor Paul Scott Carney
Associate Professor Harley T. Johnson
Assistant Professor Xiuling Li

ABSTRACT

Artificially engineered metamaterials have emerged with properties and functionalities previously unattainable in natural materials. The scientific breakthroughs made in this new class of electromagnetic materials are closely linked with progress in developing physics-driven design, novel fabrication and characterization methods. The intricate behavior of these novel metamaterials is interesting from both fundamental and practical point of view. New frontiers are being explored as intrinsic limitations challenge the scaling of microwave metamaterial designs to optical frequencies. These materials promise an entire new generation of miniaturized passive and active optical elements. In this study, I demonstrate an on-fiber integrated "fishnet" metamaterial modulator for telecommunication applications. This metamaterial shows remarkable coupling to fiber guided modes (3.5dB) and a photoswitchable tuning range of more than 1.8dB. The design offers extremely small footprint (~10 wavelengths) and complete elimination of bulk optical components to realize low-cost, potential high-speed optical switching and modulation.

Unique characterization techniques need to be developed as conventional optical microscopy runs out of steam to resolve the fine features of optical metamaterials. To address this challenge, I have investigated cathodoluminescence imaging and spectroscopy technique. This scanning electron beam based technique allows optical image acquisition and spectroscopy with high spectral and spatial resolution. Monochromatic photon maps (spectral bandwidth ~5nm) show strong variation of localized plasmon modes on length scales as small as 25nm. Numerical simulations performed to model the eigenmodes excited by electron beam show strong agreement with experiments.

I also demonstrate progress made in "superlensing", a phenomenon associated with plasmonic metamaterials, leading to subdiffraction resolution with optical imaging. Fabricating a smooth silver superlens (0.6nm root mean square roughness) with 15nm thickness, I demonstrate 30nm imaging resolution or $1/12^{th}$ of the illumination wavelength (near-ultraviolet), far below the diffraction-limit. Moreover, I have extended subdiffraction imaging to far-field at infrared wavelengths. Utilizing a two-dimensional

array of silver nanorods that provides near-field enhancement, I numerically show that subwavelength features can be resolved in far-field in the form of Moiré features. Development of this unique far-field superlensing phenomenon at infrared wavelengths is of significant importance to chemical and biomedical imaging.

In memory of Dada and Jee

ACKNOWLEDGEMENTS

I have been fortunate to be surrounded by many loving people and it is my great pleasure to thank them for their love, support, blessings and encouragement.

First of all, I would like to express my sincere gratitude towards my advisor Prof. Nicholas Fang, for his unending support and valuable guidance throughout the course of my graduate studies. His confidence in my abilities was crucial to smooth my transition from traditional engineering background into the realm of nanotechnology. Without his exemplary vision, optimism and encouragement, this work could not have taken its present shape.

During the course of my graduate studies, I had the opportunity to work with a number of collaborators. I am thankful to Keng Hsu and Anil Kumar for help with fabricating various samples; Hyungjin Ma, and Xu Jun for optical characterization; Kin Hung Fung and Lumerical technical support group for various stimulating discussions on numerical simulations. Special thanks to Dr. James Mabon for help with carrying out cathodoluminescence measurements. I also had the pleasure to work with researchers and collaborators from HP Labs. Dr. Wei Wu, Dr. S. Y. Wang, VJ Logeeswaran provided timely help and support. I am thankful to all other lab members Chunguang Xia, Tarun Malik, Shu Zhang, Ho Won Lee, and Matthew Alonso for providing a friendly work environment. I am grateful to my committee members Prof. Paul Scott Carney, Prof. Harley Johnson, and Prof. Xiuling Li for their valuable time and suggestions.

I am thankful to all my friends who kept me company and made me feel at home in Urbana-Champaign. My parents, my sister, brother and relatives have been a constant source of unconditional love and support all throughout my life. Expressing my gratitude in words towards them is an exercise in futility. Nikki came into my life during the final stages of my PhD; she helped me get past my worries and stood by me during this long process.

Finally I would like to thank all the funding resources DARPA, NSF, and DoE for supporting my research work at University of Illinois.

TABLE OF CONTENTS

1 INTRODUCTION*

1.1 Background and motivation

Over the past eight years, metamaterials have shown tremendous potential in many disciplines of science and technology. Their extraordinary properties and applications has placed them on many scientific-breakthrough lists, including *Materials Today*'s top 10 advances in material science over the past 50 years.[1] The core concept of metamaterials is to scale up conventional continuum materials by using artificially designed and fabricated structural units with the required effective properties and functionalities. These structural units considered as the constituent "atoms" and "molecules" of the metamaterial can be tailored in shape and size, the lattice constant and interatomic interaction can be artificially tuned, and "defects" can be designed and placed at desired locations (Figure 1.1).

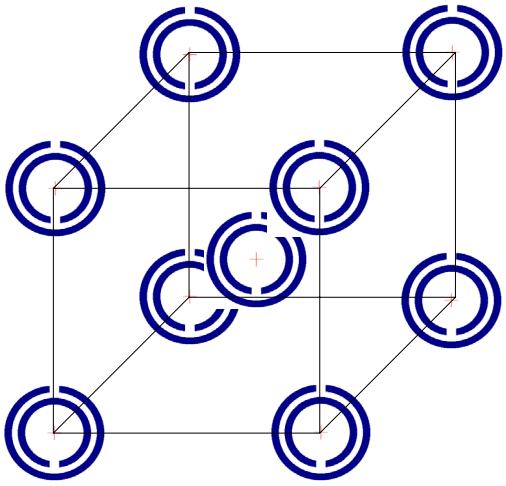

Figure 1.1 Schematic representation of a unit cell of a metamaterial in which artificial "atoms" are arranged in a body-centered-cubic lattice.[2]

Among the most sought-after properties of metamaterials is the negative index of refraction. An engineered material with simultaneous negative electric permittivity (ε)

* Part of the contents of this chapter has been published in MRS Bull. **2008**, *33*, 915-920. Reproduced by permission of the MRS Bulletin.

and negative magnetic permeability (μ) (hence negative index of refraction; $n = -\sqrt{\varepsilon\mu}$) can exist without violating any physical law. These materials show promises of exotic electromagnetic phenomena such as reversed Doppler shift and inverse Cherenkov radiation. All these exciting physics of negative refraction remained merely a mathematical curiosity since Veselago's first prediction in 1968,[3] until negative refraction phenomenon was observed experimentally by Shelby et al. at microwave frequencies in a wedge shaped negative index material (NIM).[4]

Most of the early research to realize negative refraction through metamaterials relied on developing magnetically active materials. Although negative permittivity is quite common in metals at optical wavelengths, it is very challenging to find natural materials that exhibit magnetic response at terahertz (THz) and higher frequencies. This is because magnetic responses in materials arise from either the orbiting electrons or unpaired electron spins. In contrast to electrical resonance or phonon resonance, magnetic resonant phenomena occur at much lower frequencies (typically below 100GHz).[5] However, an artificial composite made up of conductive but non-magnetic swiss rolls[6] or split-ring resonators (SRRs)[4, 7, 8] can display a magnetic response; more surprisingly the composite can exhibit a region of negative magnetic permeability in the frequency spectrum. This SRR array when combined with an array of conducting wires creates a medium with simultaneous negative permeability and permittivity. The origin of magnetic activity in an artificial composite such as SRRs made of purely non-magnetic elements arises from the coupling effect between the structure's internal inductance and capacitance. The coupling alters the impedance to generate a resonance behavior. An external magnetic field with a varying flux normal to the metallic loop induces a current flow, which, in turn, results in a local magnetic dipole moment. This magnetic dipole moment generates magnetization that contributes to the permeability μ (Ampere's law).

Apart from interesting physics and novel electromagnetic phenomena, metamaterials offer opportunities to realize several groundbreaking engineering applications. Subdiffraction imaging,[9] invisibility cloaks,[10] chemical and biomolecular sensing,[11, 12] communication and information processing[13] (Figure 1.2) are some of the applications that have generated enormous interest in metamaterials over a relatively

short period of time. The pressing need to realize these applications has been the driving force in the quest to obtain metamaterials operating at optical frequencies.

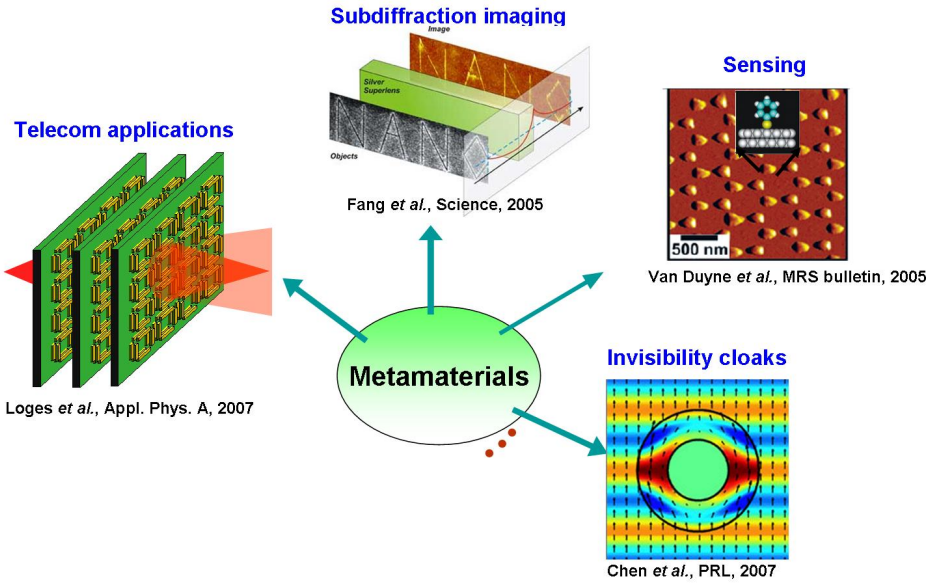

Figure 1.2 A plethora of potential applications such as subdiffraction imaging, sensing, cloaking, and telecommunication has been the driving force in realizing metamaterials at optical frequencies.

Figure 1.3 is an illustrative chart of progress made in scaling artificial magnetism, negative refraction and other novel phenomenon such as subdiffraction imaging to optical frequencies. Ring resonator designs first demonstrated at microwave frequencies have been successfully scaled to mid-infrared (IR) frequencies (e.g. L-shaped resonators operating at 60THz).[14] However, further scaling requires a different approach because of deviation of metal from perfect conductor behavior at higher frequencies.[15] Among the first distinguished designs with near-IR resonant magnetic activity was demonstrated using a wire sandwich structure, in which a dielectric layer is sandwiched between two metal films. The magnetic response in this sandwich configuration originates from the antiparallel current supported by the wire pair.[16] When combined with long metal wires, this structure, popularly known as a "fishnet", was shown to have negative refraction for

a particular polarization at telecommunication wavelength (1550nm). Development of metamaterials operating at telecommunication wavelengths is of significant practical interest as it can lead to novel optical components such as lenses, beam-splitters and optical modulators for fiber-optic communication industry.

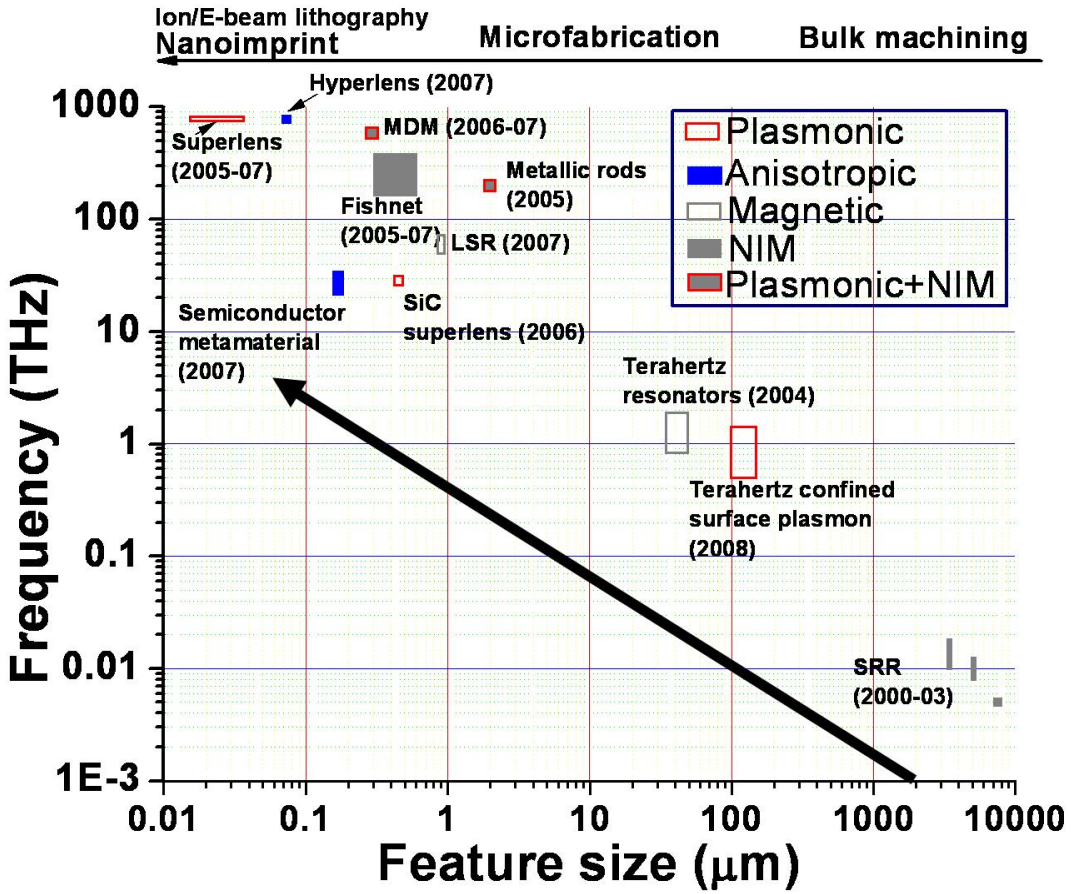

Figure 1.3 Progress made in scaling metamaterials from microwave to optical frequencies. Feature size denotes lattice or unit cell size as appropriate. Suitable fabrication tools corresponding to feature size are listed at the top. *Note:* LSR is L-shaped resonator,[14] MDM is metal–dielectric–metal,[17, 18] SRR is split-ring resonator[4, 7, 8] and NIM stands for negative index materials.

Metamaterials often derive their extraordinary properties from surface plasmon waves which are collective oscillations of free-electrons on the surface of metallic nanostructures. These surface plasmon waves are characterized by their extremely short

wavelength and thus provide a natural interface to couple light to much smaller nanoscale devices more effectively. An entire new generation of metamaterials termed as plasmonic metamaterials operates simply by harnessing properties of resonant surface plasmons. Amplification of evanescent waves,[19] achievement of negative refractive index such as in fishnet metamaterial,[20] extraordinary transmission enhancement,[21] and enhanced Raman scattering[22] are some of the surface plasmons driven phenomena that offer great opportunities for several applications. Optical imaging with subdiffraction resolution, nanolithography, and detection of chemical and biological species with single molecule sensitivity represent some of the possibilities. For example, a planar silver (Ag) film (termed as superlens) is one of the simplest forms of plasmonic metamaterials with an extraordinary ability to beat the diffraction limit through amplification of evanescent waves.[19] Artificial plasmonic metamaterials also offer an opportunity to engineer surface modes over a wide range of frequency by simple surface patterning. Patterning also allows strong confinement and enhancement of resonant plasmon modes compared to flat metal films.[23] These metallic patterns are often utilized in surface-enhanced Raman spectroscopy (SERS) as sensing substrates.

The intricate structure of these novel metamaterials and devices is derived from physics-driven design for desired properties and applications. These designs require development of viable manufacturing and novel characterization techniques. In this dissertation, I have explored the field of optical metamaterials to address three of the most important applications in optical regime, namely telecommunication, optical imaging beyond diffraction limit and chemical sensing. With an exceptional team of experts in the field of plasmonic metamaterials, we set to explore these applications with an integrated approach; starting with fundamental understanding of the physics of metamaterials to developing simulation, fabrication and characterization tools in order to build a continuum picture. The objective of this research is three fold: (1) to develop an integrated metamaterial modulator on an optical fiber for telecommunication applications, (2) to explore cathodoluminescence (CL) spectroscopy as a characterization technique for imaging of plasmonic modes of metallic nanostructures, and (3) to refine the subdiffraction imaging capability of silver superlenses operating in near-ultraviolet

(UV) and develop novel far-field superlenses for near and mid-infrared (IR) frequencies for chemical sensing applications.

The first objective is inspired by an inevitable thrust of research and development in photonics to drive to ever higher levels of integration, eventually leading to a "Moore's Law" for optical information technology, requiring the exponential growth of information processing functions such as modulating and switching at small scales. A significant roadblock towards that goal is the size and cost of discrete optical components. In this research, we explore novel concepts of metamaterials to address these ultimate demands. We have investigated the fishnet metamaterial design and its possible integration on to an optical fiber to develop a lightweight, compact and efficient telecommunication modulator.

The second objective sets to explore the properties of plasmonic metamaterials using CL imaging and spectroscopy. This part of the research addresses the pressing need to develop unique characterization techniques for the analysis of subwavelength and complex metastructures. Existing characterization methods ranging from optical microscopy to near-field scanning optical microscopy (NSOM) do not offer the flexibility of characterizing optical metamaterials with features on the order of sub-10s of nanometers. On the other hand CL, a scanning electron beam based characterization technique offers an opportunity to investigate these structures with unprecedented resolution. This investigation is critical to fully understand and exploit the properties of metal nanostructures.

The third objective deals with one of the most promising applications of metamaterials; their ability to obtain images that are diffraction free. Inspired by recent work on superlens imaging[9] we set to explore the ultimate limit of subdiffraction imaging with silver superlenses. While these superlenses are limited to providing subdiffraction images only in the near-field, we have explored an imaging approach based on Moiré effect that allows subdiffraction resolution in the far-field at IR frequency range. This frequency range is of special interest to chemists and biologists who utilize IR imaging tools such as Fourier-transform infrared imaging (FT-IR) and spectroscopy to detect trace amounts of chemicals and malignancy in biological cells and tissues. The development of

a parallel far-field optical imaging tool with subdiffraction resolution could have a profound impact in chemical sensing and medical diagnostics.

1.2 Thesis organization

This dissertation is organized into 5 chapters. Besides this introductory chapter which is intended to provide a brief background and outline of the study, the contents of rest of the chapters are organized as follows.

Chapter 2 discusses the development of "Integrated metamaterial modulator on optical fiber" for telecommunication. We have investigated the fishnet metamaterial as an optical modulator for on-fiber communication and information processing applications. The design offers small footprint (~10-20λ, where λ is free-space wavelength) and integration on fiber eliminates the need for bulk optical components. Numerical studies indicate 3.5dB in transmission dip due to coupling of fiber guided modes with that of the metamaterial and an on/off ratio of 1.8dB for the integrated modulator. We have also investigated a "flipped fishnet" geometry that shows low loss and stronger coupling with fiber-guided modes.

Chapter 3 presents "Imaging of plasmonic modes of nanostructures using high-resolution cathodoluminescence spectroscopy". Most of the prevalent optical metamaterial designs are based on nanostructures made of noble metals such as silver and gold. To investigate the optical properties of such structures, we have performed CL spectroscopy on silver nanoparticles in a scanning electron microscopy setup. Direct excitation and emission of decoupled surface plasmon modes is observed with panchromatic and monochromatic imaging techniques. Monochromatic emission maps have been shown to resolve spatial field variation of resonant plasmon mode on length scale smaller than 25nm. Finite-difference time-domain numerical simulations are performed for both the cases of light excitation and electron excitation. The results of radiative emission under electron excitation show an excellent agreement with experiments. A complete vectorial description of induced field is given, which complements the information obtained from experiments.

Since its conceptualization[24] superlens has received great deal of attention from the scientific community owing to its superior imaging capabilities with subdiffraction resolution. Theoretically, the device is capable of λ/20 - λ/30 image resolution[25, 26]. However, after the first demonstration of λ/6 imaging (60nm resolution)with a silver superlens,[9] no further improvement in resolution has been reported so far, mainly because it requires fabrication of thin, ultra-smooth silver film, which presents a daunting challenge owing to island forming tendencies of silver.[27] In Chapter 4, we show a smooth superlens (~0.6nm root mean square roughness) can be fabricated down to 15nm thickness. Utilizing an intermediate wetting layer germanium for the growth of silver, we experimentally demonstrate 30nm or λ/12 optical imaging resolution at near-UV wavelength. Moreover, we have conceived a novel far-field subdiffraction imaging scheme at IR wavelengths. Utilizing a plasmonic material consisting of array of silver nanorods, we numerically demonstrate that subwavelength information from an object can be coupled out to the far-field in the form of Moiré features. A simple image reconstruction algorithm can then be applied to recover the object with subwavelength resolution. Realization of such a far-field superlens opens up exciting avenues for biomedical imaging and chemical analysis.

Finally, Chapter 5 provides the summary of the work presented in this dissertation and gives an outlook on possible future directions.

2 INTEGRATED METAMATERIAL MODULATOR ON OPTICAL FIBER

2.1 Introduction

In the quest for fast, efficient and compact photonic devices, metamaterials have been demonstrated as promising candidates for optical modulation.[13, 28, 29] These artificial materials consisting of discrete set of metal-dielectric composite structures have been shown to mimic the properties of bulk materials.[7, 28] These discrete elements can be designed to achieve a desired response in a frequency range not readily accessible with natural materials. In particular, the response can be tuned optically or electrically by including active elements in the structural unit. For example, excitation of charge carriers in a constituent semiconductor layer or the substrate can lead to modulation of optical properties such as effective refractive index and resonance frequency of the metamaterial. The inherent resonant nature of the metamaterial response enhances the effect of active elements. Moreover, since the structural unit of metamaterial can be very small compared to wavelength, the realization of compact photonic devices only several wavelengths in footprint is a distinct possibility. This has generated considerable interest over the past few years in the research community to develop active metamaterial devices. An early breakthrough in the field came in 2006 when Chen and colleagues demonstrated a resonant metamaterial modulator[29] with tunable properties to an applied bias potential. Using gold split-ring resonators (SRR) on a thin semiconductor substrate a tunable optical response was achieved in the terahertz regime. With nominal voltages (~16V), transmission at resonance was modulated by as much as 50%. With metamaterial removed, the substrate by itself showed less than 10% modulation.

These active metamaterial devices find tremendous potential in telecommunication and fiber-optic systems. While SRR design shows a strong promise as a terahertz modulator, however, fiber-optic systems require devices operating in near-infrared (IR) wavelengths. Scaling SRR to optical frequencies and obtain photoconductive switching in IR is extremely challenging fabrication-wise, as it requires very small structural dimensions. Furthermore, linear scaling of resonant wavelength of SRR design with its structural dimensions breaks down and resonant response starts to

saturate near optical frequencies.[15] This happens because of deviation of metal from perfect electric conductor behavior at higher frequencies.

New designs capable of operating at near-IR and even visible frequencies are being explored.[30] Among the first distinguished designs of metamaterial operating in near-IR regime is a metal-dielectric-metal sandwich structure (Figure 2.1 *inset*). This sandwich structure arranged in the form of cross-wires is popularly known as fishnet metamaterial.[16] This metamaterial can be designed to have simultaneous negative values of magnetic permeability (μ) and electric permittivity (ε); a feature leading to negative refractive index. The design has recently been successfully scaled to bulk three-dimensional configuration as well.[31] Relative ease of fabrication, operation in near-IR frequency range, and metal-dielectric composite structure which allows switching by modulating the dielectric layer, makes this design a promising candidate for optical modulation.[32] Although the metamaterial itself is small in size (~10-20λ, where λ is free-space wavelength), optical fiber communication systems require several bulk components (e.g. lenses, alignment optics etc.) to couple light out of a fiber into the modulator and then back into the optical fiber (Figure 2.1(a)). Correspondingly, the free space propagation introduces additional losses and noise into the signal. Optical amplifiers are often required to compensate for these losses.

In this work, we demonstrate that a metamaterial modulator can be integrated directly to an optical fiber, thus eliminating the need for bulk optical components. The modulator design is based on silver (Ag)-silicon (Si) -silver fishnet structure (Figure 2.1(b)) that allows modulation in near-IR frequency range with photoexcitation of carriers in silicon layer. Our numerical studies indicate that fiber-guided modes couple strongly to the fishnet metamaterial near its magnetic resonance frequency. Hence, a dip is observed at the resonant wavelength in fiber transmitted output (off state). Upon optical excitation of silicon layer, the resonance frequency of fishnet is detuned, and thus the optical signal is guided by the fiber (on state). Simulations indicate optical modulation with on/off ratio of 1.8dB or 0.1dB per micron length of modulator is feasible with this design. As a necessary precursor to the operation of integrated fiber modulator, we have conducted experimental studies with near-field scanning optical microscopy (NSOM) in total internal reflection configuration. These measurements suggest coupling

of evanescent modes to the metamaterial at resonance and are in good agreement with simulations. While fishnet metamaterial is an effective free-space modulator, the integrated modulator shows reduced efficiency due to oblique angles of incidence under fiber-guidance. To optimize the integrated modulator, we have investigated a "flipped fishnet" geometry which shows improved performance at oblique angles of incidence. This design promises to be a low loss and efficient integrated modulator.

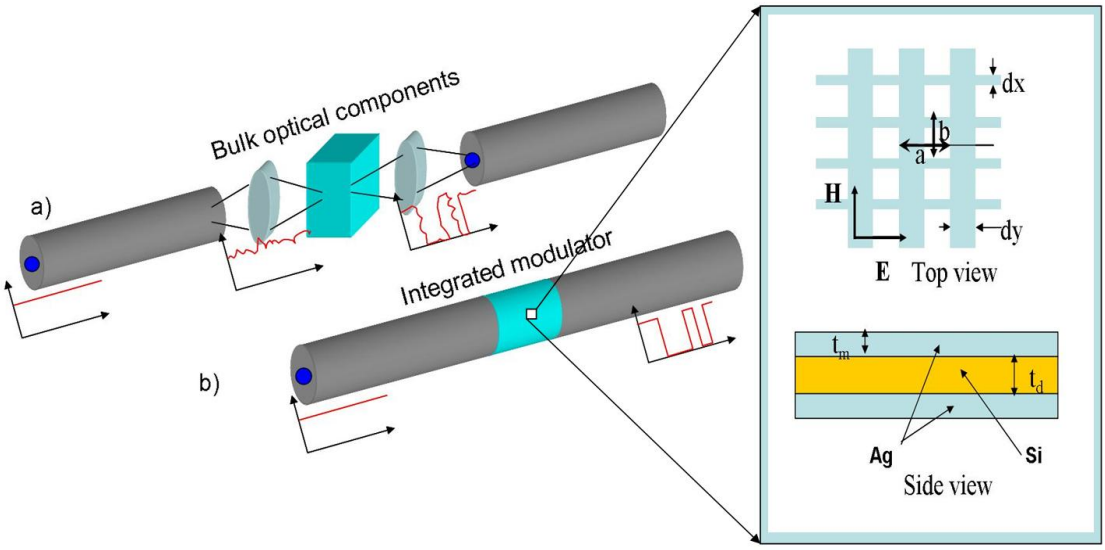

Figure 2.1 (a) Conventional fiber-optic communication systems require bulk optical components such as lenses, modulator and amplifiers to generate and transport information. **(b)** An integrated modulator design eliminates the need for bulk components. *Inset zoom:* Schematic of Ag-Si-Ag fishnet structure. Vector **H** and **E** denote the directions of magnetic and electric field respectively.

2.2 Free-space fishnet metamaterial modulator

To design an integrated fiber-optic modulator based on fishnet metamaterial, we first investigate the free-space modulation effect. Full scale three-dimensional numerical simulations are performed to obtain the geometric parameters of Ag-Si-Ag fishnet metamaterial and its performance as an optical modulator. The computations are performed using a commercial software package CST Microwave Studio. A computational grid with 12 mesh points per wavelength is utilized. Silver is modeled as a

dispersive lossy metal with permittivity governed by Drude model, whereas Si is modeled as a non-dispersive lossless material with ε =11.9. The structure is embedded in free-space and is excited by waveguide simulator, which allows modeling of the free-space problem as a bounded simulation.[33] The normal incidence transmission and reflection characteristics (S-parameters) of the metamaterial are plotted in Figure 2.2(a), (b). Reflection shows a strong dip at 1760nm, which is attributed to excitation of magnetic resonance. To better understand the nature of this resonance, field distribution is plotted in the metal strips and the enclosed dielectric (Figure 2.2(c)). The color map indicates the strength of the magnetic field at resonance. It is evident that strong magnetic field is concentrated in the dielectric and is negative with respect to the incident field, suggesting a negative magnetic permeability at resonance. This magnetic response of the structure arises due to a displacement current loop as illustrated by the electric field arrow plot. The conduction current density (small compared to displacement current) in the two metal strips is oppositely directed, thus forming a current loop and generating a magnetic resonance. At magnetic resonance, the structure assumes simultaneous negative values of magnetic permeability and electric permittivity and hence the structure is better impedance matched to surroundings ($Z(\omega) = \sqrt{\mu(\omega)/\varepsilon(\omega)}$, where Z represents impedance at frequency ω). This leads to a dip in reflection as observed at 1760nm. However, away from resonance, magnetic permeability achieves positive values while electric permittivity is still negative. This causes a large impedance mismatch and therefore transmission achieves a minimum (observed at 1780nm in Figure 2.2(a)).

The spectral location and quality factor of this resonance is strongly dependent on the complex refractive index of the sandwich layer and this is central to the function of fishnet metamaterial as an optical modulator. For example, the refractive index of Si layer can be modulated by utilizing a plasma-dispersion effect, thereby detuning the resonance wavelength and achieving optical modulation.

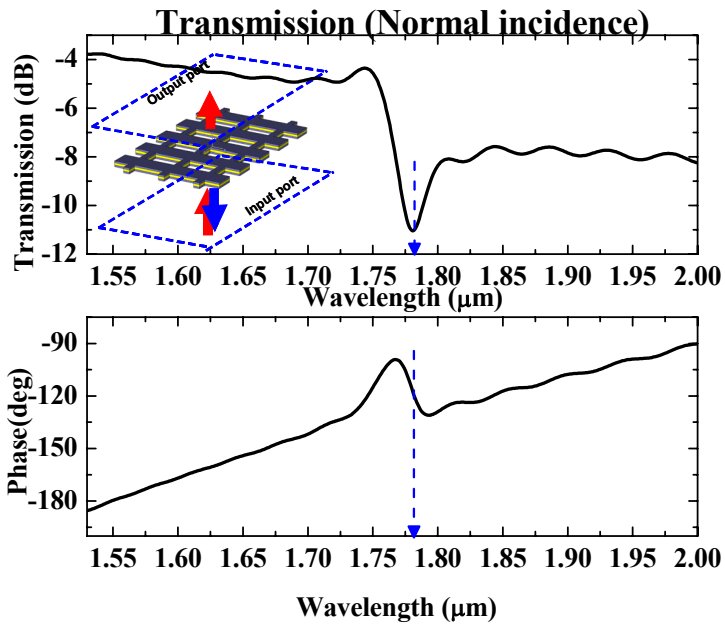
Transmission (Normal incidence)
Transmission (dB)
-4
-6
-8
-10
-12
Output port
Input port
1.55 1.60 1.65 1.70 1.75 1.80 1.85 1.90 1.95 2.00
Wavelength (μm)
Phase(deg)
-90
-120
-150
-180
1.55 1.60 1.65 1.70 1.75 1.80 1.85 1.90 1.95 2.00
Wavelength (μm)

(a)

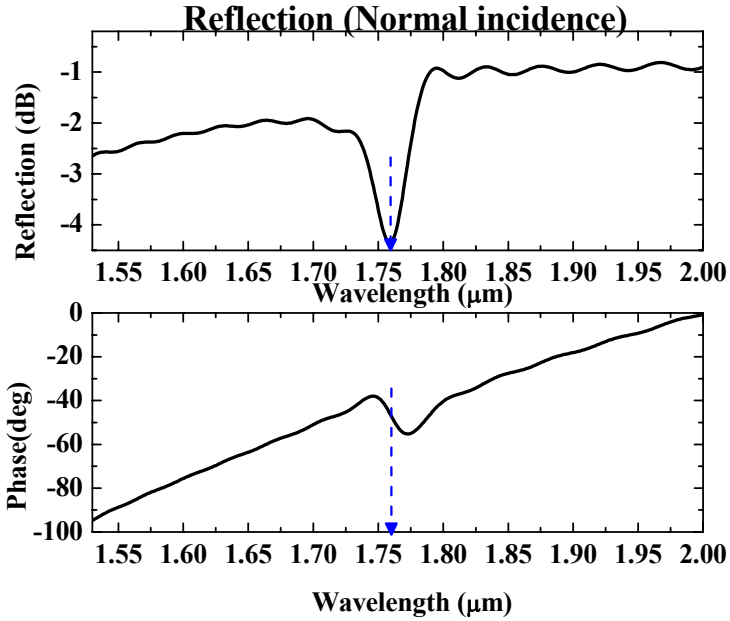
Reflection (Normal incidence)
Reflection (dB)
-1
-2
-3
-4
1.55 1.60 1.65 1.70 1.75 1.80 1.85 1.90 1.95 2.00
Wavelength (μm)
Phase(deg)
0
-20
-40
-60
-80
-100
1.55 1.60 1.65 1.70 1.75 1.80 1.85 1.90 1.95 2.00
Wavelength (μm)

(b)

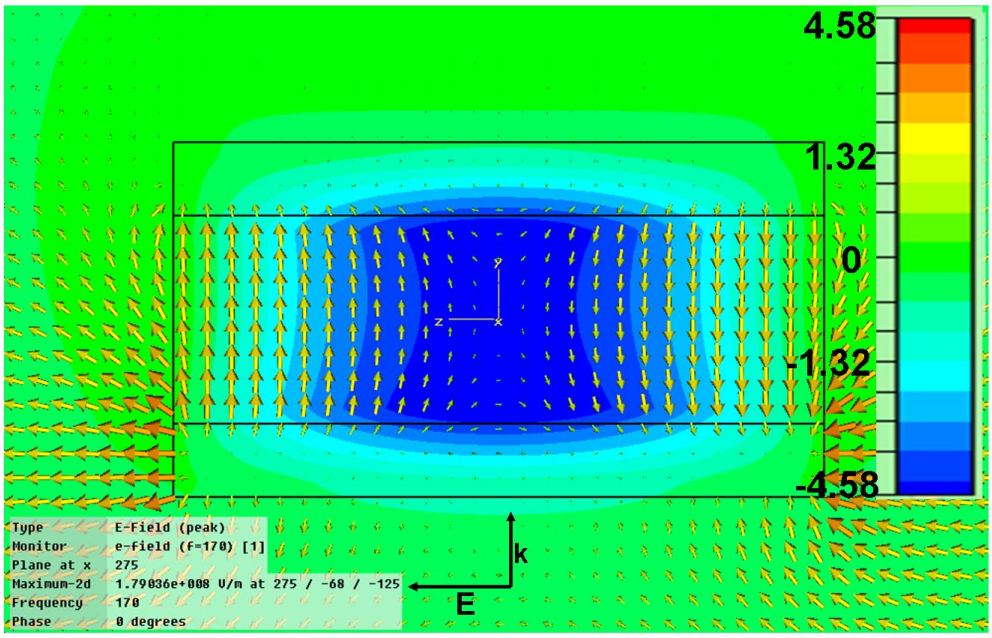

(c)

Figure 2.2 (a) Normal incidence transmission amplitude and phase characteristics of Ag-Si-Ag fishnet structure (Inset). **(b)** Reflection characteristics. **(c)** Field map within the metal-dielectric-metal sandwich structure at resonant wavelength of 1760nm. The color represents magnetic field (**H**) normalized with respect to incident magnetic field, and the arrows represent electric field (**E**) distribution. The incident wave polarization is as indicated and the dimensional parameters of the fishnet structure as illustrated in Figure 2.1 are t_m = 28nm, t_d = 80nm, dx = 108nm, dy = 250nm, a = b= 550nm.

To investigate the performance of this structure as a free-space optical modulator, simulations are performed where a pump beam induced modulation in the refractive index of Si is assumed and transmission characteristics of fishnet are computed (Figure 2.3(a)). It is observed that by modulating the refractive index of Si by just 1.7%, transmission is modulated by 6dB (75% change) and phase undergoes a shift of 35 degrees (Figure 2.3(b)). In comparison, an equally thick Si layer by itself undergoes a transmission modulation of less than 0.2dB (4%). It should be noted that this calculation is performed for just one fishnet layer. This implies that by stacking 5 layers of this sandwich structure one can build a Mach-Zehnder interferometer with a total interaction

length of just 680nm, an order of magnitude smaller than other nonlinear materials. It is worth mentioning here that the aforementioned amount of index change in Si layer can be achieved with ~320μJ/cm^2 of pump fluence.[32]

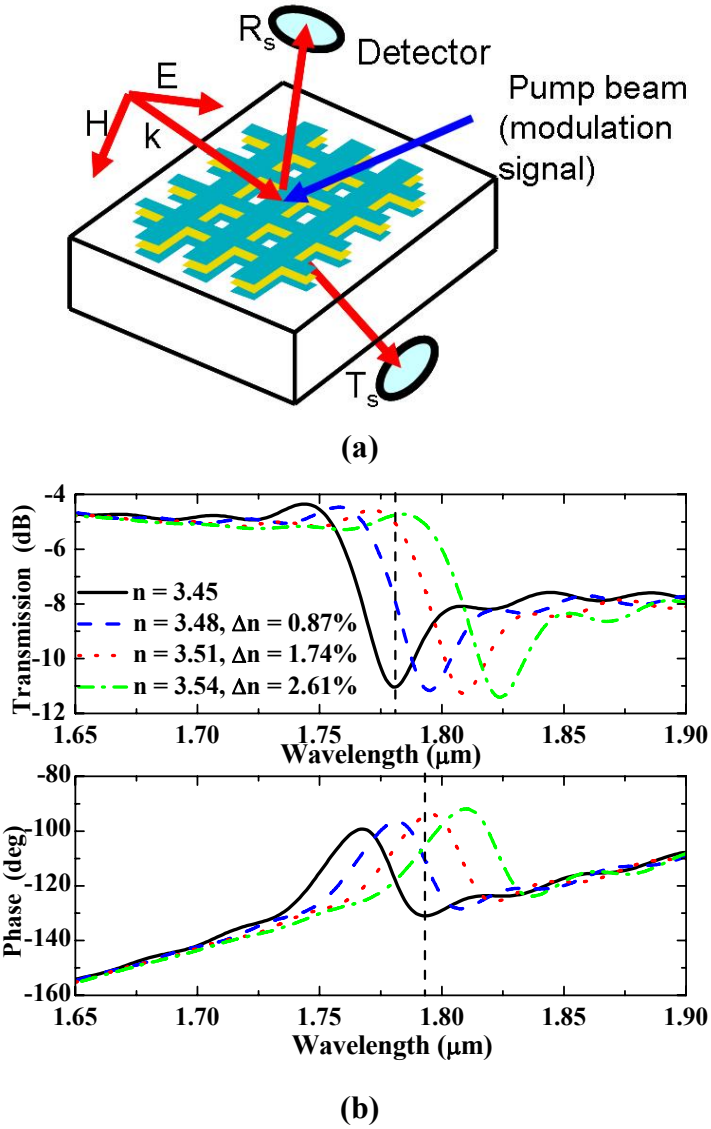

Figure 2.3 (a) Schematic illustration of free-space fishnet modulator. A pump beam induces a change in refractive index (n) of Si layer. **(b)** Simulated change in transmission characteristics of fishnet as the index of Si layer changes.

These simulations strongly indicate that fishnet metamaterial design can be an efficient and compact stand-alone component. However, to build an optical modulator for

fiber-optic communication systems would require several other bulk components which to a certain extent nullifies the advantages of a having a compact central unit. By integrating the modulator directly onto the fiber, we eliminate the bulk optical components, leading to significant cost reduction. This integrated design offers smaller footprint, low loss, high efficiency, self-alignment and is less prone to electromagnetic interference.

2.3 Integrated fishnet metamaterial modulator

Figure 2.4(a) illustrates the conceptual description of fishnet optical modulator made on side-polished fiber. By fabricating this modulator onto a fiber flat (after removal of a section of the fiber's cladding) permits evanescent interaction of guided modes of the fiber with the device. An external optical modulation signal, thus allows the possibility of modulating transmitted output signals from the fiber. Fishnet metamaterial was fabricated using focused ion beam (FIB) milling (Figure 2.4(b)) onto the flat side of a commercially available D-shaped fiber (Source: KVH industries).

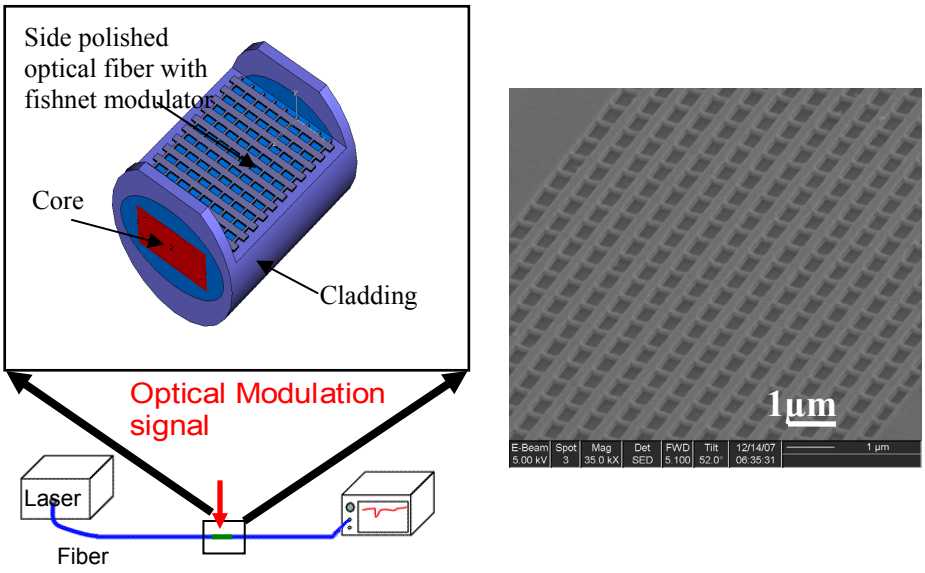

(a) **(b)**

Figure 2.4 (a) Sketch of fishnet modulator on polished optical fiber. **(b)** Secondary electron image depicts fishnet metamaterial fabricated onto a single D-fiber.

This integrated design is based on mode coupling between fishnet and fiber guided modes. We have simulated this coupling effect by placing the fishnet onto a fiber and monitoring the trans-coupled output (Figure 2.5(a)). Figure 2.5(b) shows the transmission (red dashed line) and reflection (blue dotted line) characteristics of a fishnet designed to be resonant near 1500nm (reflection dip). It is observed that near the metamaterial resonance, light is coupled into the fiber through surface modes and is guided by it; hence we observe a peak in the trans-coupled output spectrum (black solid line). To further verify if this is truly a resonant mode of the metamaterial and not a diffracted mode, we have simulated an identical grating structure but without the intermediate dielectric layer. This simple metal grating structure shows no resonant coupling effect (Figure 2.5(c)).

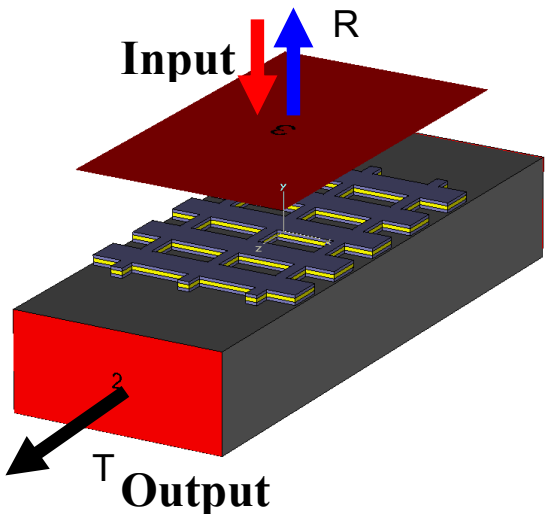

(a)

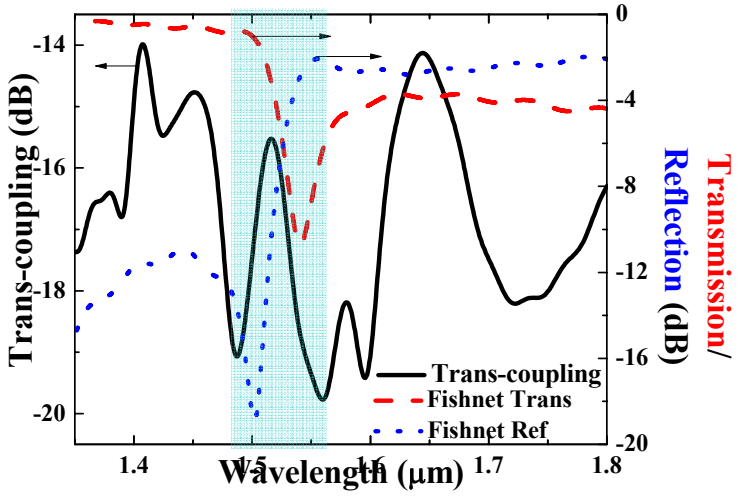

(b)

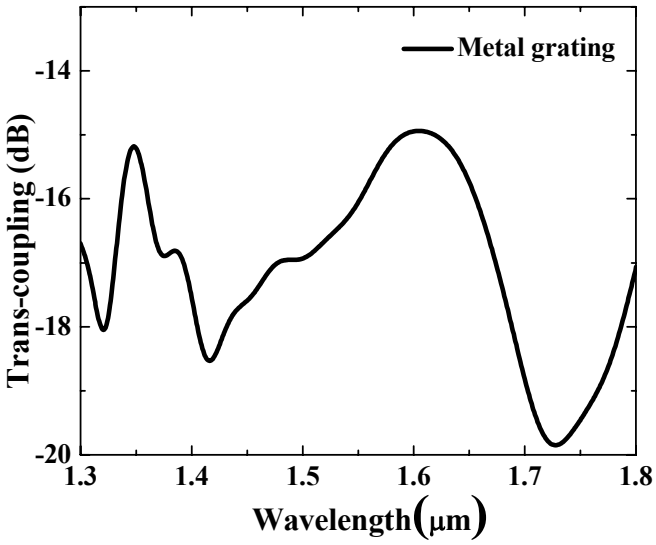

(c)

Figure 2.5 (a) Simulation setup for investigating trans-coupling between fishnet and fiber guided modes. The fiber is modeled with permittivity ε = 2.1786. **(b)** Simulated trans-coupling output shows a peak near the resonant wavelength of fishnet metamaterial (marked with a box as a guide). The transmission (red dashed line) and reflection (blue dotted line) characteristics of the metamaterial in free-space are also depicted. **(c)** Trans-coupled output when the metamaterial is replaced with an identical metal grating structure. In this case no resonant peak is observed suggesting that the diffracted modes are not coupled to the fiber.

Light guided by a fiber interacts with fishnet only in the form of evanescent modes. To experimentally investigate this near-field interaction, we have carried out NSOM measurements under total internal reflection configuration. Figure 2.6(a) illustrates the experimental setup; incident light is totally reflected at the interface of glass and fishnet metamaterial. Only evanescent modes interacting with the fishnet are collected by NSOM probe. The probe is scanned across the sample with an average height of 50nm above the surface. Figure 2.6(b), (c) shows fishnet topography and optical image acquired at 1550nm illumination wavelength, respectively. Corresponding near-field simulated intensity 50nm above the surface of fishnet is shown in Figure 2.6(d). It is indeed observed that the evanescent light is coupled to the resonant mode of the metamaterial, as the optical image shows similar field distribution as the simulated near-field distribution at the resonant wavelength. Both plots show large photon counts in the hole regions of the metamaterial. These high intensity regions are connected along the direction of thick metal strips which are resonant at 1550nm.

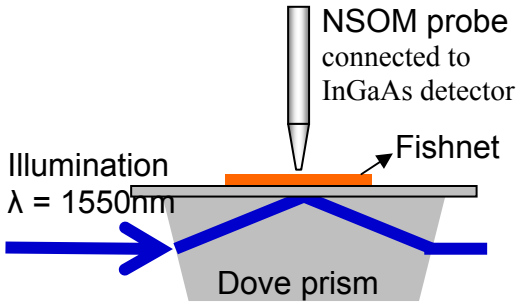

(a)

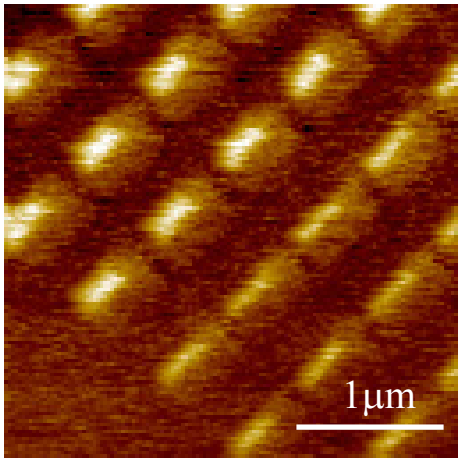

(b)

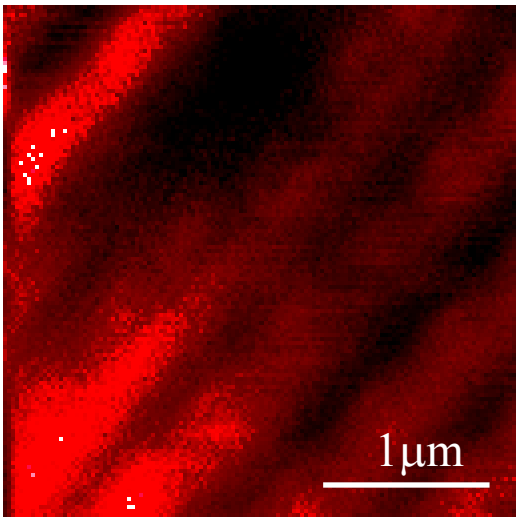

(c)

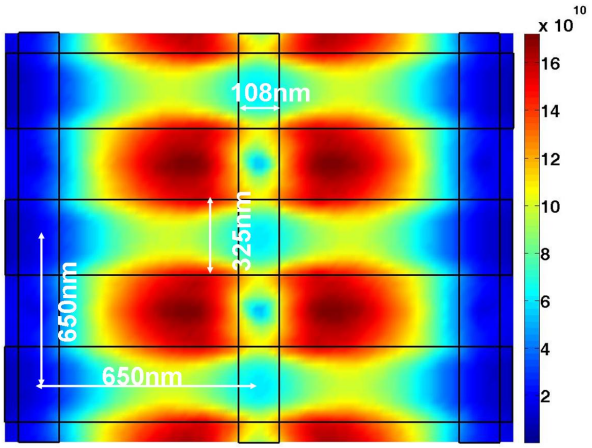

(d)

Figure 2.6 (a) Schematic illustration of NSOM measurements performed on fishnet metamaterial in total internal reflection configuration. **(b)** Topographic image (bright regions represent holes, dark areas are metal strips) **(c)** NSOM optical image **(d)** Simulated near-field at the resonant wavelength (metal strips are marked by black lines for clarity).

2.3.1 Numerical simulations based on effective medium model

It is to be noted here that the full-scale electromagnetic simulation methodology as described above is computationally very intense, especially for integrated modulator

geometry. To reduce this computational load and investigate the performance of integrated fiber modulator, we utilize homogenization approximation for the metamaterial. In this approximation, the metamaterial is considered as a fictitious homogeneous film with macroscopic optical parameters ε and μ. These quantities are retrieved such that they have the identical complex transmittance and reflectance properties to that of the actual nanostructured metamaterial.[34] This approximation allows a reduction in the dimensionality of the design problem while carrying the essential physics with reasonable accuracy. With this approximation, the integrated fiber-modulator geometry can be greatly simplified to a stratified configuration (Figure 2.7). For the purpose of this study, we have utilized the effective medium properties of fishnet metamaterial (ε_{eff}, μ_{eff}, n_{eff}) as derived by Wu et al.[35] The parameters used in computation are shown in Figure 2.8. The fiber core (germania doped silica in D-shaped fiber) is modeled as a semi-infinite planar material with $\varepsilon = 2.1786$, $\mu = 1$. In fabricated sample, there is usually a thin cladding layer separating the fiber core and fishnet metamaterial which has been neglected for the sake of simplicity. We utilize the transfer-matrix method based on the Fresnel transmission and reflection coefficients to obtain the ω(k) dispersion plot.

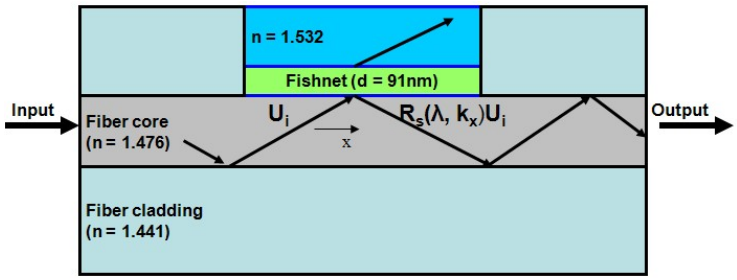

Figure 2.7 Schematic illustration of fishnet modulator geometry used in dispersion study. U_i denotes the incident field, and R_s represents the reflection coefficient for S-polarized light. Initial experiments were performed with fishnet fabricated on glass (n = 1.532) and brought into contact with fiber.

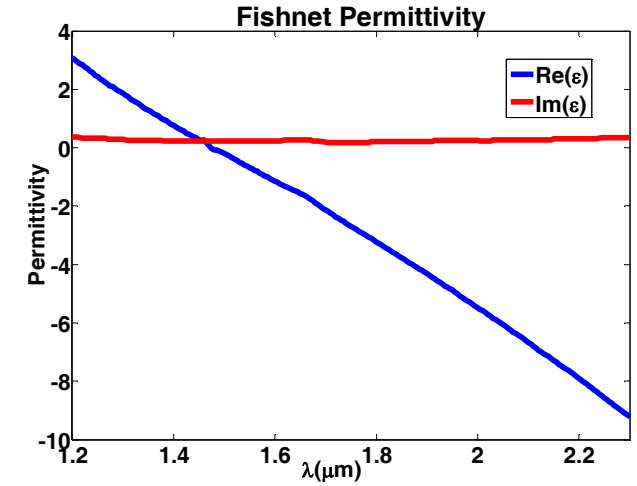

(a)

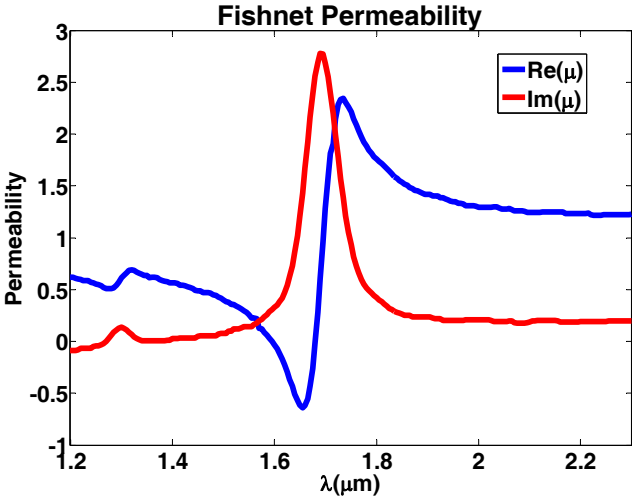

(b)

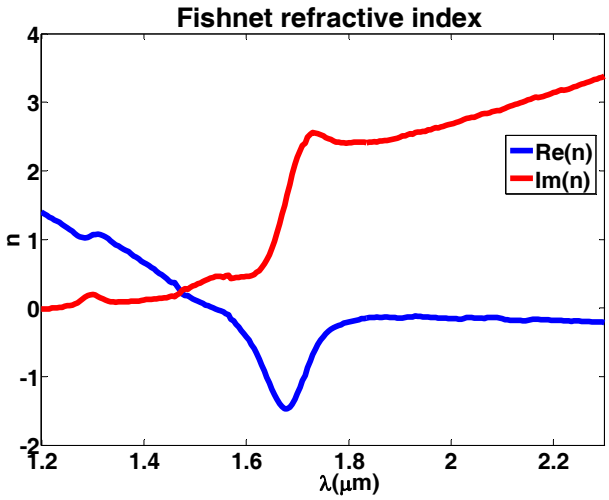

(c)

Figure 2.8 Effective medium parameters for fishnet metamaterial **(a)** Permittivity ε, **(b)** Permeability μ and **(c)** Refractive index n, obtained from Ref. 35.

Figure 2.9(a) shows the dispersion diagram for S-polarized light (TE mode). The color scale represents the reflected intensity (in dB). Based on critical angle of guidance for D-fiber ($\theta_c = 77.5^0$) and its core diameter (2μm, along the shorter axis), we estimate that guided modes suffer one reflection bounce per 18μm of fishnet interaction length. Hence, the single bounce dispersion diagram directly corresponds to the fiber output when the modulator interaction length is <18μm. This dispersion plot tells some key features of this integrated modulator. With small angle of incidences, the resonance of the metamaterial is very sharp and strong. However under steep angles of incidences, as is the case with fiber guidance, the resonance is relatively broad and weak. It should be noted that only the modes with $k_x > 1.441k_0$ are guided by the fiber core due to total internal reflection from cladding. Figure 2.9(b) shows the reflected intensity for such a guided mode ($k_x = 1.46k_0$). This plot clearly shows that the coupling of the fiber guided mode to the resonant mode of the metamaterial is ~3.5dB.

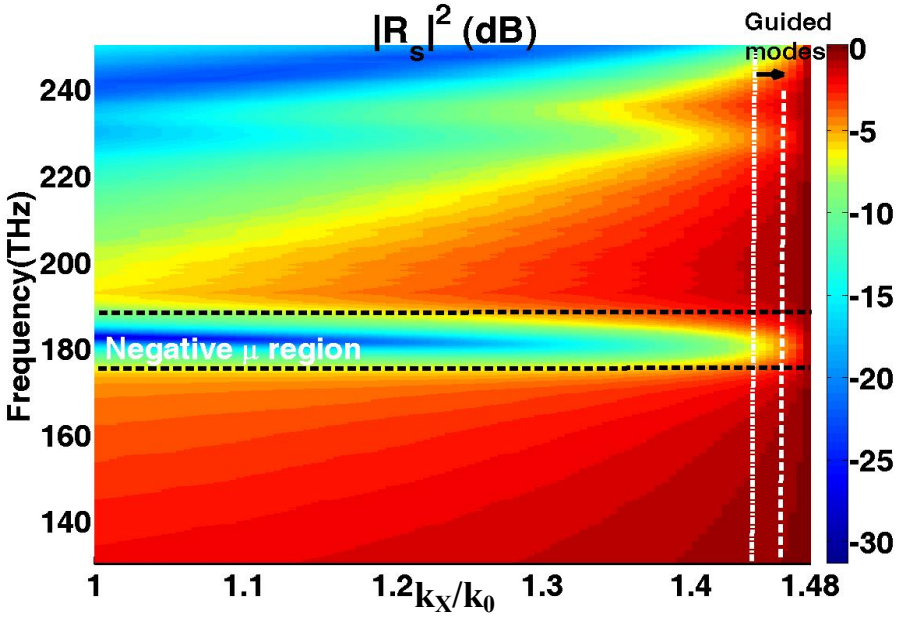

(a)

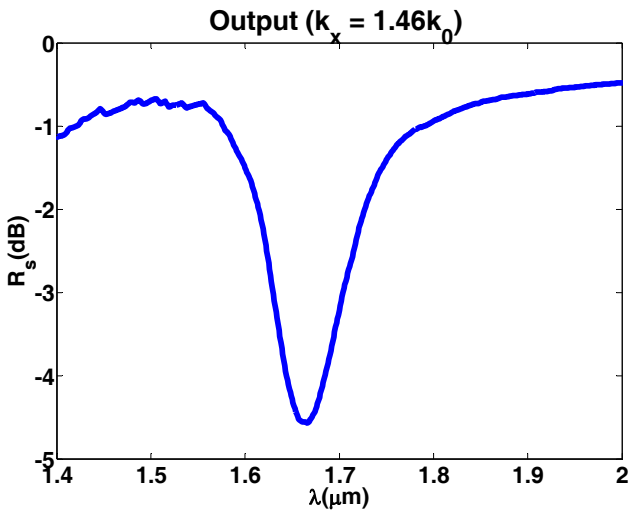

(b)

Figure 2.9 (a) Dispersion plot for reflected intensity (output). **(b)** Output for a particular guided mode shown by white dashed line in (a) (k_x= 1.46k_0)

Optical modulation of the effective properties of the fishnet metamaterial can be accomplished with Ag-Si-Ag heterostructure by photoexcitation of carriers in Si layer. The resonant nature of the structure allows modulation of the effective refractive index by as much as 40% with small changes in Si refractive index (~1.7%) as indicated by free-space simulations shown earlier. Based on these results we investigate the modulation of output intensity through the fiber when the effective index of fishnet is changed due to carrier excitation in Si layer. Figure 2.10(a) shows one such case of modulation of effective properties of fishnet that can be achieved with pumping the Si intermediate layer with visible light. Figure 2.10(b) shows the modulation of output intensity for the guided mode (k_x= 1.46k_0) with pumping. Modulation depth of 1.8dB (per reflection bounce) is observed at the resonant wavelength.

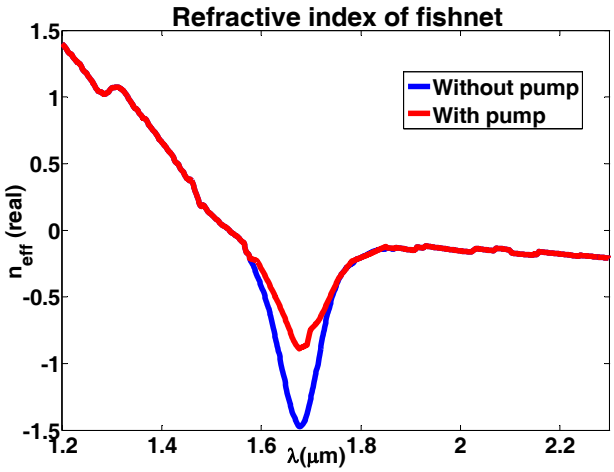

(a)

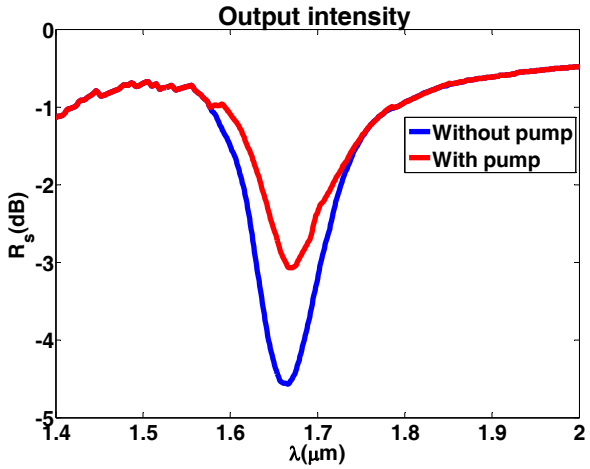

(b)

Figure 2.10 (a) An example case of modulation of effective refractive index of fishnet metamaterial. **(b)** Modulated output from the fiber when the effective index of fishnet is changed with pumping.

2.4 Towards improving modulator performance

In the previous sections, we have demonstrated the operation of integrated fiber modulator based on fishnet metamaterial. While on one hand the design offers extremely small footprint, it has certain drawbacks. First, the fiber guided mode couples weakly to the resonance mode of the metamaterial compared to free-space coupling and second, relatively moderate modulation depths. Under fiber-guidance light is incident on the metamaterial at steep angles, and this reduces the resonance strength as some diffracted

modes start to propagate through the metamaterial. This is evident from dispersion plot in Figure 2.9(a) which shows the reduction in resonance strength as the angle of incidence increases ($\theta = \sin^{-1}(k_x / nk_0)$, where θ is the angle of incidence and n is the refractive index of fiber core). Resonance strength is also low because of losses in the metamaterial which is also responsible for broadening of resonance. Modulation depth is rather limited because of the fact that the switching layer is buried underneath a metal film which requires relatively higher pump intensities to bring the modulation effect. In following sections, we address these issues and demonstrate that a "flipped fishnet" design is better suited as an integrated fiber modulator.

2.4.1 Losses, integration of gain material and flipped fishnet for enhanced modulation

One of the most fundamental challenges with the prevalent designs of metamaterials is the presence of losses. These losses originate from intrinsic absorption of constituent materials, specifically metals which are highly lossy at optical frequencies. Resonant nature of the metamaterial and topological effects such as surface roughness also contributes to the losses. These losses severely hinder the performance of metamaterials and restrict their range of practical applications. One of the approaches to compensate loss is inclusion of an optically pumped gain media.[36] Gain media can be incorporated in close proximity of the metamaterial or can be an integral layer of the metamaterial itself. The former approach was investigated theoretically and experimentally where an $In_{0.786}Ga_{0.214}As_{0.465}P_{0.535}/In_{0.53}Ga_{0.47}As$ quantum well structure was used as a substrate providing gain (gain coefficient, $g = 3000cm^{-1}$) to the fishnet metamaterial fabricated on top.[37] It was observed that even at a nominal gap of 20nm (in the form of a spacer layer) between the gain media and fishnet metamaterial, the gain had a very little effect (<2%) on the properties of the metamaterial. This is because electromagnetic field is concentrated mainly inside the dielectric layer of the fishnet structure (in between the metal wires, see Figure 2.2(c)) and it penetrates weakly into the quantum well structure, leading to poor coupling between the metamaterial and underneath gain media. An alternative to this approach is to replace the passive dielectric layer in fishnet metamaterial with active gain media. This can be accomplished by using

dye molecules/quantum dots in a polymer matrix as the dielectric layer. To investigate this approach numerically, we model the gain material as a Lorentz media with negative damping. The following parameters are used: gain wavelength 1550nm, gain linewidth of 100nm, base permittivity of 1.9 and Lorentz permittivity = -0.01, which corresponds to gain coefficient g = 1139cm^{-1} at 1550nm). Dimensions of fishnet metamaterial with this dielectric layer are tuned such that the resonance coincides with gain wavelength. The results of incorporating gain material are presented in Figure 2.11. While the enhancement (~3.6dB) in resonance is clearly observed, achieving the required amount of gain requires strong pump fluence. This is because of the fact that the active layer is buried underneath a metal film with thickness larger than the skin depth at pump wavelength. At pump wavelength of λ = 480nm (suitable for optical gain with infrared quantum dots), the absorption coefficient of Ag is 3.6x10^5 cm^{-1}. A 30nm thick Ag film reduces the incident pump intensity to $I = I_0 e^{-2\alpha z} = 0.12 I_0$. Hence, the metal film greatly reduces the pump intensity to just 12% before it can interact with the gain media.

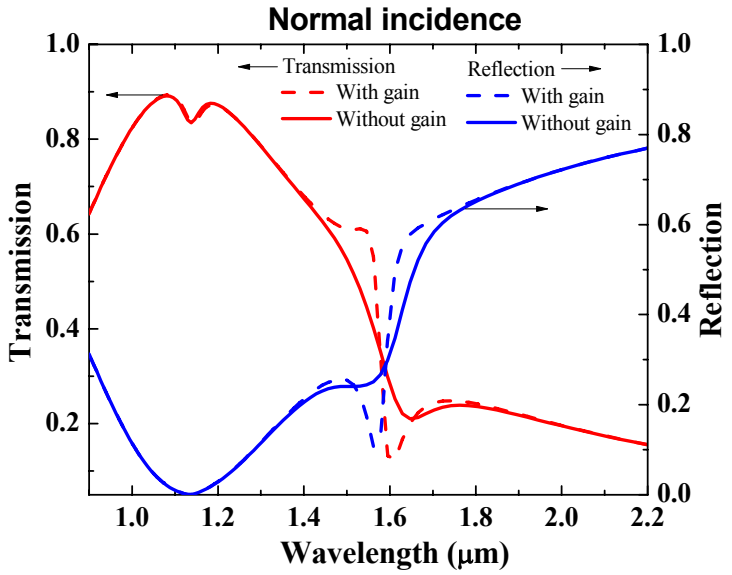

Figure 2.11 Effect of incorporating gain material in between the metal strips of fishnet structure. Fishnet resonance is enhanced when the gain is tuned to its resonance frequency. Dimensions of fishnet are t_m = 42nm, t_d = 20nm, dx = 100nm, dy = 316nm, a = b= 600nm.

A yet another approach to reduce losses in fishnet metamaterial is to cascade multiple fishnet layers in the direction of wave propagation, as was proposed recently.[38] While it may seem counterintuitive, but increasing the number of lossy metal layers indeed leads to reduction in overall loss and increased figure of merit of the metamaterial. This is due to destructive interference of antisymmetric conduction currents in the metal films which effectively cancels out current flow in intermediate layers and reduces the ohmic losses (Figure 2.12(a)). This was demonstrated experimentally where a three-dimensional configuration of the fishnet metamaterial with 21 layers showed one of the highest figure of merit to date.[31]

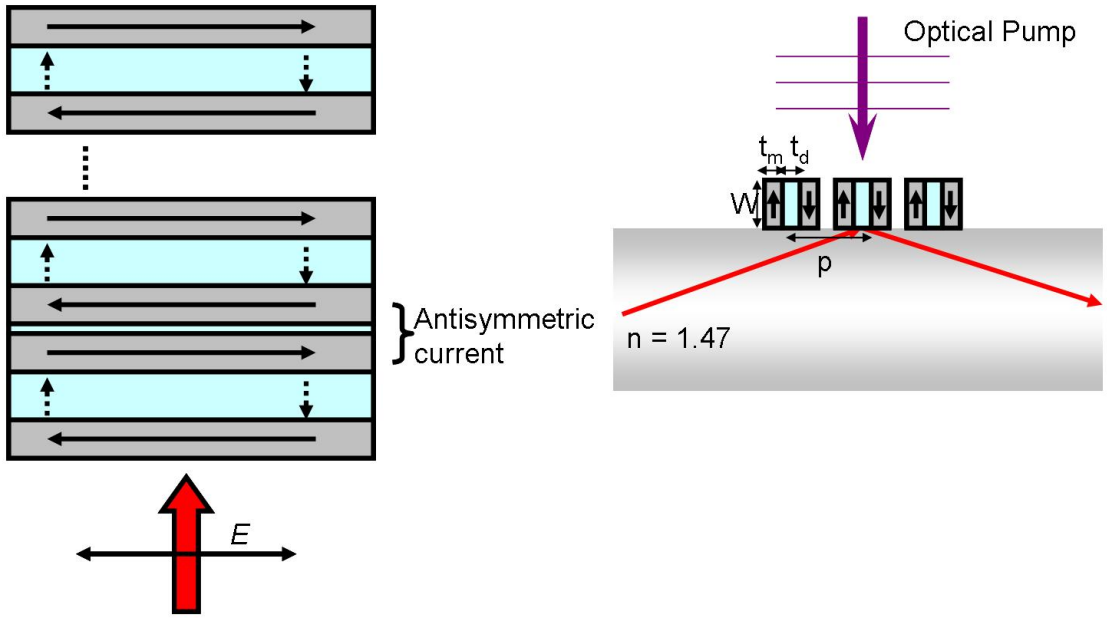

(a) **(b)**

Figure 2.12 (a) A bulk 3D configuration of fishnet metamaterial supports antisymmetric currents in adjacent metal strips leading to reduced losses. **(b)** Schematic illustration of a flipped fishnet modulator design in waveguide configuration. The oblique angle of incidence of guided modes supports antisymmetric currents. Moreover, the active layer (shown in light blue color) is directly exposed to pump signal, thereby allowing the modulation of guided modes more effectively.

To this end, we again note that the direction of incident wave in integrated fiber modulator is oblique. Hence, to reduce losses in the metamaterial at oblique incidences,

we have investigated a novel approach. In this approach, the individual magnetic resonator unit of fishnet is flipped (Figure 2.12(b)). As the wave propagates through the fiber, the individual flipped units experience different phase, which allows the metal films to have antisymmetric currents and hence low loss. This design also offers an enhanced modulation effect as the switching media is directly exposed to pump radiation, thereby improving the overall efficiency of integrated modulator.

2.4.2 Oblique angle simulations of flipped fishnet

To quantitatively understand the behavior of flipped fishnet when integrated onto a fiber, we have performed numerical simulations at oblique incidences. While methods of simulating metamaterials at normal incidence using finite-difference time-domain (FDTD) are well established,[33] broadband off-normal incidence simulations pose a unique problem to FDTD approach. In broadband simulations, the source injects a field with a constant in-plane wavevector for all frequencies. This implies that the actual injection angle varies as a function of frequency. Multiple simulations are required to gather simulation data at various frequencies for a fixed angle of incidence.[39, 40] We have investigated the flipped metal-dielectric-metal resonator design at oblique angles of incidence. A parametric sweep for various angles of incidence is done within the wavelength range of interest. Bloch boundary conditions are used along the periodic direction of the metamaterial. For simplicity, we have considered a two-dimensional case where the electric rods such as in fishnet design are eliminated. The data obtained from these simulations is irregularly spaced and has been interpolated to a rectangular grid of angle of incidence and wavelength for ease of plotting.

Figure 2.13(a) shows the dispersion plot of transmission response of flipped resonators against frequency and angle of incidence. It is observed that the resonance becomes narrower with increased angle of incidence (Figure 2.13(b)). This is attributed to reduced losses as increasing oblique incidences start to support antiphase currents in adjacent units of flipped resonators. To further quantify this effect, we have estimated the losses through the flipped fishnet as a function of angle of incidence. This is achieved by calculating imaginary part of refractive index $\mathrm{Im}(n) = \frac{\lambda}{4\pi W}\ln(\frac{1-R}{T})$,[31] where W is the

width of flipped resonator unit, R and T denote single-bounce reflection and transmission respectively. It is indeed observed that the imaginary part of index reduces with increasing angle (Figure 2.13(c)). To illustrate the operation of flipped fishnet as an integrated fiber modulator, we have plotted the field intensity and phase at probe wavelength of 1550nm (Figure 2.14(a), (b)). Light is incident from the fiber side at an angle of 70^0. Vector plot of the electric field depicting the phase is shown in Figure 2.14(b). It is observed that the phase (along the solid black lines) in the two metal regions differs by ~164^0. This suggests that the conduction currents in the two metal strips are almost antiparallel.

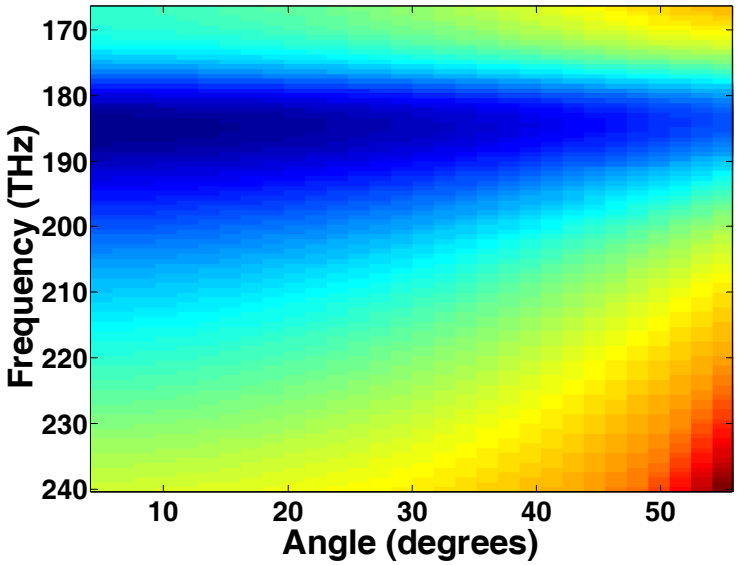

(a)

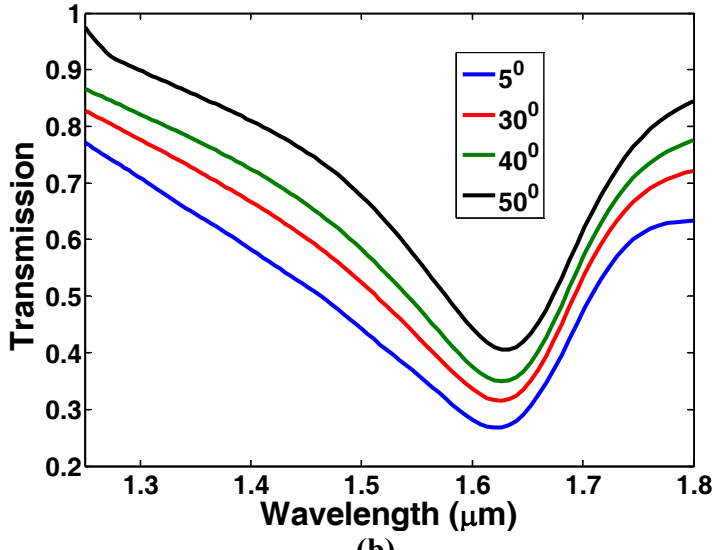

(b)

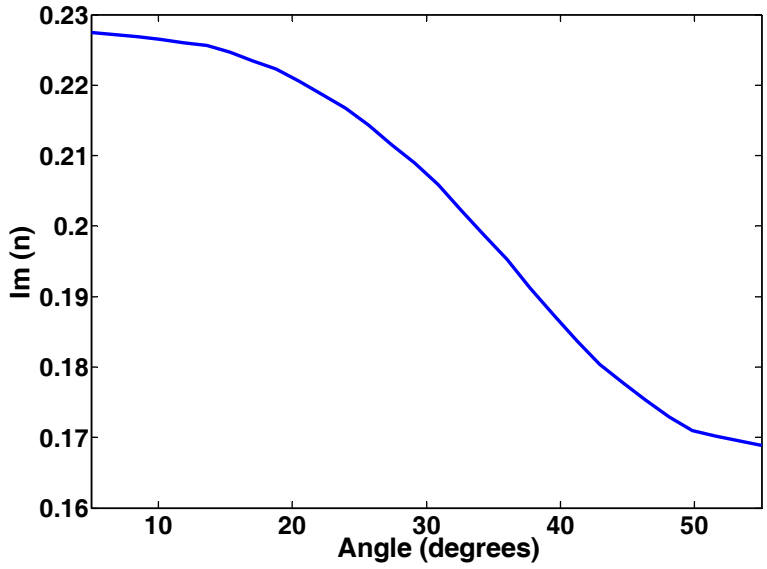

(c)

Figure 2.13 (a) Dispersion plot for flipped fishnet design computed with FDTD simulations. Dimensions used for the simulation are W = 260nm, p = 120nm, t_m = 30nm, t_d = 30nm (key in Figure 2.12(b)). The dielectric is assumed to be MgF_2 with ε = 1.9. **(b)** Transmission plot for flipped fishnet at a few selected angles of incidence. **(c)** Estimated imaginary part of refractive index as a function of angle of incidence for one bounce reflection of fiber-guided mode (λ = 1550nm) with flipped fishnet metamaterial.

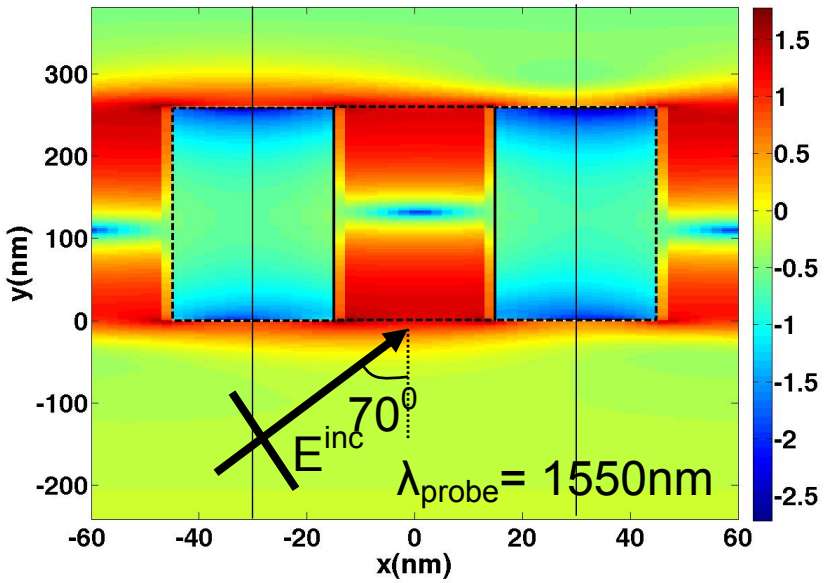

(a)

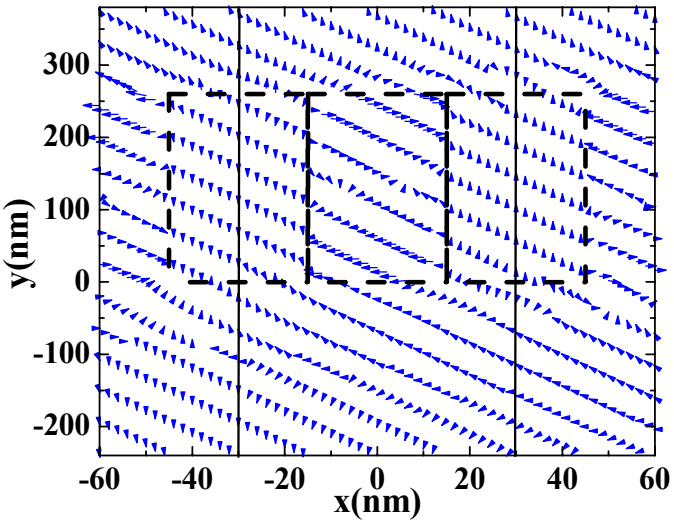

(b)

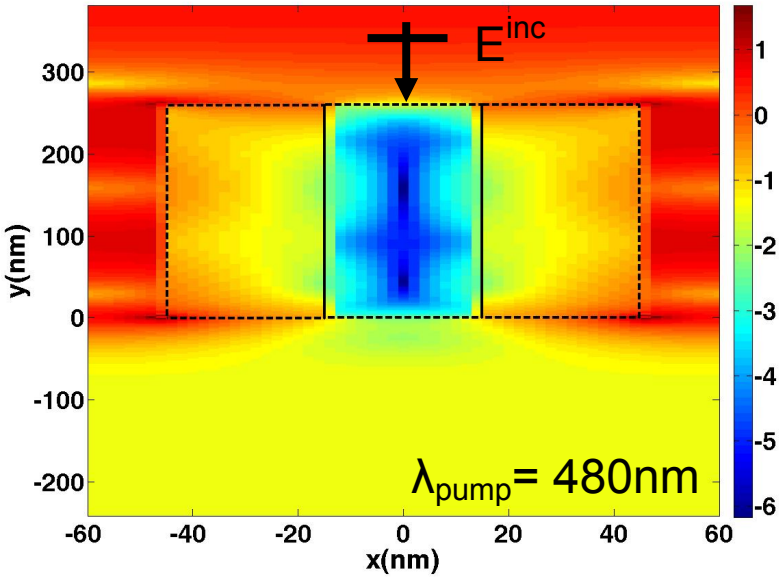

(c)

Figure 2.14 (a) Field distribution (log scale) at probe wavelength (λ = 1550nm). Light is incident from the bottom (fiber core, n = 1.47) at an angle of 70^0. The metal-dielectric-metal sandwich structure is marked by black dashed lines for clarity. **(b)** Vector plot of the electric field, showing counter-propagating current direction in the two metal layers. Phase difference in metal regions along the two vertical black lines is 164^0. **(c)** Field distribution (log scale) at pump wavelength (λ = 480nm), light is incident from the top.

To investigate the switching ratio of this integrated modulator in presence of a gain medium, we have plotted the field distribution at the pump wavelength (480nm) in Figure 2.14(c). Pump radiation is incident from the top which efficiently excites the gain layer sandwiched in between the two metal strips. The field distribution suggests that the pump field penetrates weakly into the fiber-core; however, the probe field interacts strongly with the gain layer (Figure 2.14(a)). Upon absorption of pump radiation, the gain layer provides optical amplification to the probe field. We observe that with moderate gain coefficients ($g = 1139cm^{-1}$), the reflected intensity for guided mode ($\lambda = 1550nm$) is modulated by 2.05dB (37%) when pump radiation is turned on. This is significantly better compared to the case, where gain is incorporated into substrate.[37] With less than half the amount of gain required the modulation is improved by more than 35%. Moreover, the required amount of gain in flipped fishnet can be achieved with less than 12% of pump power compared to reported fishnet structure, where the metal film is exposed to pump radiation.

2.5 Summary

To summarize, in this study we have investigated fishnet metamaterial as an optical modulator for on-fiber communication and information processing applications. This design offers small footprint (~10λ) and integration on fiber eliminates the need for bulk optical components. Numerical studies indicate an on/off ratio of 1.8dB for the integrated modulator. To reduce the losses associated with fishnet metamaterial and improve coupling to fiber guided modes, we have investigated a flipped fishnet design which has metal-dielectric-metal sandwich in a direction perpendicular to conventional fishnet. This design offers several advantages: Reduction in ohmic losses, as the antisymmetric currents in adjacent metal strips lead to destructive interference at oblique incidences; secondly, enhanced modulation effect, as the switching layer is directly exposed to pump radiation. With less than 12% of incident pump power compared to conventional fishnet, flipped fishnet shows a modulation depth of 2.05dB of fiber guided modes. This small footprint, high efficiency metamaterial opens exciting avenues for telecommunication applications.

3 IMAGING OF PLASMONIC MODES OF NANOSTRUCTURES USING HIGH-RESOLUTION CATHODOLUMINESCENE SPECTROSCOPY

3.1 Introduction

A multitude of optical phenomena at the nanoscale are made possible by resonant surface plasmons in artificially structured metal systems. These optical phenomena often give rise to properties that are difficult to obtain in natural materials. An entire new generation of artificial materials in the emerging field of plasmonics is designed to harness these properties through nanoscale engineering. These materials find tremendous applications in chemical and biological sensing.[41, 42] By simple surface patterning a thin metal film, it is possible to engineer its surface modes over a wide range of frequency.[23] Highly localized optical modes associated with patterned surfaces with nanoscale features (<~200nm) and the sensitivity of these modes to local refractive index finds tremendous potential in realizing compatible and efficient sensors. These optical modes known as localized surface plasmon resonance (LSPR) modes are responsible for producing strong scattering and extinction spectra in metal nanoparticles such as silver and gold. Exploiting local electromagnetic field enhancement associated with these plasmonic structures has led to several interesting applications such as enhanced fluorescence,[43] enhanced photo-carrier generation[44] and other nonlinear effects such as second harmonic[45] and high-harmonic generation[46]. Often the field is confined spatially on length scales on the order of 10-50nm and varies strongly with particle shape, size and material composition.[47] Unfortunately, diffraction-limited optical imaging techniques do not have enough spatial resolution to image these plasmon modes or precisely locate the "hot-spots" responsible for producing enormous enhancement such as in Raman imaging. Near-field scanning optical microscopy (NSOM) has been used to investigate these plasmon modes,[48] however, the resolution is limited by the tip size (~50-100nm). On the other hand, electron beam based characterization techniques such as cathodoluminescence (CL) and electron energy loss spectroscopy (EELS) are able to excite and image plasmon modes with very high spatial resolution. EELS for example has been demonstrated to resolve plasmon modes on length scale below 18nm.[49] EELS

technique, however, has to be performed in a transmission electron microscope (TEM), where it detects the inelastically scattered electrons and the loss suffered by electron beam in exciting surface plasmons. Although the technique has been described as one with the best spatial and energy resolution,[49] it requires samples to be electron transparent (typically <100nm). Specialized sample preparation procedure (used for TEM) and instrumentation makes it an expensive alternative and infeasible for samples on thick substrate. On the other hand, scanning electron microscopy (SEM) based CL technique does not suffer from this limitation. CL (in both SEM and TEM mode) has been utilized to image plasmon modes of particles and antennas of various shapes.[50-53]

CL has been used in materials science as an advanced technique for examination of intrinsic structures of semiconductors such as quantum wells[54, 55] or quantum dots[56, 57]. Typically, a tightly focused beam of electrons impinges on a sample and induces it to emit light from a localized area down to 10-20 nanometers in size. By scanning the electron beam in an X-Y pattern and measuring the wavelength and intensity of light emitted with the focused electron beam at each point, a high resolution map of the optical activity of the specimen can be obtained. In traditional cathodoluminescence of semiconductors, impingement of a high energy electron beam will result in the excitation of valence electrons into the conduction band, leaving behind a hole. The detected photon emission is actually a result of electron-hole recombination process. In the case of metallic nanostructures however, the photons are produced as a result of excited plasmons, i.e. collective motion of the conduction electrons induced by the fast moving electrons, and these induced charges can act back on the electron beam, causing it to lose energy as detected in EELS. In CL spectroscopy, we are able to detect radiation due to the oscillating plasmon on metallic structures, allowing quantitative study of the local field (Figure 3.1). Mechanism of this radiation has recently been presented[52, 58]. While, photon emission from semiconductor materials on interaction with electron beam is well understood, CL from plasmonic nanostructures is a relatively new field and deserves more attention.

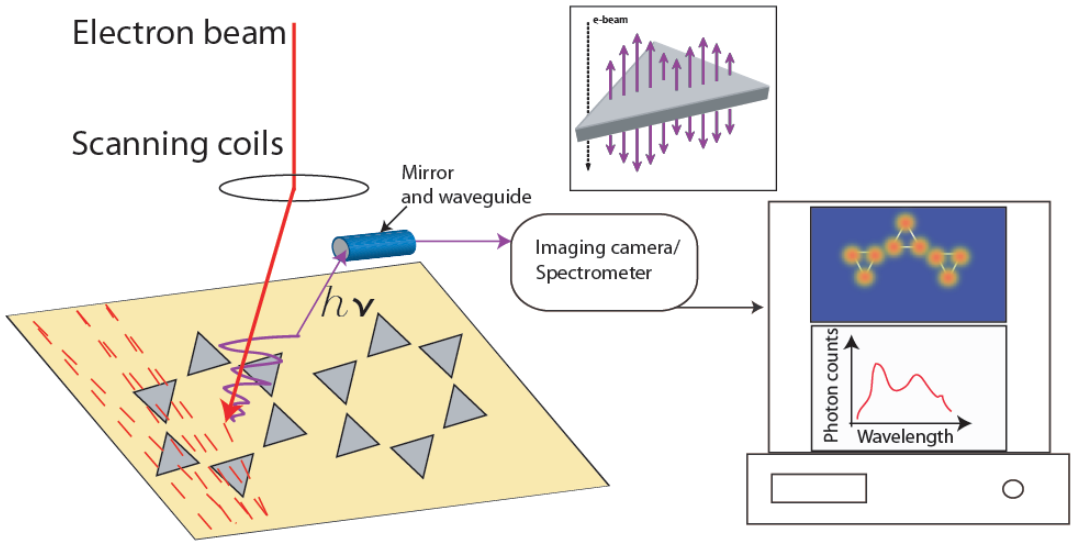

Figure 3.1 Schematic illustration of CL spectroscopy and imaging technique performed in scanning electron microscope. *Inset:* Passing electron beam induces current/electromagnetic oscillations in a metallic particle. These oscillations known as surface plasmon modes are responsible for radiation detected in CL.

In this study, we investigate the plasmon modes of silver (Ag) triangular nanoparticles using CL imaging and spectroscopy. The triangular particle geometry is of special interest to chemists and a hexagonal array of these particles has been extensively studied as a surface-enhanced Raman spectroscopy (SERS) substrate.[59, 60] It has been shown that Raman signal of molecules adsorbed on these particles can be enhanced by a factor of 10^8.[59] While it is understood that the excitation of plasmons in these metallic nanoparticles is responsible for the field enhancement effect, it is a challenge to identify the local fields associated with these plasmons. Several theoretical studies have identified the plasmon eigenmodes of triangular nanoparticles,[61-63] only a few experimental studies have demonstrated a resolution capability of mapping the spatial field variation associated with these plasmon modes.[49, 64, 65] In this work, we report direct excitation and emission of decoupled surface plasmon modes with CL spectroscopy (in SEM chamber) on triangular nanoparticles. In spectroscopic mode with monochromatic photon maps, we are able to distinguish the dramatic spatial variation of resonant plasmon mode on length scales smaller than 25nm. Numerical simulations were performed to identify the plasmon eigenmodes of triangular particles using a commercial finite-difference time-domain

(FDTD) simulator.[40] Both electron beam excitation and a more conventional plane wave scattering type calculations are performed to stress the differences between light excitation and electron excitation. Electron excitation calculations are performed by modeling the moving electron charge as a series of closely spaced dipoles with temporal phase delay governed by the velocity of electron. We also incorporate substrate effect into our calculations. We illustrate that while normally incident light can excite in-plane eigenmodes, electron beam is capable of exciting out of plane dipole mode of the particles.

3.2 Results and discussion

Conventionally, nanoparticles are characterized by their extinction spectra. The peaks observed in absorption or scattering spectra of particles under light excitation reveal resonant wavelengths of certain plasmon eigenmodes of the particle. While light excitation can couple to low frequency plasmon eigenmodes, it is hard to excite high-frequency plasmon states due to large momentum mismatch.[66] Electron excitation on the other hand can couple to high-frequency plasmon modes and recently it has been described to directly reveal the local density of plasmon states.[67] While optical techniques are limited in their resolution capability to image the plasmon eigenmodes, electron excitation on the other hand is potentially capable of resolving details below 10s of nanometers. Resolving surface plasmon modes and understanding the underlying physics is crucial to design better plasmonic devices tailored to specific applications.

For the purpose of this study we fabricated 40nm thick Ag equilateral triangular nanoparticles with ~200nm edge length arranged in a hexagonal lattice (as in SERS studies[60]). These particles are fabricated on silicon substrate and the shortest distance between two adjacent particles is >100nm. Silicon is chosen as the substrate material, to suppress background cathodoluminescence in the wavelength range of interest (near-UV and visible). For the purpose of numerical simulations we model and analyze single nanoparticle. This is because experimentally the interaction distance between electron beam and the particle is limited to few 10's of nms and hence, the excitation of plasmon modes is insensitive to particle coupling over ~100nm spacing. This is especially true for

particles on a non-plasmonic substrate such as silicon. We have performed spectrally resolved CL imaging experiments on these triangular nanoparticles on Si substrate. Emission spectrum of the particle induced by the electron beam passing through nearby the tip of the particle reveals a resonance peak at 405nm and a secondary peak at 376nm (Figure 3.2, blue solid line). This is in excellent agreement with simulations which indicate a resonance peak at 430nm and secondary peak at 385nm under tip excitation (Figure 3.2, red dashed line). It is to be noted that in this simulation, Si substrate has been approximated as non-dispersive loss-less material with an average refractive index of 4.8 (see methods).

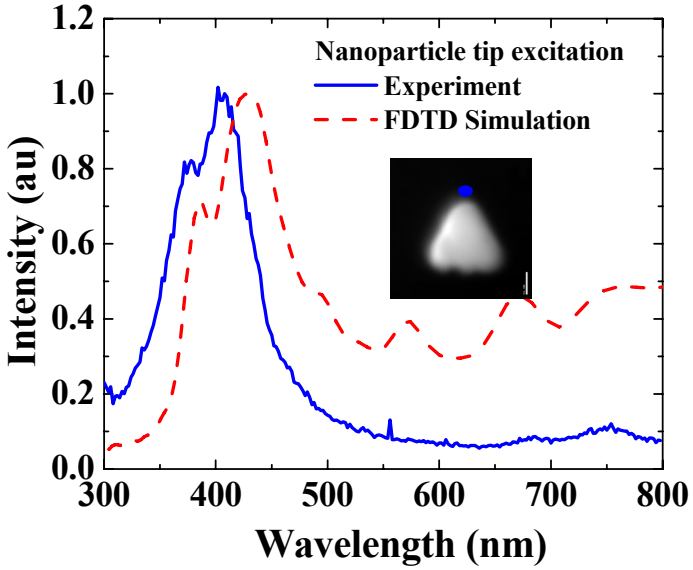

Figure 3.2 Luminescence spectrum collected from triangular nanoparticle under tip excitation (solid blue). The spectrum was corrected for grating response function. Corresponding simulated radiation spectrum (dashed red). *Inset*: SEM image of the particle with blue dot showing the position of the electron beam. The scale bar is 50nm.

Our experimental setup consists of a paraboloidal mirror, which is placed between the sample stage and the electron beam in a SEM chamber. The electron beam passes through an aperture in the mirror to the sample surface. The sample is at the focus of the mirror which lies 1mm below it. Light emitted by the sample is collected by the mirror and is directed to the detectors through a light guide. Spectrally resolved measurements

are performed using a monochromator (Czerny-Turner type). Light passing through a monochromator allows taking a spectrum, as well as images at a selected wavelength. In panchromatic mode of imaging, light skips the monochromator and all of the light is carried to the detection optics. The measurements are performed using a 15kV electron beam and a photo multiplier tube (PMT) detector with sensitivity encompassing near-ultraviolet (UV) and visible wavelengths (250-850nm).

Figure 3.3(a) is the secondary electron image (SEI) of triangular nanoparticle which gives the topographic information about the specimen. Figure 3.3(b) is a panchromatic CL image (PanCL). In panchromatic mode all of the emitted light is collected by the detector and hence the intensity at each pixel represents the integrated photon counts in the sensitivity range of the detector. PanCL image clearly depicts plasmon induced luminescence in Ag nanoparticle. This luminescence arises due to induced electromagnetic field on the nanoparticle caused by the external field of incoming electrons. The way this image is acquired is similar to SEM mapping i.e. by raster scanning the electron beam and collecting emitted photons rather than secondary electrons as done in scanning electron imaging. The collected light when passed through a grating monochromator allows resolving spectral features as shown in Figure 3.2. As an experimental reference, we have also recorded the emission from flat silver film which reveals a sharp bulk plasmon peak at 325nm and surface plasmon peak at 340nm (Figure 3.3(c), blue solid line). The location of these resonant peaks on flat silver matches with the material permittivity data[68] within ±5nm. The nature of these peaks (bulk vs surface) was further confirmed by a separate CL experiment, where we coated the flat silver film with ~5.5nm thick alumina (Al_2O_3) coating using Atomic Layer Deposition (ALD). In this case, we observe a sharp peak at 325nm and a relatively broad peak at 357nm (Figure 3.3(c), red dashed line). This confirms that the peak at 325nm corresponds to bulk plasmon of silver; whereas the second peak at 340nm (357nm) corresponds to surface plasmons at silver-air (silver-alumina) interface.

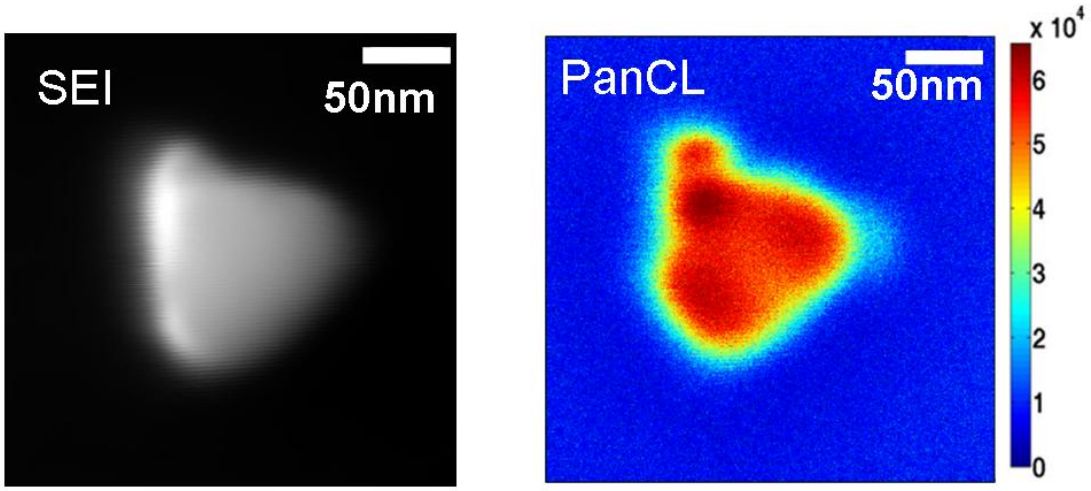

(a) **(b)**

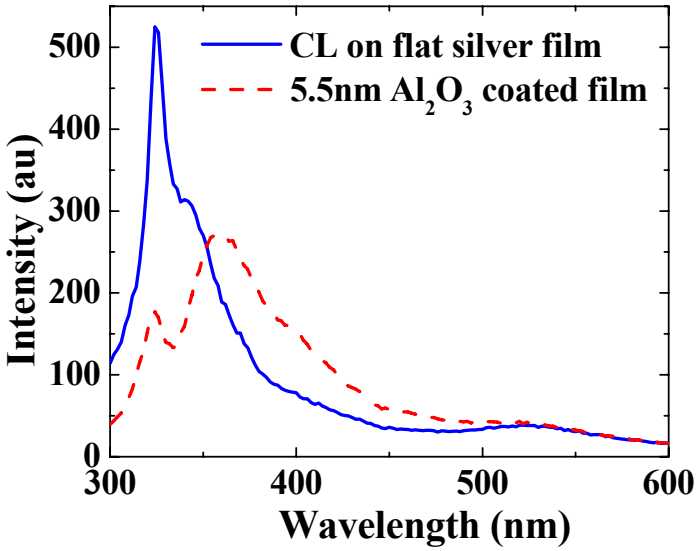

(c)

Figure 3.3 (a) Scanning electron micrograph of triangular nanoparticle. **(b)** Panchromatic CL image of the same. **(c)** Luminescence spectrum collected from a flat silver film.

Apart from emission spectra, monochromatic photon emission maps are acquired. These monochromatic CL images were obtained by setting the grating monochromator to a specific wavelength and scanning the electron beam over the nanoparticle. These

emission maps acquired by raster scanning the electron beam reveal the standing-wave patterns of surface plasmons.[49, 50] These standing-wave patterns are observed only under resonance conditions, i.e. when the field produced by the electron beam couples strongly to eigenmodes of the particle. Monochromatic CL image obtained at 400nm wavelength (with bandwidth 5.4nm and 5ms dwell time at each pixel) shows strong luminescent intensity when the electron beam scans over the tip region of the particle (Figure 3.4(a)). An image obtained at a wavelength of 355nm (Figure 3.4(b)) depicts no discernible features in spatial variation of emission suggesting non-resonant excitation.

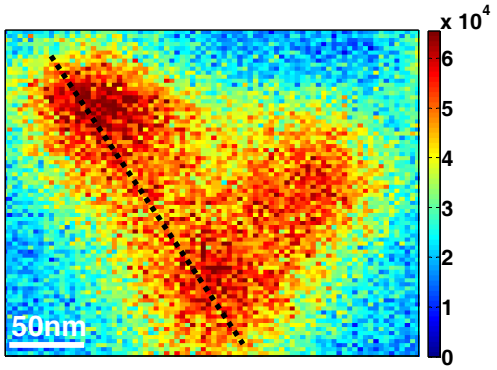

(a)

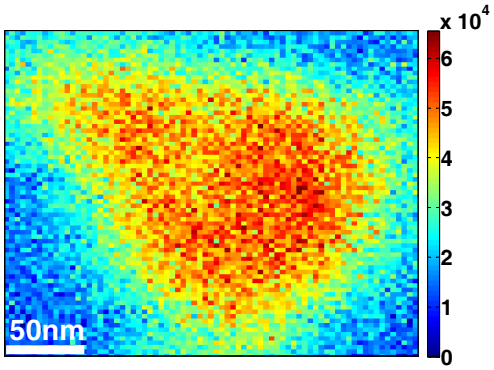

(b)

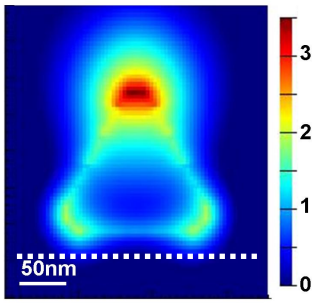

(c)

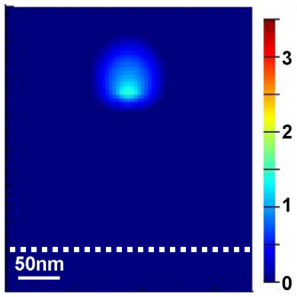

(d)

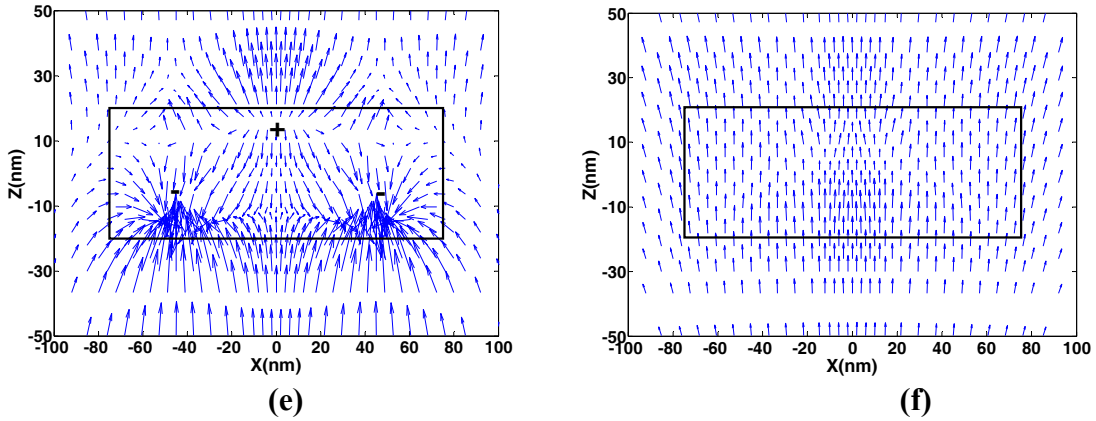

Figure 3.4 (a) Monochromatic photon emission map acquired at 400nm wavelength and **(b)** 355nm wavelength. **(c)** Simulated electric field intensity with tip excitation at 400nm wavelength for triangular nanoparticle on substrate (n = 4.8). **(d)** Intensity at 355nm wavelength. The color scale is in arbitrary units in log scale for (c) and (d). **(e)** Simulated vector plot of electric field at 400nm wavelength showing out of plane dipole mode excitation near the tip regions of the particle. The location of the plane is indicated by white dotted line in (c). Electron beam travels in *z* direction and the particle boundary is shown by black lines. **(f)** Vector plot at off-resonance wavelength of 355nm.

3.2.1 Numerical simulations

While CL experiments are limited to mapping the emitted light intensity by scanning the electron beam, numerical simulations allow us to map the field with fixed electron beam position. It is observed that under resonance conditions the induced electromagnetic field from the electron beam extends across the entire nanoparticle. This is illustrated in Figure 3.4(c) where the electron beam is located near the topmost tip of the particle and the intensity is plotted at 400nm wavelength. Notice the strong intensity near the tips of the particle, in contrast away from resonance (λ = 355nm), the induced field is weak and localized near the probe position (Figure 3.4(d)). Hence, the monochromatic emission maps acquired by scanning the electron beam under resonance condition illustrate strong luminescence near the tip regions of the particle and no spatial variation (above the noise level) away from resonance.

It should be noted that the emission pattern obtained at 400nm wavelength is very similar to the in-plane tip eigenmode of the triangular particle illustrated in earlier theoretical[61, 62] and experimental[49, 64, 65] studies. However, given the dimensions of the particle, the in-plane tip eigenmode occurs at much longer wavelengths. Our simulations indicate that the resonance at 400nm wavelength corresponds to out of plane dipole mode excitation by the electron beam. This is in strong contrast to light excitation, where a normally incident plane-wave excites electromagnetic field that correspond to in-plane charge oscillations. An electron beam on the other hand can excite out of plane charge oscillations. This is illustrated in Figure 3.4(e) which plots the simulated vector distribution of electric field in a plane parallel to the direction of electron beam. Under non-resonance condition (λ = 355nm), the induced field does not show charge oscillations (Figure 3.4(f)).

Light excitation:

To further illustrate the differences between light excitation and electron excitation, we have calculated the scattering properties of triangular nanoparticle under plane-wave illumination. When light is resonantly coupled to the plasmon modes of a nanoparticle, it leads to strong scattering and absorption of the incident field. Thus, the resonance modes can be identified based on extinction spectrum of the particle. Figure 3.5(a) presents the extinction spectra of isolated equilateral triangular nanoparticles (200nm edge length, 40nm thickness) suspended in air. We observe a dipolar plasmon peak at 677 nm and quadrupole peak at 400nm (solid black curve). The polarity of these peaks is identified based on vectorial description of the polarization response of the particle. These resonant peaks represent the well known in-plane "tip" (dipole) and "edge" (quadrupole) eigenmodes of the triangular particle (plane here refers to the plane of the particle).[49, 61, 69] It is to be noted that this result is for idealistic nanoparticle geometry with sharp tips. Deviation from this geometry such as rounding of tips is known to cause blue-shift of plasmon resonance peaks.[61] This happens because of effective reduction in volume of the particle that leads to reduction in its polarizability. Figure 3.5(a) and Figure 3.5(b) illustrate this effect. With a tip radius (*r*) of 20nm on all corners a blue-shift of 68nm is observed in dipolar resonance. It is observed that the shift in

quadrupole mode is not significant. Rounding of tips also reduces the maximum field enhancement factor which usually is localized to the corners of the tips. Hence, the peak extinction efficiency also reduces with increasing radius of curvature of tips. It is worth mentioning here that for a particle with 3-fold rotational symmetry, the extinction cross-section under plane wave excitation with two orthogonal polarizations (parallel and perpendicular to the edge of the triangle) are identical at normal incidence. However, the charge oscillations are oriented along the direction of incident polarization.

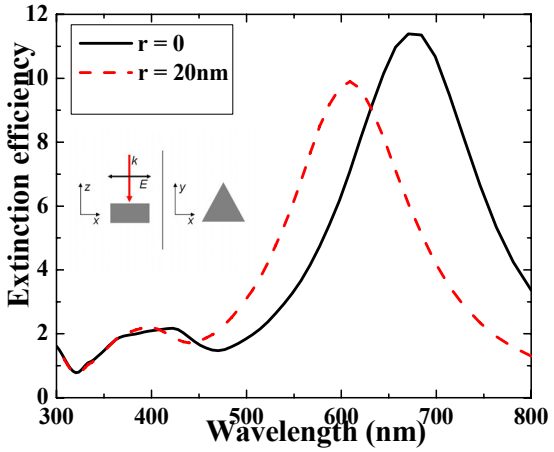

(a)

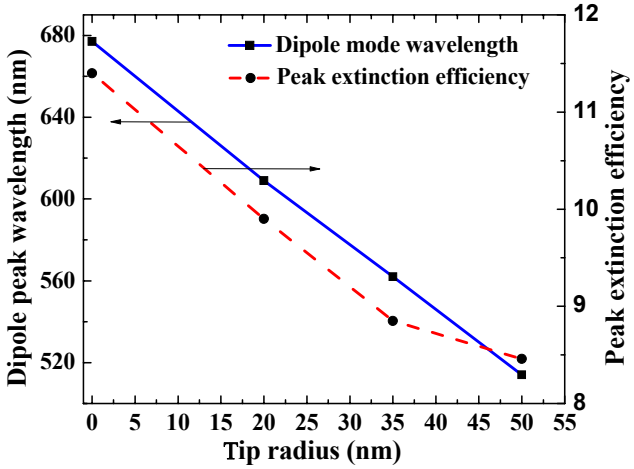

(b)

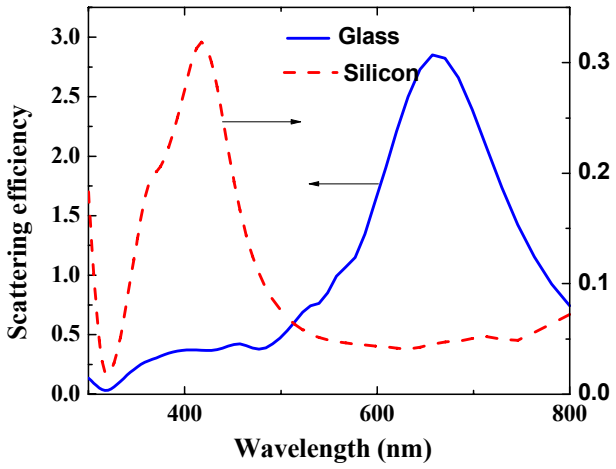

(c)

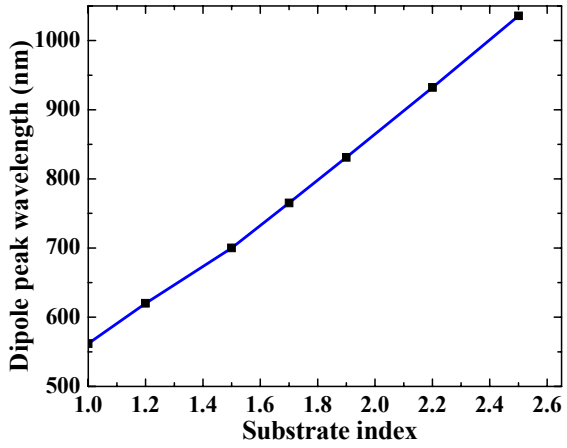

(d)

Figure 3.5 (a) Extinction spectra of triangular nanoparticle and effect of rounding of tips. *Inset*: Illumination and polarization direction of plane wave. **(b)** Shift of dipolar resonance and reduction in extinction efficiency with rounding of tips. **(c), (d)** Effect of substrate in plasmon resonances of the particle.

Next, we consider the effect of substrate. Scattered field characteristics of a particle vary significantly on interaction with a non-homogeneous dielectric environment such as in the presence of a substrate. Figure 3.5(c) illustrates this effect where the scattering cross-section of triangular particles situated on top of a substrate is plotted. In accordance with experimental setups suitable for light scattering measurements by

particles on a substrate, we incorporate light incidence from the top (air side) and only the scattered power in top half plane is considered in the calculations. It is observed that the dipolar resonance of the particle on a substrate is red-shifted with respect to its free-space resonance (Figure 3.5(d)). Qualitatively, the red-shift of the resonance can be explained by the increase in the effective permittivity of the surroundings. Particles appear larger with respect to the effective illumination wavelength in high-index surroundings which causes an increased retardation effect. Thus, for a non-dispersive substrate the amount of red-shift can be roughly approximated by taking the average refractive index of the surroundings. It is worth mentioning that the shift in higher order resonances such as quadrupole is not as significant as dipolar mode. Hence, for a high-index substrate such as silicon only in-plane quadrupolar resonance is observed (with light excitation) in visible range for the particle size under consideration.

Electron excitation:

As mentioned before scattering or extinction spectrum of a particle under plane wave excitation can be significantly different than its CL or EELS spectrum. While a plane wave represents a volumetric excitation source; on the other hand a highly focused electron beam represents a localized probe which gives information about local density of plasmon states.[67] Furthermore, the two electron characterization techniques also probe different properties of the particle; while EELS measures the total energy loss suffered by the electron in inducing electromagnetic fields on the particle, CL measures only part of the induced field which is radiated out. The two spectra EELS and CL would coincide if there were no losses in the system and the entire induced field is radiated. To numerically investigate the radiative modes that can be excited by a fast moving electron in CL setup, the electron beam can be modeled as a line current density source. The current density due to a moving electron can be written as: $\vec{J}(\vec{r},t) = -ev\hat{z}\delta(z - vt)\delta(x - x_0)\delta(y - y_0)$, where e represents electronic charge, v stands for velocity of electron, x_0 and y_0 represent the position of the electron beam and z is the direction of electron travel. In FDTD simulation approach, this current density due to a moving charge can be modeled as a series of dipoles with temporal phase delay that is governed by electron velocity (see methods). The radiative energy component of the induced electromagnetic field is

calculated by integrating the Poynting vector normal to an arbitrary large surface in the upper half-plane. Figure 3.6(a) presents the radiation spectra of triangular nanoparticle in free-space on excitation with a moving electron charge. Because of the inherent anisotropy of the particle, we model two distinguished cases 1) when the electron beam is close to the tip of the particle 2) when it is close to an edge of the particle. It is found that for both of these two cases main resonance occurring at ~600nm range (613nm for tip and 622nm for edge excitation) correspond to in-plane dipolar mode of the nanoparticle, as illustrated in Figure 3.6(b). However, the weaker resonance occurring at ~380nm corresponds to out of plane dipole mode. Since the thickness of the particle is much smaller than its edge length, out of plane dipole resonance occurs at much shorter wavelength compared to in-plane resonance. From the spectra it is evident that tip excitation is more efficient in exciting in-plane dipolar mode compared to edge excitation. Moreover, when the electron beam is close to the edge of the particle it also excites in-plane quadrupole mode at 400nm wavelength, which leads to broadening of the peak observed in the short wavelength range.

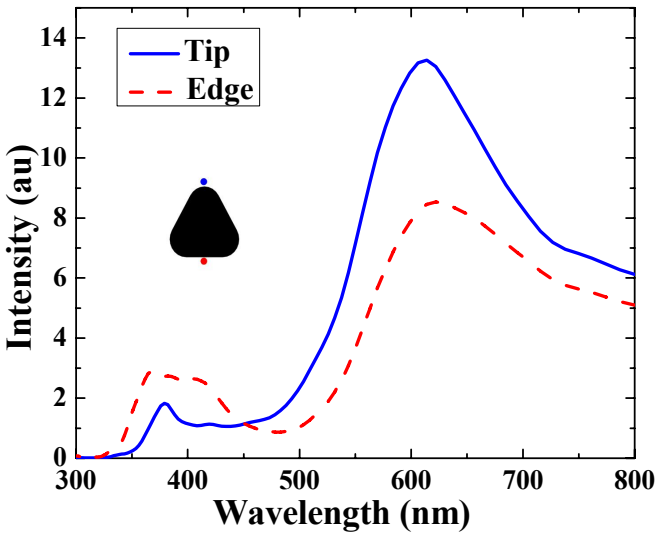

(a)

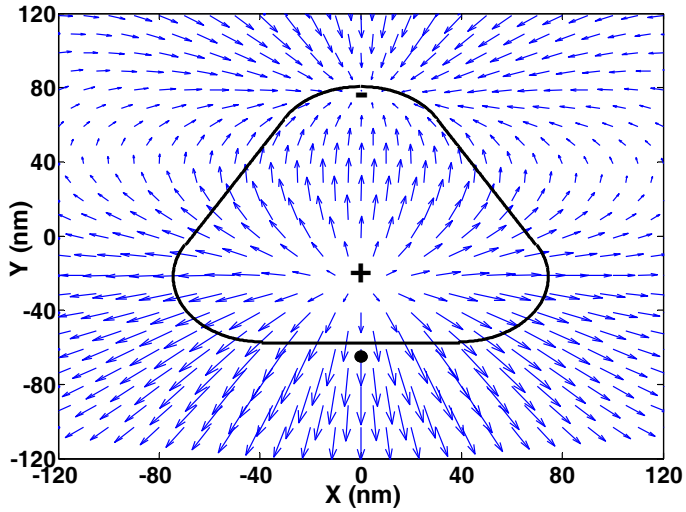

(b)

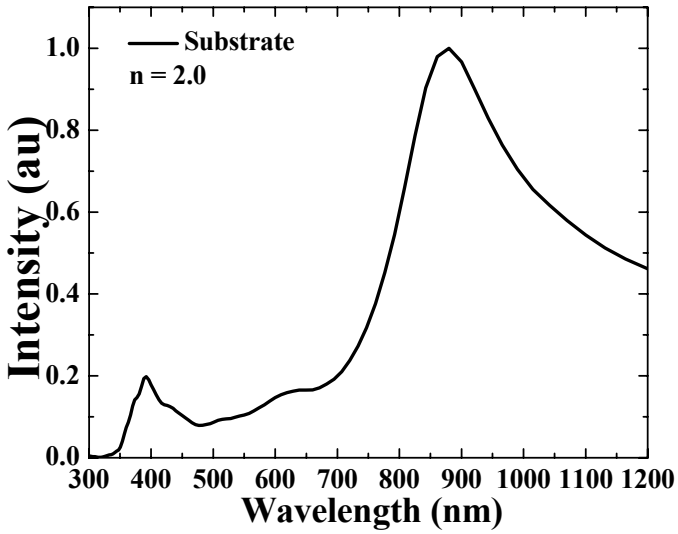

(c)

Figure 3.6 (a) Simulated radiation spectra of triangular nanoparticle in free-space upon excitation with electron beam. *Inset*: Position of the electron beam for tip (blue) and edge (red) excitation cases. **(b)** Vector plot of electric field for edge excitation case at 622nm wavelength, 10nm away from particle surface showing the excitation of in-plane dipole mode. The position of the electron beam is marked by black dot. **(c)** Effect of substrate on particle resonance upon excitation with electron beam (tip excitation). The substrate is assumed to be of constant refractive index n = 2.

We can extend some key observations from plane wave simulations to understand the effect of substrate on particle resonance under electron excitation. The in-plane dipole mode should red-shift because of increase in the index of surroundings. This is indeed observed from simulations (Figure 3.6(c)). The shift in out of plane dipolar mode is not as significant. This is expected since the thickness of the particle is small, the out of plane modes experience lower retardation effects. This suggests that for these triangular nanoparticles fabricated on high-index substrates such as silicon, electron beam can predominantly excite out of plane dipole mode and in-plane quadrupole mode in visible wavelength range. This is indeed observed in our CL experiments and simulations. The experimentally observed spectrum shows some minor differences compared to simulations (Figure 3.2). This may be attributed to the approximations we have made in our simulations. In electron excitation case, we did not include the dispersive properties of silicon substrate in our simulations. Secondly, in simulations the radiation spectra consists of photons integrated over the entire top half space. In our experiments, the collection angle of the mirror is limited to a cone angle of 160 degrees. Under the light of these differences, the experimental spectrum is in good agreement with simulations.

3.2.2 Resolution

It is evident that CL technique allows high-resolution mapping of plasmon modes. The quantification of the optical resolution of the technique deserves special attention. While, it may seem that the resolution of the technique would ultimately be limited only by electron-beam diameter, as in the case of secondary electron images, however, this may not be the case. This is because in secondary electron imaging, the incoming electron beam knocks off low energy secondary electrons (<50eV); the physical nature of this process allows high-resolution topographic image acquisition (1-5nm). However in CL imaging, photon emission can occur even when the electron beam is at a distance away from the particle. Electron beam can induce luminescence in a structure without physically passing through it, as indicated by our simulations. As a rough estimate, for 15keV electron beam, this interaction length can be as large as 18nm for light emitted at 400nm wavelength.[52] To estimate resolution, we fit Gaussians to the emission eigenmode

at 400nm wavelength. A clear spatial modulation (25% change in normalized intensity) of the eigenmode above the noise level is detectable on length scale as short as 25nm. This is illustrated in Figure 3.7, which plots the variation of radiation intensity along the edge of the particle as marked in Figure 3.4(a).

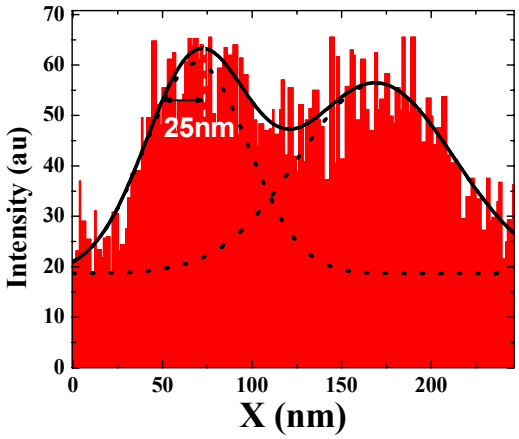

Figure 3.7 Variation of cathodoluminescence emission along the edge of the particle (marked in Figure 3.4(a)) at 400nm wavelength.

3.3 Summary

In this work CL imaging technique was utilized to image plasmon modes of Ag triangular nanoparticles with high-spatial (~25nm) and spectral resolution (~5.4nm). Spectroscopic analysis when combined with monochromatic imaging helps us to identify different channels of emission of plasmon modes. The process of radiative emission of plasmon modes in CL setup was modeled using FDTD approach. Simulations indicate that in contrast to light excitation, electron beam not only excites the in-plane eigenmodes of nanoparticles but is also able to excite out of plane modes. Because of the inherent anisotropy of the triangular particle, the position of the electron beam also influences the excitation of eigenmodes. This was presented in the context of "tip" and "edge" excitation of the particle. These results provide a better understanding of excitation and imaging of plasmon modes using CL spectroscopy.

Methods

Fabrication:

For the purpose of this study, Ag nanostructures were fabricated on silicon substrate. The samples were fabricated using a novel solid-state superionic stamping (S4) process.[2, 70] This process utilizes a pre-patterned stamp made of a superionic conductor such as silver sulfide which supports a mobile cation (silver). The stamp is brought into contact with a substrate coated with a thin silver film. On the application of an electrical bias with the substrate as anode and a metallic electrode at the back of the stamp as cathode, a solid state electrochemical reaction takes place only at the actual contact at the interface. This reaction progressively removes a metallic layer of the substrate at the contact area with the stamp. Assisted by a nominal pressure to maintain electrical contact, the stamp gradually progresses into the substrate, generating a pattern in the silver film complementary to the pre-patterned features on the stamp. Silver sulfide stamps were patterned using focused ion beam technique. A very thin (~2nm) chromium (Cr) layer is used as the adhesion layer for silver film on silicon. The fabricated structures are coated conformally with very thin dielectric layer (anatase TiO_2, 5 monolayer ~ 2.5Å) using atomic layer deposition (ALD) to protect the samples from environmental and electron beam damage. Excellent pattern transfer fidelity of the S4 approach down to sub-50nm resolution and ambient operating conditions make this process suitable for low-cost, high-throughput patterning of plasmonic nanostructures, such as presented in this study.

Simulation:

Light excitation: To numerically compute absorption and scattering by triangular nanoparticles, we utilize the total-field scattered-field (TFSF) formulation with FDTD approach. In this approach, the computation region is divided into two sections – one where the total field (incident + scattered) is computed and the second where only scattered field is computed. The particles are excited by a normal incident plane wave. Absorption and scattering cross-section are computed by monitoring the net power inflow in the total-field region near the particle and net power outflow in the scattered field region, respectively. Extinction cross-section is the sum of absorption and scattering

cross-section of the particle. Our numerical calculations suggest that for Ag nanoparticles scattering is approximately an order of magnitude larger than absorption. The material properties used in the calculation are obtained from generalized multi-coefficient model[40] that fits the dispersion data obtained from Palik[71]. This approach is more accurate for broadband simulations than fitting a single material model such as Drude or Lorentz.

Electron excitation: The electron beam has been modeled as a series of closely spaced dipoles each with temporal phase delay according to the velocity of the electron beam. In the absence of any structure, electron beam moving at a constant velocity does not generate any radiation. In FDTD, however, we simulate only a finite portion of the electron path and the sudden appearance and disappearance of the electron will generate radiation. To solve this problem, we run a second, reference simulation where all the structures are removed, and we can calculate the electromagnetic fields at any wavelength by taking the difference in fields between the simulations.[40] To get an accurate difference, we force the simulation mesh to be exactly the same with and without the structure. Currently, the methodology doesn't permit electron beam to pass through a lossy or dispersive substrate material.

4 SUBDIFFRACTION SUPERLENS IMAGING WITH PLASMONIC METAMATERIALS

4.1 Introduction

Conventional optical imaging is capable of focusing only the far-field or propagating component of light. The near-field or evanescent component with subwavelength information is lost in a medium with a positive refractive index, giving rise to diffraction-limited images. Near-field scanning optical microscopy and cathodoluminescence techniques are able to image surface and optical properties with far better resolution. However, being scanning techniques, the images have to be acquired in a point-by-point fashion.

In contrast, a thin planar lens made up of a negative-index metamaterial is capable of parallel subdiffraction imaging, as predicted by Pendry's theory.[24] As highlighted in Chapter 1, it is not easy to ensure a negative magnetic permeability at optical frequencies. Fortunately, however, in the electrostatic near-field limit, the electric and magnetic responses of materials are decoupled. Thus, for transverse magnetic (TM) polarization, having only negative permittivity suffices to obtain the near-field "superlensing" effect.[24] This makes metals with relatively lower losses such as silver (Ag), natural candidates for superlensing at optical frequencies. Exciting quasistatic surface plasmons of a thin silver film allows the recovery of evanescent waves,[19] thus providing subdiffraction images in the near field. Resolution as high as 60 nm or one-sixth of the wavelength has been achieved experimentally.[9] The device termed as silver superlens demonstrated parallel subwavelength imaging capability for arbitrary nano-objects. In this research, we investigate the ultimate resolution capability of silver superlenses. Our experiments demonstrate that with careful control of Ag surface morphology the resolution capability can be further extended to 1/12 of the illumination wavelength, providing unprecedented image details up to 30nm with 380nm illumination.

While the planar silver superlens can resolve deep subwavelength features, the imaging is limited to near-field. This is because planar superlens doesn't alter the evanescent decaying nature of subwavelength information. In this study, we have

investigated a far-field superlens operating at near-infrared (IR) wavelengths that allows resolving subwavelength features in the far-field. By utilizing evanescent enhancement provided by plasmonic materials such as silver nanorods and Moiré effect, we numerically demonstrate that subwavelength information of an object can be converted to far-field or propagating information which in turn, can be captured by conventional optical components. A simple image restoration algorithm can then be used to reconstruct the object with subwavelength resolution.

This unique class of optical superlenses with potential molecular scale resolution capability will enable parallel imaging (illustration Figure 4.1) and nanofabrication in a single snapshot, a feat that is not yet available with other nanoscale imaging and fabrication techniques such as atomic force microscopy and electron beam lithography.

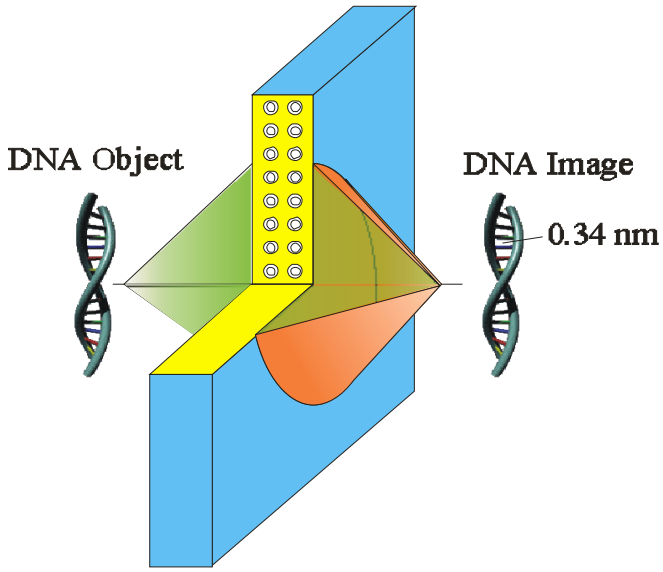

Figure 4.1 Realization of high-resolution superlens would open up the possibility of novel applications, such as imaging of biomolecules in their natural environment.[72]

4.2 Smooth superlens

Theoretically, silver superlens is capable of λ/20- λ/30 image resolution (where λ is incident wavelength).[25, 26] However, challenges remain to realize such a high resolution imaging system, such as minimizing the information loss due to evanescent decay, absorption or scattering. Our calculations (not presented here) have indicated that the

thickness of spacer layer (separating the object and the lens) and that of silver film are the two major governing factors that determine subwavelength information loss due to evanescent decay and material absorption. Particularly, the surface morphology of silver film plays a significant role in determining the image resolution capability. Below a critical thickness silver is known to form rough islandized films.[27] Rougher films perturb the surface plasmon modes causing loss of subwavelength details and hence diminished resolution.[73] Producing thin, uniform, and ultra-smooth silver films has been a holy-grail for plasmonics, molecular electronics and nanophotonics.

Recent research efforts directed toward smoothing thin silver films have resulted in novel approaches capable of producing ultrathin silver films with atomic-scale roughness. Logeeswaran et al. demonstrated that simple mechanical pressure can generate smooth films by flattening bumps, asperities, and rough grains of a freshly vacuum-deposited metal film.[74] The authors demonstrated that mechanical pressing of 100nm films at ~600MPa can reduce the root-mean square (RMS) roughness from 13nm to 0.1nm. However, the technique suffers from issues common to contact processes such as creation of surface defects, scratches, and delamination of silver films.

In this work, we explore a new approach to grow ultra-smooth silver films characterized by much smaller RMS surface roughness. An intermediate ultra-thin germanium (Ge) layer (~1nm) is introduced before depositing Ag. Utilizing Ag-Ge surface interactions, smooth superlens down to 15nm Ag thickness has been fabricated. It is observed that introducing the Ge layer drastically improves Ag surface morphology and helps minimize the island cluster formation. Roughness measurements of thin silver films (15nm) deposited with and without Ge layer (1nm) were performed using atomic force microscopy (AFM) and X-ray reflectivity (XRR) techniques. AFM measurements directly reveal the surface topography and it is observed that the RMS roughness of Ag (over 1x1μm scan area) deposited on quartz substrate improves from 2.7nm down to 0.8nm by introducing Ge (Figure 4.2(a), (b)). In XRR measurements, the decay in overall reflected intensity and the oscillation amplitude is strongly affected by the roughness of films. These measurements also suggest drastic improvements in the quality of Ag films incorporating Ge (Figure 4.2(c)). Intensity reflected from sample 1 (without Ge - blue dotted curve) drops sharply and does not show oscillating fringes owing to large

roughness of the Ag film. In contrast, sample 2 (with Ge – black solid curve) shows large number of fringes and a slow decay in intensity suggesting highly uniform films. Experimental data fit (red dashed curve) reveals that the roughness of 15nm thick Ag film in sample 2 is <0.58nm, more than 4 times smoother compared to sample 1. This is attributed to the fact that surface diffusion of Ag on glass (SiO_2) is energetically favorable compared to diffusion on Ge.[75] Hence, Ge acts as a wetting layer for Ag and helps a layer by layer growth.

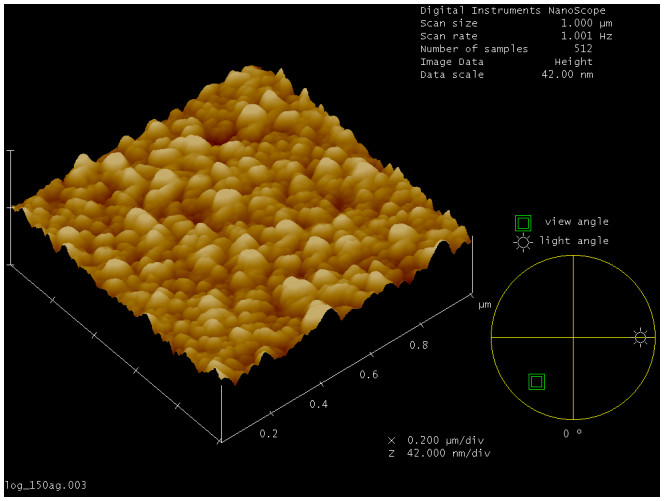

(a)

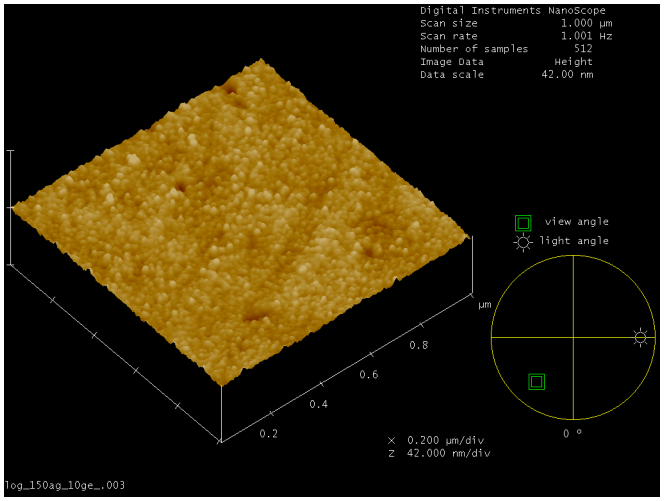

(b)

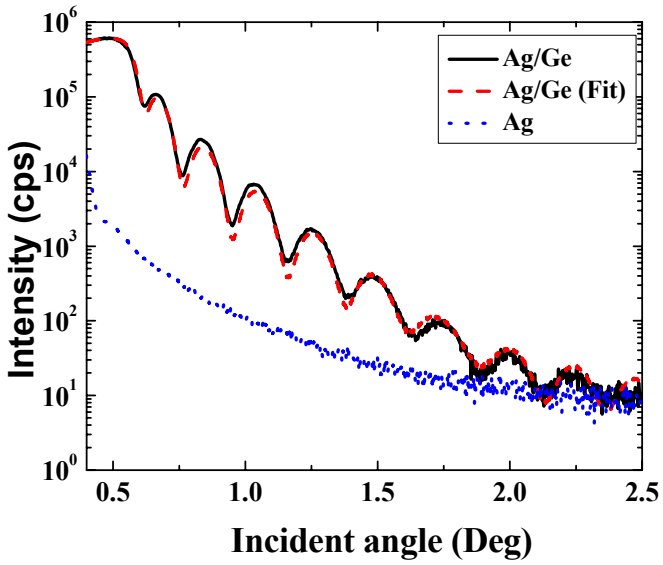

(c)

Figure 4.2 Smooth Ag growth on Ge **(a)** Surface topology from AFM micrographs (1x1μm scan) 15nm Ag deposited on quartz substrate and **(b)** 15nm Ag deposited with 1nm Ge on quartz substrate. **(c)** XRR studies of thin Ag films grown directly on quartz and with Ge intermediate layer.

The configuration of the smooth silver superlens is illustrated in Figure 4.3. An array of chrome (Cr) gratings 40nm thick with 30nm half-pitch, which serve as the object, was patterned using a nanoimprint process (see methods). In Figure 4.4, we present a step-by-step surface characterization of the prepared smooth silver superlens with embedded chrome gratings using AFM. In order to prepare a flat superlens on top of the objects (Figure 4.4(a)), it is necessary to deposit a planarization layer to reduce the surface modulations. Surface modulations can alter the dispersion characteristics of the plasmons and it smears out the image details. Also, the planarization layer should be thin to prevent a significant loss of evanescent components from the object. In our process, a planarization procedure using nanoimprint technique is developed to reduce the surface modulations below 1.3 nm (Figure 4.4(b)). This is achieved by flood-exposure of 66nm thick UV spacer layer over a flat quartz window under pressure, followed by subsequent reactive ion etching (RIE) to back etch the spacer to 6nm thickness on top of the chrome gratings. A 35nm thick Cr window layer is photolithographically patterned on top of the

spacer layer to enhance the contrast with dark-field imaging. Subsequently, 1nm Ge and 15nm Ag layer (superlens) is evaporated over the window layer (Figure 4.4(c)), followed by coating with a thick layer of optical adhesive (NOA-73) which serves as the photoresist. The substrate is exposed with a collimated 380nm UV light for 120 seconds (Nichia UV-LED, 80mW). The optical image recorded on the photoresist is developed and imaged with AFM (Figure 4.4(d)).

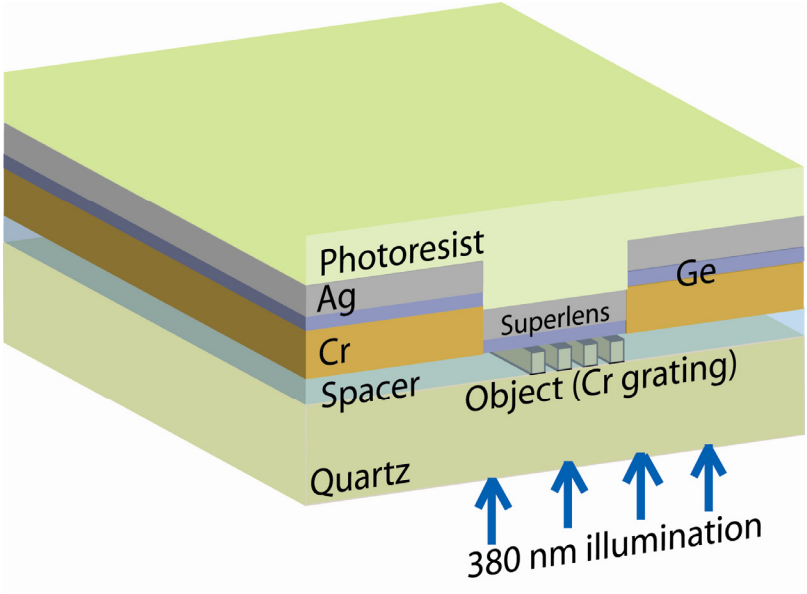

Figure 4.3 Schematic drawing of smooth silver superlens with embedded 30nm chrome gratings on a quartz window, operating at 380nm wavelength. To prepare the smooth superlens, a thin germanium layer is seeded.

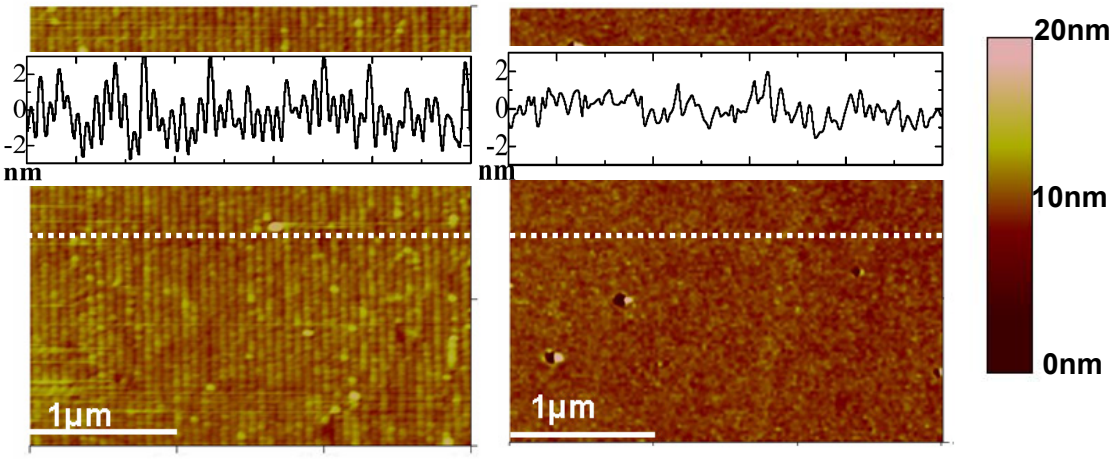

(a) **(b)**

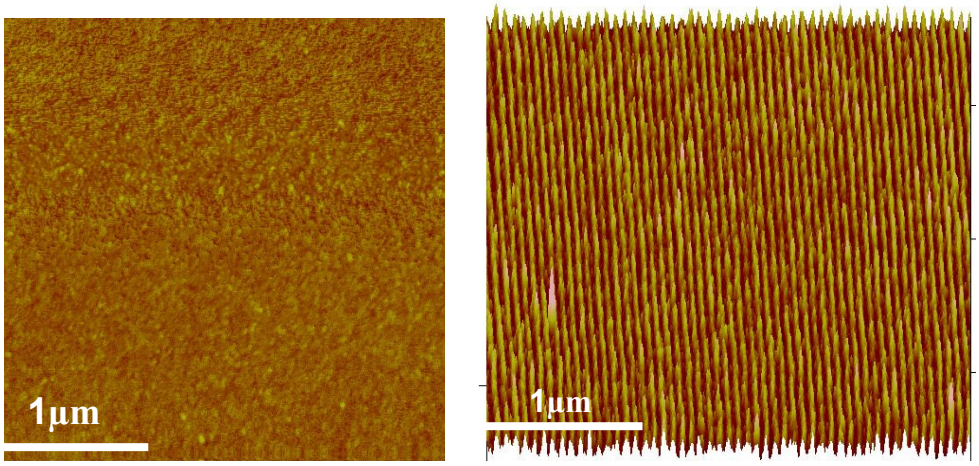

(c) **(d)**

Figure 4.4 Step by step surface characterization of the prepared smooth silver superlens sample with embedded gratings using atomic force microscopy. **(a)** Close-up image (3X3µm) of the nanoimprinted chrome gratings of 30nm half-pitch prepared on quartz windows. Inset presents the line section plot at the marked dotted line. **(b)** Surface profile of the sample after planarization with 6nm spacer layer onto chrome gratings, showing an RMS roughness of 1.3nm. **(c)** Surface profile of the sample after the deposition of Cr window, Ge and Ag layer. **(d)** The image of the 30nm half-pitch Cr grating area recorded on the photoresist layer after exposure and development. (Color scale for all images: 0 to 20nm).

For a qualitative comparison, we theoretically compute the resolving power of a thin ultra-smooth Ag-Ge superlens. Using transfer matrix approach,[76] we compute the optical transfer function and point spread function (PSF) of the multilayer lens system comprising of the spacer (6nm), Ge (1nm) and Ag layers for transverse magnetic polarization at incident wavelength of $\lambda = 380$nm.We optimize Ag thickness for maximum resolution. It is observed that 20nm thick Ag is capable of transferring a broad range of strongly evanescent modes and can exceed $\lambda/11$ half-pitch resolution. Adding Ge is generally unfavorable at UV wavelengths, as it is absorptive. However with only 1nm thick Ge in Ag-Ge superlens, the evanescent decay is only significant for feature sizes below $\lambda/12$. Computed PSF of such a superlens has full-width at half-maximum (FWHM) of 23nm. An object grating constructed with FWHM of 30nm at 60nm pitch

when convoluted with this PSF gives an image grating with FWHM = 37nm (Figure 4.5(a)). Moreover, the intensity contrast appearing in the image ($r = I_{max} / I_{min} \sim 3$) is sufficient to resolve this object with most commercial photoresists (PR) using superlens photolithography. In contrast, a near-field lens without Ag layer (e.g. spacer 27nm thick) gives a PSF with FWHM of 45nm. Constructed image of the object grating with this lens gives a FWHM of 113nm (~λ /3) (Figure 4.5(b)). The resulting image contrast ($r \sim 1.3$) is not sufficient to resolve the grating using photolithography.[77] We experimentally verify our findings by imaging Cr gratings with 30nm wires at 60nm pitch using Ag-Ge superlens and near-field control lithography experiments without Ag.

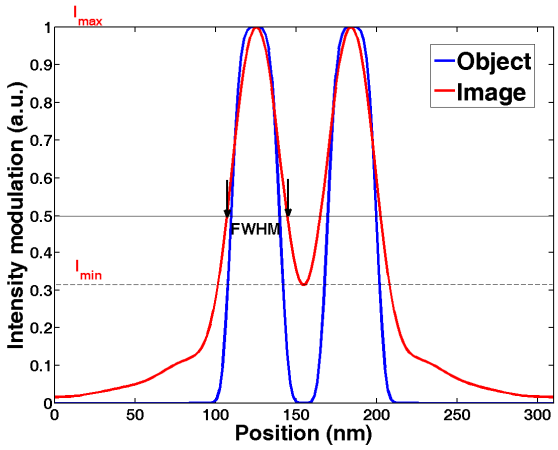

(a)

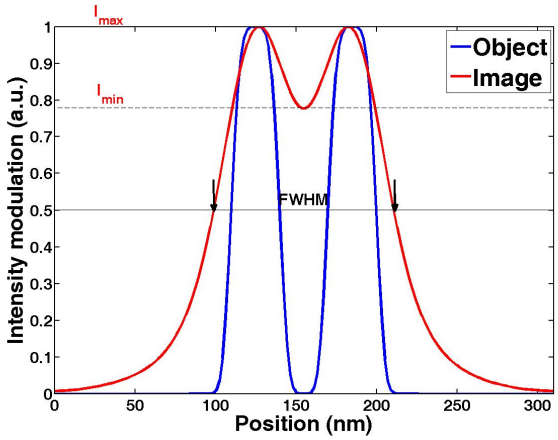

(b)

Figure 4.5 Computed image modulation **(a)** with superlens FWHM = 37nm **(b)** without superlens FWHM = 113nm.

Figure 4.6(a) (top panel) shows the image of the Cr grating area recorded on the photoresist layer after exposure and development. It is evident from section analysis of the recorded image (middle panel) that with careful control of surface morphology, the recorded image has ~6nm height modulations. The Fourier-transformed spectrum shows clear peaks upto third harmonic of the 60nm pitch Cr gratings successfully recorded on the resist layer (bottom panel). In a control experiment, when the Ag-Ge layers are replaced by equally thick spacer layer, we observe that only a portion of grating area is developed (Figure 4.6(b)). Moreover, the developed wires are much thicker (~47nm) and the poor contrast suggests loss of resolution as predicted by the PSF calculation. This confirms that near-field imaging alone without evanescent enhancement is not capable of resolving high-frequency spatial features (~λ/12) located just 27nm (= λ/14) below the surface.

4.3 Subdiffraction far-field imaging in infrared

In the previous section, we have demonstrated subdiffraction imaging with a smooth silver superlens at near-ultraviolet (UV) wavelength. Development of UV-superlenses is of importance to semiconductor industry in order to develop lithography techniques capable of patterning smaller and smaller transistors in keeping up with the Moore's law. A yet another wavelength range of interest where realization of subdiffraction imaging can have a profound impact is near to mid-IR. IR imaging technology such as Fourier transform – infrared (FT-IR) imaging and spectroscopy is one of the most common tools utilized in medicine and natural sciences for studies of materials and biological species. Measurements conducted in 1-20μm region of the electromagnetic spectrum bears special significance, as the absorption of radiation in this region represents signature vibrational, rotational or bending modes of molecules and functional groups. While FT-IR spectroscopic technique can resolve these narrowband features with high spectral resolution, diffraction-limited spatial resolution is often the bottleneck of this imaging tool. Subdiffraction imaging in the infrared can be achieved using a planar superlens, which enhances the evanescent components carrying the subwavelength information. Silicon carbide has been demonstrated as a suitable material

in mid-IR wavelength range supporting surface plasmon excitation,[78] a necessary precursor to achieve this evanescent field enhancement. However, this planar superlens is near-sighted, in that although the evanescent components get enhanced but their decaying nature outside the superlens is unaltered and hence, the detection optics needs to be very close to the superlens in order to capture the subwavelength information. This is usually achieved by scanning a near-field probe[78] or recording the subwavelength information onto a photographic material and using atomic force microscopy to read the information, as demonstrated in earlier section. However, the serial nature of these processes makes them unsuitable for real time and dynamic imaging applications.

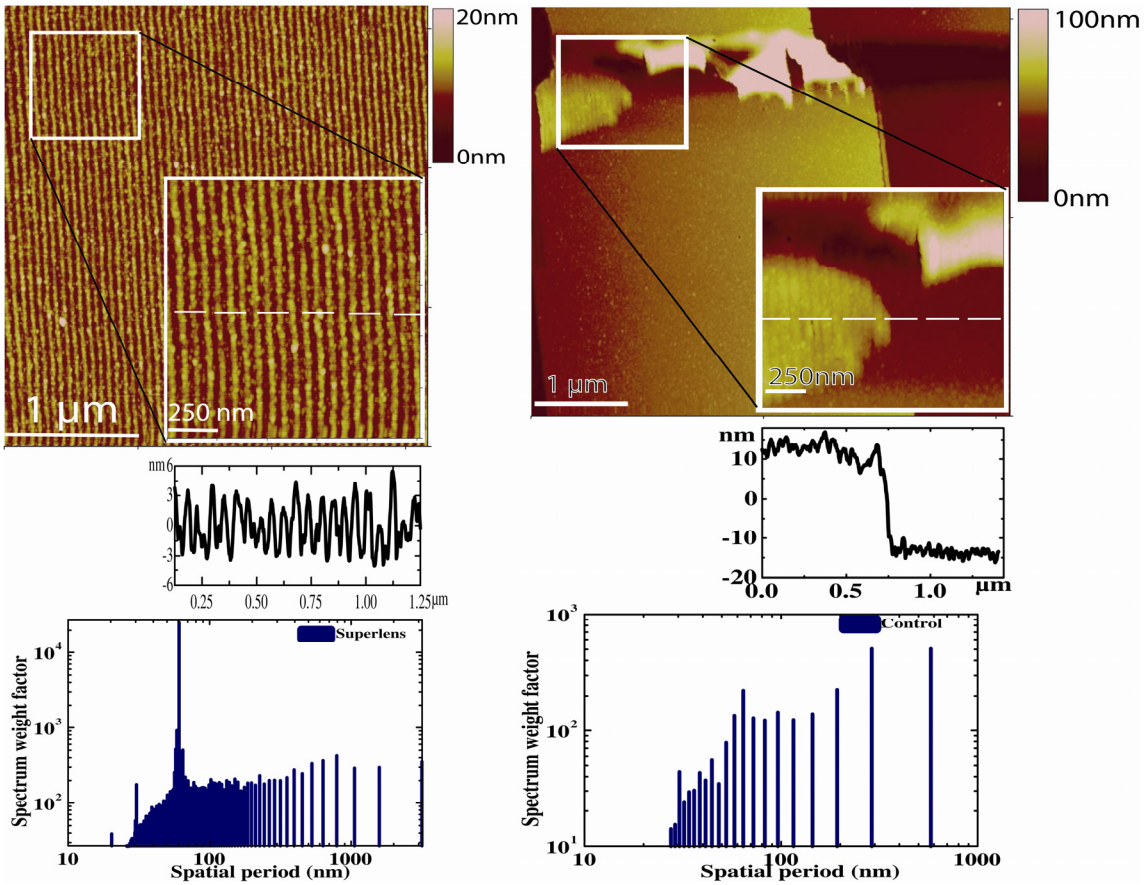

Figure 4.6 Subdiffraction optical imaging **(a)** with superlens **(b)** without superlens. Top panel: AFM of developed photoresist. Middle panel: Section analysis. Bottom panel: Fourier analysis.

Recently, several different approaches have been proposed to overcome this limitation and obtain subwavelength optical imaging in the far-field.[79-81] The basic idea is to convert the evanescent components with subwavelength information into propagating modes that can be processed by conventional optics. One of the approaches is to utilize the hyperbolic dispersion properties of a strongly anisotropic medium with opposite signs of permittivities ($\varepsilon_{\parallel}$ and $\varepsilon_{\perp}$).[80, 81] This device termed as hyperlens allows propagation of high-frequency components which ordinarily have an evanescent decay in an isotropic medium. To preserve the propagating nature of these high frequency components even outside the hyperlens, an annular cylindrical geometry is employed. This geometry carries an image magnification, so that the subwavelength features can be magnified to a size that can be seen by conventional diffraction-limited optics. This concept of anisotropic imaging has been experimentally demonstrated to achieve ~λ/3 resolution, utilizing an effective anisotropic medium with concentric rings of metal-dielectric lattice.[82, 83]

A yet another approach is to utilize Moiré effect mediated by excitation of surface plasmons allowing recovery of subwavelength information in the far-field.[84] By carefully designing a subwavelength grating, it is possible to achieve a "frequency mixing" of evanescent fields from the object and grating. In this work, we have designed a metamaterial substrate consisting of periodic array of silver nanorods. We show that these nanorods have plasmonic resonance in IR regime and the near-field enhancement associated with this plasmonic resonance fulfills the key requirement for frequency mixing of evanescent fields from the nanorods and the object. This near-field frequency mixing leads to formation of Moiré features that are of propagating nature and can be recorded with a conventional microscope. A simple image reconstruction algorithm can then be utilized to recover subwavelength spatial details of the object from the acquired far-field image (Figure 4.7). Our numerical simulations clearly show the formation of Moiré features in the far-field due to evanescent mixing between the nanorods and a periodic object grating. Object features corresponding to 2.5μm period are recorded in far-field with an incident wavelength of 6μm, indicating a far-field imaging resolution capability of λ/2.4. This imaging scheme can be easily interfaced with current FT-IR microscopes and would enable real time imaging with ultra high resolution.

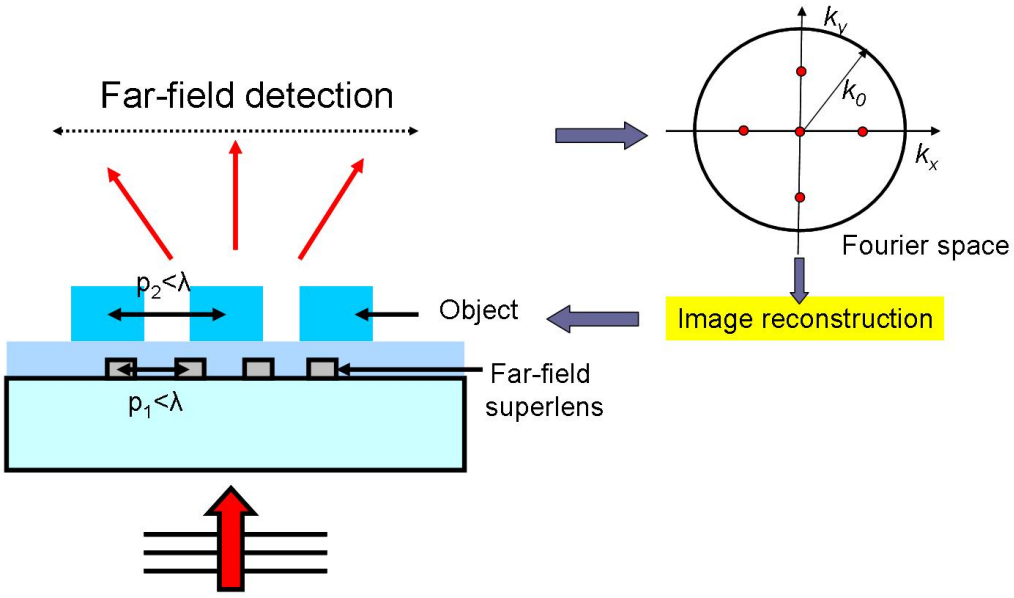

Figure 4.7 Subdiffraction far-field imaging scheme using Moiré effect.

4.3.1 Principle of far-field subwavelength imaging using Moiré effect

The Moiré effect is a well-known optical phenomenon that results in frequency-mixing when two periodic/quasiperiodic structures are superposed on each other. The effect is highly sensitive to relative orientation and displacement of the structures and has found unique applications in optical metrology.[85] Historically, like any optical imaging technique, the Moiré effect has also been limited to propagating fields.[86] This is because the evanescent fields from the two structures do not couple to form Moiré fringes. To have evanescent wave mixing, one needs to find a way to enhance the evanescent fields between the two structures. This can be achieved by excitation of surface plasmons which provide the essential enhancement of the evanescent fields. For example, if the near-field Ag superlens is inserted in between the two objects, the coupling of evanescent fields can be significantly improved. Thus, frequency mixing of evanescent fields can also lead to formation of Moiré fringes in the far-field.[87] The enhancement and frequency mixing of evanescent fields forms the basis of far-field subwavelength imaging using the Moiré effect. A device so designed has been termed as far-field superlens.[79]

The device consists of a periodically corrugated grating. Waves radiated by an object will be diffracted by the grating. The wavevectors of the diffracted waves are given by the grating law $k^{'} = mk^{i} + nk^{g}$, where $k^{'}$, k^{i}, and k^{g} are the diffracted, incident and grating wavenumbers in the transverse direction, and *m, n* represent the diffraction order. Since, we are interested in resolving subwavelength details of the object, we restrict our discussion to incident wavenumbers that lie in evanescent region. Out of the diffracted waves, only the ones with $|k^{'}| <= k_0$ are propagating in free-space, where k_0 is free-space wavenumber. This condition can be satisfied if the period of grating and incident field from the object are both subwavelength but with a small difference (e.g. $k^{'} = (k^{i} - k^{g}) < k_0$, where $k^{i}, k^{g} > k_0$). This results in formation of Moiré fringes in the far-field, provided that the evanescent field from the object couples to the grating. With a proper design of the far-field superlens it is possible to make sure that a unique correlation exists between the far-field Moiré pattern and the near-field subwavelength object.[87] In this case, a simple image restoration algorithm can then be used on the far-field Moiré pattern to reconstruct the object with subwavelength spatial details.

The far-field imaging approach can easily be understood from frequency domain point of view. Consider a two-dimensional object to be imaged which occupies a double-elliptical area in the spatial frequency domain (Figure 4.8(a)). Conventional lenses are limited to transmitting only the spatial frequencies that lie in the propagation region (Figure 4.8(b)). The image thus obtained does not carry the high-frequency information of the object (Figure 4.8(c)). Let's now imagine a lens specially designed to image only the high-frequency components from the object. The lens suppresses the propagating waves from the object, while enhancing the evanescent waves (Figure 4.8(d)). The lens also consists of a periodic grating which has a slight tilt with respect to the orientation of the object (Figure 4.8(e)). The evanescent field consisting of subwavelength information of the object couples to this grating. This object field upon diffraction through the grating would result in a pattern which is the convolution of the grating function and the object (Figure 4.8(f)). However, only the features that lie in the propagating region (marked by dotted circle) would be carried forward to the far-field. Notice that this far-field transmitted pattern, however, consists of all of the subwavelength information from the object, although in a shifted arrangement. With the knowledge of the grating periodicity

of the lens and its orientation, it is possible to reconstruct the image with subwavelength features of the object in the far-field. This forms the physical foundation of subwavelength far-field imaging.

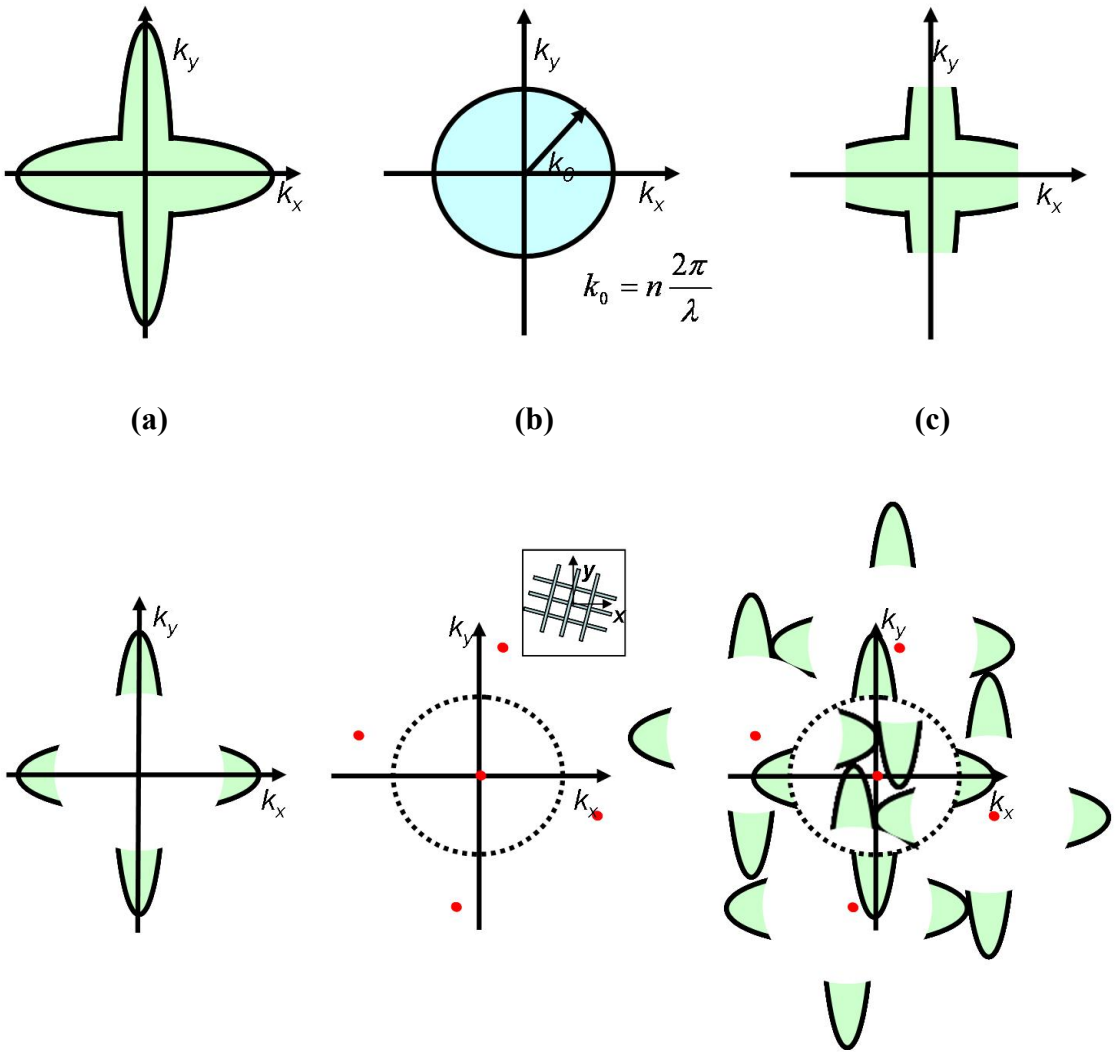

(a) **(b)** **(c)**

(d) **(e)** **(f)**

Figure 4.8 Frequency domain representation of **(a)** Object **(b)** Lens **(c)** Image formed with conventional lens. **(d)** Evanescent components comprising of subwavelength information of the object. **(e)** A rotated two dimensional periodic grating, dotted circle represents the propagation region. *Inset:* Real space image of grating. **(f)** Image obtained through the grating structure, note that the information lying outside the dotted circle is of

decaying nature, and only the information within the dotted circle is carried forward to the far-field.

4.3.2 Design of far-field superlens in infrared

As mentioned above, a key requirement to achieve Moiré effect for evanescent fields is to ensure field enhancement and coupling between the object and the lens. Surface plasmons provide the essential route to achieve this. However, direct excitation of surface plasmons on a planar interface between metal and dielectric in the infrared regime is limited by the choice of appropriate materials. To address this challenge, we note that the use of discrete plasmonic elements can achieve both goals; first to enhance near-field coupling with the object and second to transform the near-field components to far-field in the form of Moiré features. In this study, we have designed a metamaterial substrate consisting of discrete elements that provide surface plasmon excitation in IR. The metamaterial substrate consists of two-dimensional array of Ag nanorods. These nanorods support plasmonic resonance in IR range.[88] The fundamental dipolar resonance of the nanorods (with dimensions 1000 x 200 x 200 nm) on silicon substrate (mid-IR transparent) is observed at a wavelength of $\lambda = 6.1\mu m$. This matches reasonably well with the classical description from antenna theory, which predicts the dipolar resonance at $\lambda_{res} = 2nL = 5.04\mu m$, where n is the effective refractive index of the surroundings and L is the length of linear antenna. Substrate effect can be taken into account by taking an average permittivity of the surroundings. Deviation of the resonance wavelength from antenna theory is attributed to the finite penetration of the electromagnetic field into nanorods (non-zero skin depth) and periodic arrangement of the rods. Since, the cross-section dimension of the nanorod is much smaller than wavelength but larger than the skin depth of metal, the resonance and linewidth are found out to be almost independent of it. The nanorod resonance is strongly polarization dependent and is observed only when the electric field is aligned parallel to the rod axis. Figure 4.9(a) presents the normal incidence far-field transmission spectra of periodic array of nanorods (lattice 2x2μm). At resonance, nanorods exhibit strong extinction due to excitation of surface plasmons.

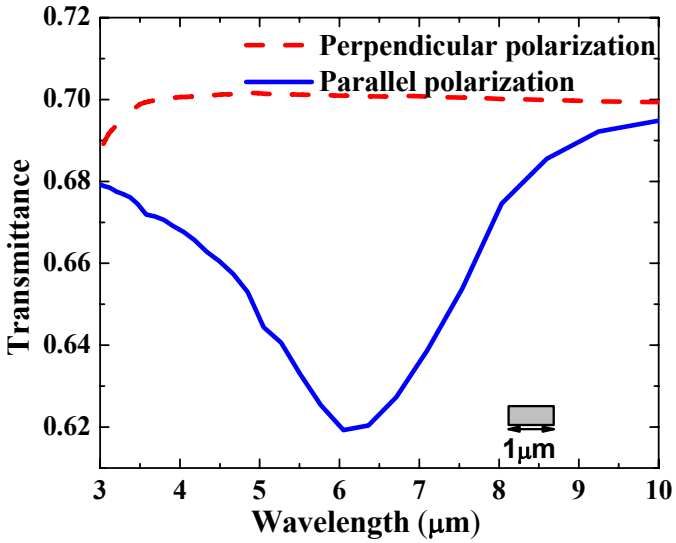

(a)

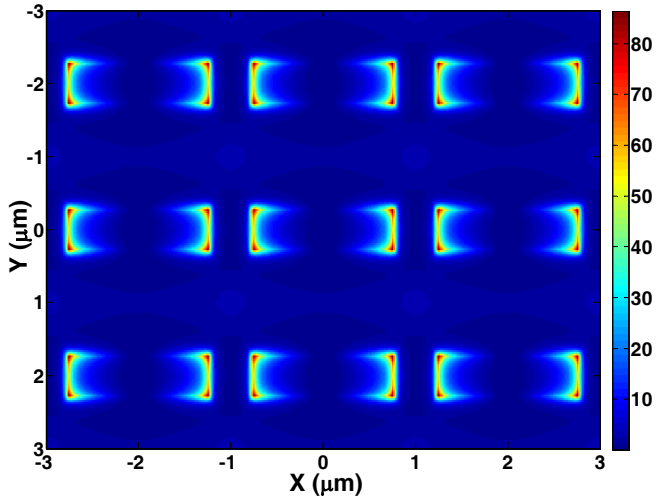

(b)

Figure 4.9 (a) Transmission spectra of periodic array of Ag nanorods in the IR region. Resonance is observed only for parallel polarization, i.e. when the electric field is aligned along the direction of rod axis. **(b)** Near-field intensity calculated 20nm above the surface of the rods at the fundamental dipolar resonance $\lambda = 6.1\mu m$.

Calculated near-field intensity (~20nm above the surface of the nanorods) show local-field enhancement at the fundamental dipolar resonance (Figure 4.9(b)). In a separate study by Neubrech et al.,[89] this near-field enhancement has been shown to

improve the sensitivity of infrared detection. Utilizing the resonant interaction between surface plasmons and vibrational modes of a molecule, a detection sensitivity of less than one attomole of molecules was demonstrated. In context of subdiffraction imaging, we show that this near-field enhancement in combination with the grating momentum provided by nanorod array, allows evanescent fields from the object to be diffracted to the far-field. This is evident from Figure 4.10, which shows the optical transfer function of nanorod array for evanescent waves calculated at $\lambda = 6\mu m$. The incident evanescent wave is simulated by a total internal reflection mechanism, as illustrated in Figure 4.10 inset. It is observed that the far-field transmission of such a nanorod array system is enhanced for wavevectors lying in the region $k^i = 2k_0$ to $4k_0$. Without the nanorod array, evanescent waves have far-field transmission intensity given by $\exp(-2\,\mathrm{Im}(k_z)z)$, where $k_z = i\sqrt{k^{i2} - k_0{}^2}$, which is $<10^{-9}$ for $k^i > 2k_0$. The enhanced transmission due to nanorods is attributed to surface plasmon excitation, which allows grating coupling of evanescent modes ($2k_0 \le k^i \le 4k_0$) to far-field propagating waves, in accordance with the grating law $k^{'} = k^i - k^g$, where for nanorods $k^g = 3k_0$. In the next section, we numerically demonstrate this coupling effect by computing the far-field spectrum of objects imaged with the nanorod array.

4.3.3 Computing far-field angular spectrum

To demonstrate far-field imaging numerically, we perform forward computations, i.e. from near-field profile to far-field angular spectrum. As a simplified example, we consider imaging of an aluminum object consisting of a 2-dimensional subwavelength grating. The periodic nature of the object makes the simulation and analysis simpler while capturing the essential physics of the imaging process. The periodicity of the object is chosen to be 2.5x2.5μm with linewidth of 1.25μm. The corresponding lattice constant of metamaterial substrate consisting of array of nanorods is 2x2μm. Near the resonance wavelength of the nanorods at $\lambda = 6\mu m$, the corresponding wavevectors are $k^i = 2.4k_0$ (object), and $k^g = 3k_0$ (nanorods). It can be seen that diffracted waves corresponding to the evanescent wave mixing of these wavevector components are

propagating only through first order diffraction $k^{'} = (k^{i} - k^{g}) = 0.6k_0$. Hence, there is no overlap between diffracted waves and a clear one to one relationship exists between far-field angular spectrum and near-field object profile.

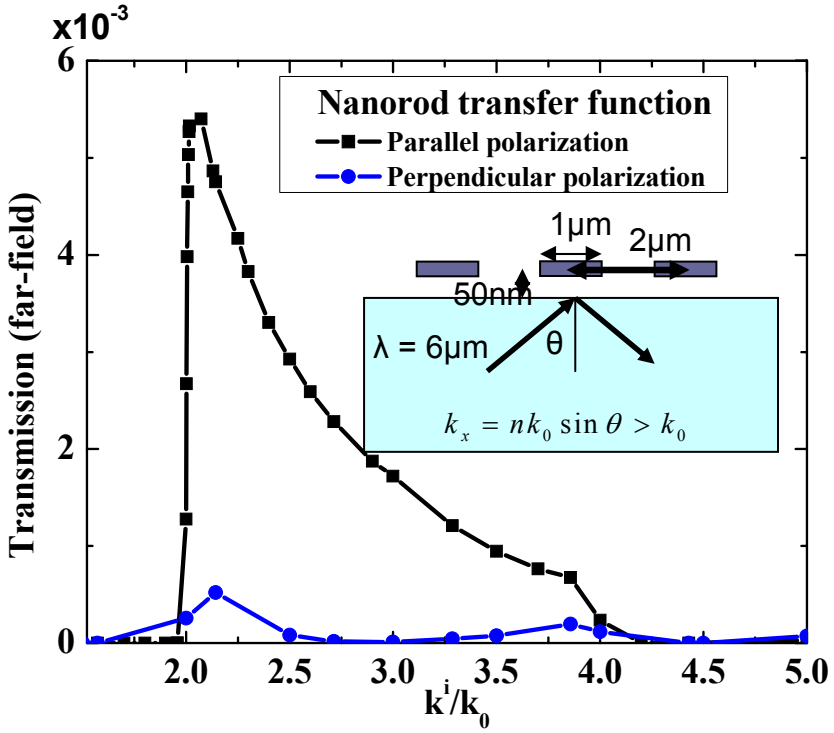

Figure 4.10 Far-field transmission computed for various incident transverse wavenumbers at λ = 6μm, for parallel and perpendicular polarization. *Inset:* Schematic of the simulation geometry. A total internal reflection mechanism is utilized to simulate evanescent wave incidence on the nanorod array.

To obtain the far-field angular spectrum, we utilize the fact that in the far-field only contribution to a point of observation is from a plane wave originating from the source and propagating along the radial direction to the point of observation. We have performed numerical simulations to compute the far-field angular spectrum of nanorods overlapped with a subwavelength object grating. Simulations are performed using a commercial finite-difference time-domain tool.[40] The nanorods on silicon substrate are physically separated from the subwavelength object grating by a thin (50nm) dielectric

spacer layer. A plane wave illumination is assumed from the substrate side and near-field profile is monitored 50nm away from the subwavelength object on the air side. Periodic boundary conditions are assumed in x-y directions with a period of 10μm, which is integral multiple of the period of the rods and the object. The near-field data (E_x, E_y, E_z) recorded in the simulations is decomposed into plane waves using a far-field projection algorithm which gives the far-field angular spectrum of the field on the surface of a sphere (radius = 1m). The projected far-field spectrum of the combined near-field (object + nanorods) is shown in Figure 4.11(a). The polar plot shows variation of electric field intensity $|E|^2$ as a function of θ andϕ, where θ, ϕ are the polar and azimuth angles of the spherical coordinate system. The far-field intensity $|E|^2(\theta, \phi)$ is directly related to the Fourier components of the field,[90] since in the far-field $k_x = k_0 \sin\theta\cos\phi$, $k_y = k_0 \sin\theta\sin\phi$. Apart from zero frequency (DC) components, we observe hot spots in the far-field angular spectrum at the locations marked by white dotted circles. Lowest frequency diffraction spots occur at $(\theta,\phi) = (36.9^0, \pm 90^0)$ & $(36.9^0, \pm 180)$, while higher order diffraction features are observed at $(\theta,\phi) = (58^0, \pm 45^0)$ & $(58^0, \pm 135^0)$. These locations correspond to wavevectors $(k_x, k_y) = (0, \pm 0.6k_0), (\pm 0.6k_0, 0)$ and $(0.6k_0, \pm 0.6k_0)$, $(-0.6k_0, \pm 0.6k_0)$, respectively. In other words, if a lens were to directly convert these Fourier components of the far-field into a real-space image, we would see a 2-dimensional grating with period of 10x10μm for 6μm illumination wavelength. Clearly, this period corresponds to the period of Moiré fringes which result from the evanescent wave mixing between the nanorods and the object grating. To further illustrate this imaging concept, we compute the far-field angular spectrum for a second object which consists of a 2-dimensional grating with period 3.5x3.5μm. The Moiré interference fringes in this case correspond to wavevectors $k' = (\frac{6}{2}m + n\frac{6}{3.5})k_0$, where 6μm is the incident wavelength and 2μm is the periodicity of nanorods. It is clear that the Moiré features are propagating with the lowest diffraction order corresponding to $m = \pm 1$ and $n = \mp 2$. The corresponding Moiré features have $k' = \mp 0.429k_0$ which gives $\theta = 25.4^0$. These features are indeed recovered in the far-field as illustrated in Figure 4.11(b), (d).

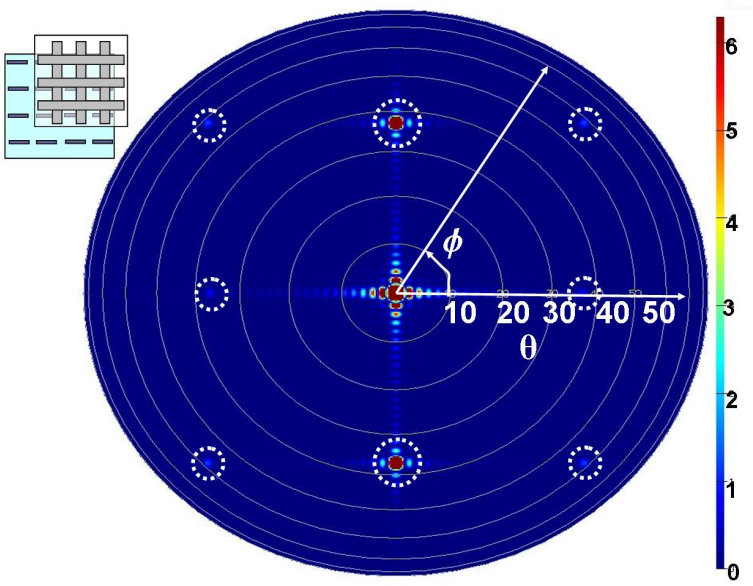

(a)

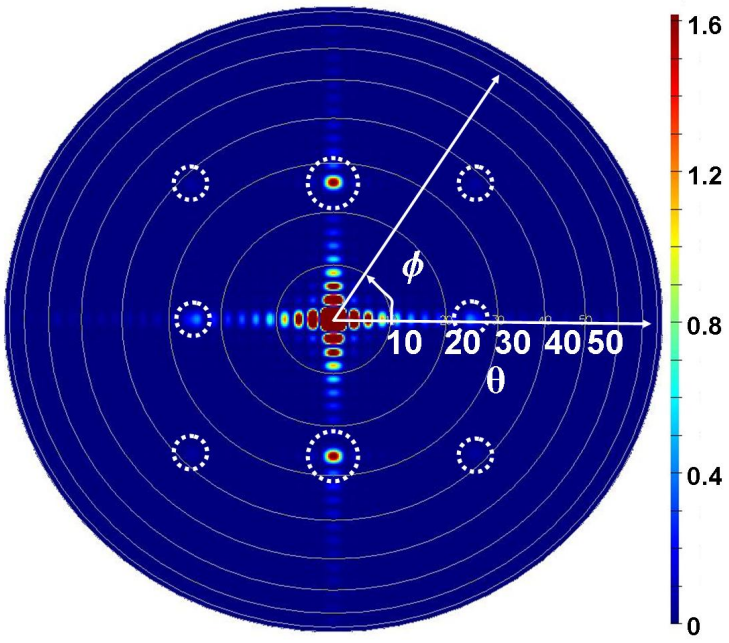

(b)

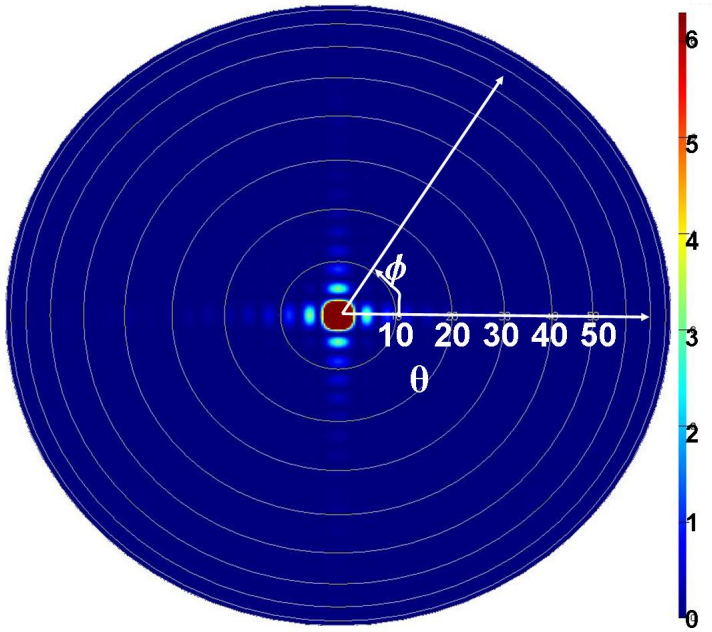

(c)

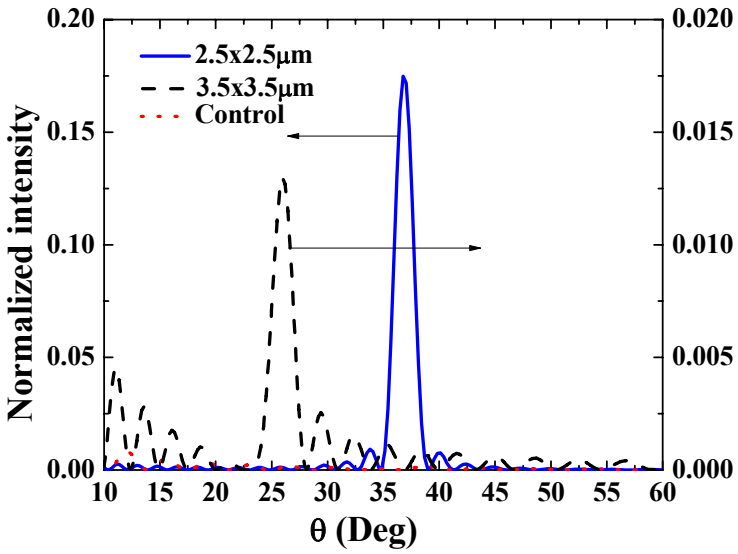

(d)

Figure 4.11 Computed far-field angular spectrum for a combined system of object and nanorods. In (a) to (c) white solid circles indicate constant θ lines, whereas ϕ varies from 0 to 360^0 in counterclockwise direction. White dotted circles are marked to highlight the diffraction orders appearing due to Moiré effect. **(a)** Periodic object grating with lattice

2.5x2.5μm. *Inset:* Schematic illustration of combined system in real space. **(b)** Object grating with lattice 3.5x3.5μm. **(c)** Control case when the incident polarization is perpendicular to the nanorods, resulting in no near-field enhancement. Data presented for object with 2.5x2.5μm lattice. **(d)** Far-field angular spectrum for the above three cases at $\phi = 90^0$. Intensities are normalized to the DC component.

As a control case, we also compute the far-field angular spectrum of the combined system (object + nanorods), when the incident wave has a polarization perpendicular to the nanorods. Since, there is no resonance and enhancement of evanescent field in this case, the Moiré features are not observed in the far-field (Figure 4.11(c), (d)).

It is evident that the far-field angular spectrum is not the real-space image of the object. However, the real-space image can be reconstructed by applying lateral shifts to the frequency components according to grating law and taking inverse Fourier transform. For the case of periodic grating objects, this procedure is almost trivial. However, the imaging itself is not limited to periodic objects and can be extended to generalized shapes, provided a clear one to one relationship is known between the recorded far-field Moiré features and object features.

4.4 Summary

To summarize, we have demonstrated a new approach to realize ultra-smooth Ag superlenses with an unprecedented λ/12 resolution capability at near-UV wavelength. Incorporating few monolayers of Ge drastically improves Ag film quality and minimizes the subwavelength information loss due to scattering. Our theoretical and lithography results clearly indicate subdiffraction imaging down to 30nm half-pitch resolution with 380nm illumination.

We also have demonstrated numerically a far-field imaging technique based on Moiré effect with subdiffraction resolution capability in IR regime. A nanorod substrate was designed that provides near-field enhancement, a necessary precursor to achieve evanescent mixing. By transforming unresolvable high-frequency information of the object into low frequency Moiré features, we are able to observe the subdiffraction

features in the far-field. At incident wavelength of 6μm, Moiré features corresponding to object periodicity of 2.5μm were clearly seen in the far-field. The methodology relies on a prerequisite that an unambiguous reconstruction can be done by a suitable design of metamaterial substrate. The image reconstruction procedure is very simple and requires only Fourier transform and lateral shifts of frequency components. This reconstruction procedure can be completely automated, making real time dynamic imaging of materials, biological cells and tissues with subwavelength resolution a distinct possibility.

Methods

Sample preparation for smooth superlens:

Ag, Ag/Ge samples were prepared on quartz using electron-beam evaporation with deposition rate of 0.1 Å/s for Ge and 1 Å/s for Ag at a pressure of $8x10^{-7}$ torr. The substrate (~1"x1", 1mm thick) were first cleaned using RCA1 solution.[91] Electronic grade source material was supplied by Kurt J. Lesker with a four-nine purity.

Nanoimprint technology:

Nanoimprint technology developed at Hewlett-Packard laboratory was utilized to fabricate 30nm half-pitch Cr gratings and 6nm thick spacer films. First a PMMA (950k/15k) layer with thickness 60nm is spin coated on quartz substrate, followed by spin coating of a UV-resist with thickness 66nm. The UV-resist is imprinted and cured using a mold with 30nm half-pitch gratings. UV-resist layer is then etched to 45nm thickness using RIE (with CF_4: 60 sccm, 2mtorr), followed by through etching of PMMA layer with O_2 RIE (40 sccm, 2mtorr). 40nm thick Cr is deposited using e-beam evaporator at 0.1Å/s, followed by liftoff using acetone and ultrasonic agitation. Planarization of the Cr gratings is performed by spin coating UV-resist with thickness 66nm, followed by imprinting with a flat mold and UV-curing. UV-resist is then etched using CF_4 RIE to a total thickness of 46nm, thus resulting in a spacer layer with 6nm thickness.

XRR measurement:

X-ray reflectivity measurements were carried out on a Philip MRD X'pert system. Measurements were made in a range between 0 and 3 degrees, of which some data points close to zero degree were removed since no useful information is available until the total angle of reflection. Incident angle scan data points were collected with a step width of 0.01 degrees. Theoretical curves were simulated using commercial software Wingixa. Film thickness and density were determined from the period of intensity oscillations and total reflection edge, respectively.

5 SUMMARY, FUTURE WORK AND OUTLOOK

5.1 Summary

This dissertation has dealt with design and characterization of plasmonic metamaterials. We have addressed some of the fascinating applications of metamaterials in realizing new optical devices which are considerably smaller than light wavelength. We have investigated a novel characterization technique specifically suited to probe optical properties of metamaterials at the nanoscale.

After a brief overview of recent advances in the field of optical metamaterials in introduction chapter, we presented an integrated metamaterial modulator for on-fiber data transport and telecommunication applications in Chapter 2. With numerical simulations we demonstrated a double-wire sandwich structure, popularly known as a "fishnet metamaterial", as an effective modulator. We have also investigated a flipped fishnet design that shows promise of being a low-loss and more effective integrated modulator.

Chapter 3 describes scanning electron beam based cathodoluminescence imaging and spectroscopy technique for characterization of plasmonic metamaterials. Both experimental and numerical simulation studies were presented that reveals a coherent picture of excitation of plasmon modes with electron beam. We have conceptualized a new finite-difference time-domain based simulation methodology that models the electron beam as an array of point dipoles. In this chapter we focused on analyzing plasmon modes of silver triangular nanoparticles anchored on a substrate.

In Chapter 4 we discussed the subdiffraction imaging capability of plasmonic systems such as planar silver superlenses and nanorods. We have experimentally demonstrated a resolution capability of $1/12^{th}$ of the illumination wavelength, providing unprecedented image details up to 30nm with near-UV light. This was achieved by carefully minimizing the information losses due to evanescent decay, absorption and scattering due to rough surfaces. Applying the state-of-the-art nanoimprint technology and intermediate wetting layer (germanium) for the growth of silver, we have shown that a smooth superlens could be fabricated with thickness down to 15nm. We have also discussed extending the subdiffraction resolution capability of plasmonic materials to far-

field in infrared regime for chemical sensing applications. By designing a nanorod substrate, we have numerically demonstrated that the evanescent modes from an object can be coupled out to the far-field in the form of Moiré features. A subdiffraction resolution of 2.5μm pitch is demonstrated at 6μm wavelength.

5.2 Future work

This work presents a unique platform to understand the fundamental characteristics of metamaterials and harness the novel physics to develop practical applications. The field of optical metamaterials is relatively new, and there is certainly a huge scope for further development on several aspects presented in this study. Specifically there are certain key directions which we would like to be followed-up:

- Experimental demonstration of integrated fiber modulator, including study of temporal dynamics.
- Exploration of novel plasmon physics of metallic nanostructures with cathodoluminescence spectroscopy, including study of plasmon propagation lengths to distinguish localized vs. traveling plasmon modes. Improving the modeling and numerical simulation methodology by incorporating varying electron velocity, and dispersive or lossy substrates.
- Experimental realization of far-field subdiffraction imaging at infrared wavelengths and developments of efficient image reconstruction algorithms for complex subwavelength structures.

5.3 Outlook

Since the realization of metamaterials first at microwave frequencies, significant improvements in performance have been made possible by new physical insights in device design and better fabrication techniques. However, material losses at optical frequencies remain a key challenge to the wide-scale adoption of metamaterial enabled technologies. For example, current commercial telecommunication switches operate with more than 10dB extinction ratios. While metamaterials offer an opportunity to

significantly reduce the device footprints, further exploration of design optimization to reduce losses and harness other novel nonlinear behavior is desirable. The development of low-loss metamaterials could be the foundation of switches, modulators and other novel optical devices in all-optical integrated information processing architectures, which can process data signals much more efficiently than their electronic counterparts.

In addition, the fundamental understanding of light-matter interaction at small scales is still an area open to debate. The boundary between continuum and quantum mechanical phenomena can be challenged with development of characterization techniques such as cathodoluminescence and electron energy loss spectroscopy. This is critical for development of miniaturized optical devices such as chemical sensors with single molecule detection sensitivity and waveguides to confine and guide electromagnetic signals at nanoscale.

Fabrication of sub-20nm thick smooth silver films is critical for many applications in metamaterials, plasmonics and nanophotonics. This includes realization of multilayer superlenses operating at visible wavelengths. Development of potential low-loss and high resolution superlenses opens the door to exciting applications in nanoscale optical metrology and nanomanufacturing. The ultrahigh resolution capability of far-field superlenses could have a far reaching impact on biomedical imaging and chemical sensing.

Demonstration of novel functionalities and applications at research scale is only the beginning of the road for metamaterials. The control of optical properties at nanoscale and integration of different components remain one of the hardest challenges. Nevertheless, the progress made in metamaterials over a relatively short period of time is phenomenal. The realization of full potential of this new class of materials will have a profound impact on several disciplines including electronics, communication, medical diagnostics, health care, and manufacturing.

REFERENCES

1. The top ten advances in materials science. *Mater. Today* **2008,** *11,* 40-45.
2. Chaturvedi, P.; Hsu, K.; Zhang, S.; Fang, N., New Frontiers of Metamaterials: Design and Fabrication. *MRS Bull.* **2008,** *33,* 915-920.
3. Veselago, V. G., The electrodynamics of substances with simultaneously negative values of ε and μ. *Sov. Phys. Usp.* **1968,** *10,* 509.
4. Shelby, R. A.; Smith, D. R.; Schultz, S., Experimental Verification of a Negative Index of Refraction. *Science* **2001,** *292,* 77-79.
5. Yen, T. J.; Padilla, W. J.; Fang, N.; Vier, D. C.; Smith, D. R.; Pendry, J. B.; Basov, D. N.; Zhang, X., Terahertz magnetic response from artificial materials. *Science* **2004,** *303,* 1494-1496.
6. Smith, D. R.; Pendry, J. B.; Wiltshire, M. C. K., Metamaterials and negative refractive index. *Science* **2004,** *305,* 788-792.
7. Smith, D. R.; Padilla, W. J.; Vier, D. C.; Nemat-Nasser, S. C.; Schultz, S., Composite medium with simultaneously negative permeability and permittivity. *Phys. Rev. Lett.* **2000,** *84,* 4184-4187.
8. Greegor, R. B.; Parazzoli, C. G.; Li, K.; Tanielian, M. H., Origin of dissipative losses in negative index of refraction materials. *Appl. Phys. Lett.* **2003,** *82,* 2356-2358.
9. Fang, N.; Lee, H.; Sun, C.; Zhang, X., Sub-diffraction-limited optical imaging with a silver superlens. *Science* **2005,** *308,* 534-537.
10. Chen, H. S.; Wu, B. I.; Zhang, B.; Kong, J. A., Electromagnetic wave interactions with a metamaterial cloak. *Phys. Rev. Lett.* **2007,** *99,* 063903.
11. Williams, C. R.; Andrews, S. R.; Maier, S. A.; Fernandez-Dominguez, A. I.; Martin Moreno, L.; Garcia-Vidal, F. J., Highly confined guiding of terahertz surface plasmon polaritons on structured metal surfaces. *Nature Photonics* **2008,** *2,* 175-179.
12. Alu, A.; Salandrino, A.; Engheta, N., Negative effective permeability and left-handed materials at optical frequencies. *Optics Express* **2006,** *14,* 1557-1567.
13. Logeeswaran, V. J.; Stameroff, A. N.; Islam, M. S.; Wu, W.; Bratkovsky, A. M.; Kuekes, P. J.; Wang, S. Y.; Williams, R. S., Switching between positive and negative

permeability by photoconductive coupling for modulation of electromagnetic radiation. *Appl. Phys. A: Mater. Sci. Process.* **2007,** *87,* 209-216.

14. Wu, W.; Yu, Z. N.; Wang, S. Y.; Williams, R. S.; Liu, Y. M.; Sun, C.; Zhang, X.; Kim, E.; Shen, Y. R.; Fang, N. X., Midinfrared metamaterials fabricated by nanoimprint lithography. *Appl. Phys. Lett.* **2007,** *90,* 063107.

15. Zhou, J.; Koschny, T.; Kafesaki, M.; Economou, E. N.; Pendry, J. B.; Soukoulis, C. M., Saturation of the magnetic response of split-ring resonators at optical frequencies. *Phys. Rev. Lett.* **2005,** *95,* 223902.

16. Dolling, G.; Enkrich, C.; Wegener, M.; Soukoulis, C. M.; Linden, S., Simultaneous negative phase and group velocity of light in a metamaterial. *Science* **2006,** *312,* 892-894.

17. Lezec, H. J.; Dionne, J. A.; Atwater, H. A., Negative Refraction at Visible Frequencies. *Science* **2007,** *316,* 430-432.

18. Shin, H.; Fan, S. H., All-angle negative refraction for surface plasmon waves using a metal-dielectric-metal structure. *Phys. Rev. Lett.* **2006,** *96,* 073907.

19. Fang, N.; Liu, Z. W.; Yen, T. J.; Zhang, X., Regenerating evanescent waves from a silver superlens. *Optics Express* **2003,** *11,* 682-687.

20. Shalaev, V. M., Optical negative-index metamaterials. *Nature Photonics* **2007,** *1,* 41-48.

21. Ebbesen, T. W.; Lezec, H. J.; Ghaemi, H. F.; Thio, T.; Wolff, P. A., Extraordinary optical transmission through sub-wavelength hole arrays. *Nature* **1998,** *391,* 667-669.

22. Nie, S. M.; Emery, S. R., Probing single molecules and single nanoparticles by surface-enhanced Raman scattering. *Science* **1997,** *275,* 1102-1106.

23. Pendry, J. B.; Martin-Moreno, L.; Garcia-Vidal, F. J., Mimicking surface plasmons with structured surfaces. *Science* **2004,** *305,* 847-848.

24. Pendry, J. B., Negative refraction makes a perfect lens. *Phys. Rev. Lett.* **2000,** *85,* 3966-3969.

25. Ramakrishna, S. A.; Pendry, J. B.; Wiltshire, M. C. K.; Stewart, W. J., Imaging the near field. *J. Mod. Opt.* **2003,** *50,* 1419-1430.

26. Chaturvedi, P.; Fang, N., Molecular scale imaging with a multilayer superlens. In *Mater. Res. Soc. Symp. Proc.*, 2006; Vol. 919, pp 0919-J04-07.

27. Basile, L.; Hawoong, H.; Czoschke, P.; Chiang, T. C., X-ray studies of the growth of smooth Ag films on Ge(111)-c(2 x 8). *Appl. Phys. Lett.* **2004,** *84,* 4995-4997.

28. Pendry, J. B.; Holden, A. J.; Stewart, W. J.; Youngs, I., Extremely low frequency plasmons in metallic mesostructures. *Phys. Rev. Lett.* **1996,** *76,* 4773-4776.

29. Chen, H. T.; Padilla, W. J.; Zide, J. M. O.; Gossard, A. C.; Taylor, A. J.; Averitt, R. D., Active terahertz metamaterial devices. *Nature* **2006,** *444,* 597-600.

30. Chettiar, U. K.; Xiao, S.; Kildishev, A. V.; Cai, W.; Yuan, H. K.; Drachev, V. P.; Shalaev, V. M., Optical Metamagnetism and Negative-index Metamaterials. *MRS Bull.* **2008,** *33,* 921-926.

31. Valentine, J.; Zhang, S.; Zentgraf, T.; Ulin-Avila, E.; Genov, D. A.; Bartal, G.; Zhang, X., Three-dimensional optical metamaterial with a negative refractive index. *Nature* **2008,** *455,* 376-379.

32. Kim, E.; Shen, Y. R.; Wu, W.; Ponizovskaya, E.; Yu, Z.; Bratkovsky, A. M.; Wang, S. Y.; Williams, R. S., Modulation of negative index metamaterials in the near-IR range. *Appl. Phys. Lett.* **2007,** *91,* 173105.

33. Weiland, T.; Schuhmann, R.; Greegor, R. B.; Parazzoli, C. G.; Vetter, A. M.; Smith, D. R.; Vier, D. C.; Schultz, S., Ab initio numerical simulation of left-handed metamaterials: Comparison of calculations and experiments. *J. Appl. Phys.* **2001,** *90,* 5419-5424.

34. Smith, D. R.; Schultz, S.; Markos, P.; Soukoulis, C. M., Determination of effective permittivity and permeability of metamaterials from reflection and transmission coefficients. *Phys. Rev. B* **2002,** *65,* 5.

35. Wu, W.; Kim, E.; Ponizovskaya, E.; Liu, Y.; Yu, Z.; Fang, N.; Shen, Y. R.; Bratkovsky, A. M.; Tong, W.; Sun, C.*, et al.*, Optical metamaterials at near and mid-IR range fabricated by nanoimprint lithography. *Appl. Phys. A: Mater. Sci. Process.* **2007,** *87,* 143-150.

36. Klar, T. A.; Kildishev, A. V.; Drachev, V. P.; Shalaev, V. M., Negative-index metamaterials: going optical. *IEEE J. Sel. Top. Quantum Electron.* **2006,** *12,* 1106-1115.

37. Ponizovskaya, E. V.; Bratkovsky, A. M., Negative index materials with gain media for fast modulation. *Appl. Phys. A: Mater. Sci. Process.* **2009,** *95,* 1137-1142.

38. Zhang, S.; Fan, W.; Panoiu, N. C.; Malloy, K. J.; Osgood, R. M.; Brueck, S. R., Optical negative-index bulk metamaterials consisting of 2D perforated metal-dielectric stacks. *Optics Express* **2006,** *14,* 6778-6787.

39. Schurig, D., Off-normal incidence simulations of metamaterials using FDTD. *International Journal of Numerical Modelling: Electronic Networks, Devices and Fields* **2006,** *19*.

40. http://www.lumerical.com

41. Haes, A. J.; Van Duyne, R. P., A nanoscale optical blosensor: Sensitivity and selectivity of an approach based on the localized surface plasmon resonance spectroscopy of triangular silver nanoparticles. *J. Am. Chem. Soc.* **2002,** *124,* 10596-10604.

42. McFarland, A. D.; Van Duyne, R. P., Single silver nanoparticles as real-time optical sensors with zeptomole sensitivity. *Nano Lett.* **2003,** *3,* 1057-1062.

43. Bharadwaj, P.; Novotny, L., Spectral dependence of single molecule fluorescence enhancement. *Optics Express* **2007,** *15,* 14266-14274.

44. Ishi, T.; Fujikata, J.; Makita, K.; Baba, T.; Ohashi, K., Si nano-photodiode with a surface plasmon antenna. *Japanese Journal of Applied Physics Part 2-Letters & Express Letters* **2005,** *44,* L364-L366.

45. Eftekhari, F.; Gordon, R., Enhanced second harmonic generation from noncentrosymmetric nanohole arrays in a gold film. *IEEE J. Sel. Top. Quantum Electron.* **2008,** *14,* 1552-1558.

46. Kim, S.; Jin, J. H.; Kim, Y. J.; Park, I. Y.; Kim, Y.; Kim, S. W., High-harmonic generation by resonant plasmon field enhancement. *Nature* **2008,** *453,* 757-760.

47. Haes, A. J.; Haynes, C. L.; McFarland, A. D.; Schatz, G. C.; Van Duyne, R. R.; Zou, S. L., Plasmonic materials for surface-enhanced sensing and spectroscopy. *MRS Bull.* **2005,** *30,* 368-375.

48. Yin, L.; Vlasko-Vlasov, V. K.; Rydh, A.; Pearson, J.; Welp, U.; Chang, S. H.; Gray, S. K.; Schatz, G. C.; Brown, D. B.; Kimball, C. W., Surface plasmons at single nanoholes in Au films. *Appl. Phys. Lett.* **2004,** *85,* 467-469.

49. Nelayah, J.; Kociak, M.; Stephan, O.; de Abajo, F. J. G.; Tence, M.; Henrard, L.; Taverna, D.; Pastoriza-Santos, I.; Liz-Marzan, L. M.; Colliex, C., Mapping surface plasmons on a single metallic nanoparticle. *Nature Physics* **2007,** *3,* 348-353.

50. Gomez-Medina, R.; Yamamoto, N.; Nakano, M.; Abajo, F. J. G., Mapping plasmons in nanoantennas via cathodoluminescence. *New J. Phys.* **2008,** *10,* 105009.
51. Hofmann, C. E.; Vesseur, E. J. R.; Sweatlock, L. A.; Lezec, H. J.; Garcia de Abajo, F. J.; Polman, A.; Atwater, H. A., Plasmonic modes of annular nanoresonators imaged by spectrally resolved cathodoluminescence. *Nano Lett.* **2007,** *7,* 3612-3617.
52. Yamamoto, N.; Araya, K.; de Abajo, F. J. G., Photon emission from silver particles induced by a high-energy electron beam. *Phys. Rev. B* **2001,** *64,* 205419.
53. Yamamoto, N.; Nakano, M.; Suzuki, T., Light emission by surface plasmons on nanostructures of metal surfaces induced by high-energy electron beams. *Surf. Interface Anal.* **2006,** *38,* 1725-1730.
54. Cibert, J.; Petroff, P. M.; Dolan, G. J.; Pearton, S. J.; Gossard, A. C.; English, J. H., Optically detected carrier confinement to one and zero dimension in GaAs quantum well wires and boxes. *Appl. Phys. Lett.* **1986,** *49,* 1275-1277.
55. Chichibu, S.; Wada, K.; Nakamura, S., Spatially resolved cathodoluminescence spectra of InGaN quantum wells. *Appl. Phys. Lett.* **1997,** *71,* 2346-2348.
56. Leon, R.; Petroff, P. M.; Leonard, D.; Fafard, S., Spatially Resolved Visible Luminescence of Self-Assembled Semiconductor Quantum Dots. *Science* **1995,** *267,* 1966-1968.
57. Rodriguez-Viejo, J.; Jensen, K. F.; Mattoussi, H.; Michel, J.; Dabbousi, B. O.; Bawendi, M. G., Cathodoluminescence and photoluminescence of highly luminescent CdSe/ZnS quantum dot composites. *Appl. Phys. Lett.* **1997,** *70,* 2132-2134.
58. García de Abajo, F. J.; Howie, A., Relativistic Electron Energy Loss and Electron-Induced Photon Emission in Inhomogeneous Dielectrics. *Phys. Rev. Lett.* **1998,** *80,* 5180.
59. Haynes, C. L.; Van Duyne, R. P., Plasmon-sampled surface-enhanced Raman excitation spectroscopy. *J. Phys. Chem. B* **2003,** *107,* 7426-7433.
60. McFarland, A. D.; Young, M. A.; Dieringer, J. A.; Van Duyne, R. P., Wavelength-scanned surface-enhanced Raman excitation spectroscopy. *J. Phys. Chem. B* **2005,** *109,* 11279-11285.
61. Shuford, K. L.; Ratner, M. A.; Schatz, G. C., Multipolar excitation in triangular nanoprisms. *J. Chem. Phys.* **2005,** *123,* 114713.

62. Hao, E.; Schatz, G. C., Electromagnetic fields around silver nanoparticles and dimers. *J. Chem. Phys.* **2004,** *120,* 357-366.

63. Martin, O. J. F., Plasmon Resonances in Nanowires with a Non-regular Cross-Section. In *Optical Nanotechnologies*, Tominaga, J.; Tsai, D. P., Eds. Springer-Verlag: Berlin Heidelberg, 2003; pp 183-210.

64. Nelayah, J.; Gu, L.; Sigle, W.; Koch, C. T.; Pastoriza-Santos, I.; Liz-Marzán, L. M.; van Aken, P. A., Direct imaging of surface plasmon resonances on single triangular silver nanoprisms at optical wavelength using low-loss EFTEM imaging. *Opt. Lett.* **2009,** *34,* 1003-1005.

65. Rang, M.; Jones, A. C.; Zhou, F.; Li, Z. Y.; Wiley, B. J.; Xia, Y. N.; Raschke, M. B., Optical Near-Field Mapping of Plasmonic Nanoprisms. *Nano Lett.* **2008,** *8,* 3357-3363.

66. Raether, H., *Surface-Plasmons on Smooth and Rough Surfaces and on Gratings*. 1988; Vol. 111, p 1-133.

67. Garcia de Abajo, F. J.; Kociak, M., Probing the photonic local density of states with electron energy loss spectroscopy. *Phys. Rev. Lett.* **2008,** *100,* 106804.

68. Johnson, P. B.; Christy, R. W., Optical constants of noble metals. *Phys. Rev. B* **1972,** *6,* 4370-4379.

69. Sherry, L. J.; Jin, R. C.; Mirkin, C. A.; Schatz, G. C.; Van Duyne, R. P., Localized surface plasmon resonance spectroscopy of single silver triangular nanoprisms. *Nano Lett.* **2006,** *6,* 2060-2065.

70. Hsu, K. H.; Schultz, P. L.; Ferreira, P. M.; Fang, N. X., Electrochemical Nanoimprinting with Solid-State Superionic Stamps. *Nano Lett.* **2007,** *7,* 446-451.

71. Palik, E. D., *Handbook of optical constants*. 1984; Vol. 1.

72. Fang, N. Engineering Subwavelength Photonic Meta Structures and Devices. PhD thesis, 2004.

73. Lee, H.; Xiong, Y.; Fang, N.; Srituravanich, W.; Durant, S.; Ambati, M.; Sun, C.; Zhang, X., Realization of optical superlens imaging below the diffraction limit. *New J. Phys.* **2005,** *7,* 255.

74. Logeeswaran, V. J.; Chan, M. L.; Bayam, Y.; Saif Islam, M.; Horsley, D. A.; Li, X.; Wu, W.; Wang, S. Y.; Williams, R. S., Ultra-smooth metal surfaces generated by

pressure-induced surface deformation of thin metal films. *Appl. Phys. A: Mater. Sci. Process.* **2007,** *87,* 187-192.

75. Logeeswaran, V. J.; Kobayashi, N. P.; Islam, M. S.; Wu, W.; Chaturvedi, P.; Fang, N. X.; Wang, S. Y.; Williams, R. S., Ultrasmooth Silver Thin Films Deposited with a Germanium Nucleation Layer. *Nano Lett.* **2009,** *9,* 178-182.

76. Heavens, O. S., *Optical Properties of Thin Solid Films*. Dover: New York, 1991.

77. Madou, M. J., *Fundamentals of Microfabrication, Chapter 1*. 2nd ed.; CRC Press: 2002.

78. Taubner, T.; Korobkin, D.; Urzhumov, Y.; Shvets, G.; Hillenbrand, R., Near-Field Microscopy Through a SiC Superlens. *Science* **2006,** *313,* 1595.

79. Liu, Z.; Durant, S.; Lee, H.; Pikus, Y.; Fang, N.; Xiong, Y.; Sun, C.; Zhang, X., Far-Field Optical Superlens. *Nano Lett.* **2007,** *7,* 403-408.

80. Jacob, Z.; Alekseyev, L. V.; Narimanov, E., Optical Hyperlens: Far-field imaging beyond the diffraction limit. *Optics Express* **2006,** *14,* 8247-8256.

81. Alessandro, S.; Nader, E., Far-field subdiffraction optical microscopy using metamaterial crystals: Theory and simulations. *Phys. Rev. B* **2006,** *74,* 075103.

82. Liu, Z. W.; Lee, H.; Xiong, Y.; Sun, C.; Zhang, X., Far-field optical hyperlens magnifying sub-diffraction-limited objects. *Science* **2007,** *315,* 1686-1686.

83. Smolyaninov, I. I.; Hung, Y.-J.; Davis, C. C., Magnifying Superlens in the Visible Frequency Range. *Science* **2007,** *315,* 1699-1701.

84. Liu, Z. W.; Durant, S.; Lee, H.; Xiong, Y.; Pikus, Y.; Sun, C.; Zhang, X., Near-field Moire effect mediated by surface plasmon polariton excitation. *Opt. Lett.* **2007,** *32,* 629-631.

85. Flanders, D. C.; Smith, H. I.; Austin, S., New Interferometric Alignment Technique. *Appl. Phys. Lett.* **1977,** *31,* 426-428.

86. Grimm, M. A.; Lohmann, A. W., Superresolution Image for One-Dimensional Objects. *J. Opt. Soc. Am.* **1966,** *56,* 1151-1156.

87. Durant, S.; Liu, Z. W.; Steele, J. A.; Zhang, X., Theory of the transmission properties of an optical far-field superlens for imaging beyond the diffraction limit. *J. Opt. Soc. Am. B* **2006,** *23,* 2383-2392.

88. Neubrech, F.; Kolb, T.; Lovrincic, R.; Fahsold, G.; Pucci, A.; Aizpurua, J.; Cornelius, T. W.; Toimil-Molares, M. E.; Neumann, R.; Karim, S., Resonances of individual metal nanowires in the infrared. *Appl. Phys. Lett.* **2006,** *89,* 253104-3.
89. Neubrech, F.; Pucci, A.; Cornelius, T. W.; Karim, S.; Garcia-Etxarri, A.; Aizpurua, J., Resonant Plasmonic and Vibrational Coupling in a Tailored Nanoantenna for Infrared Detection. *Phys. Rev. Lett.* **2008,** *101,* 157403-4.
90. Mandel, L.; Wolf, E., *Optical coherence and Quantum Optics*. Cambridge University Press: 1995.
91. Kern, W., *Handbook of Semiconductor Cleaning Technology*. Noyes Publishing: Park Ridge, NJ, 1993.

AUTHOR'S BIOGRAPHY

Pratik Chaturvedi was born on June 26th, 1983 in Madhya Pradesh, India. He received his B.Tech. degree in Mechanical Engineering from the Indian Institute of Technology (IIT) Bombay, Mumbai, India in 2004. Pratik then joined Department of Mechanical Engineering at University of Illinois, Urbana-Champaign in fall 2004. He worked with Prof. Nicholas Fang in the area of Nanoplasmonics and graduated with his M.S. in 2006. Pratik then continued with graduate studies towards Ph.D. degree under the guidance of Prof. Fang. His research has focused on design and characterization of optical metamaterials and has resulted in several conference presentations and journal publications including in MRS Bulletin and Nano Letters. Two of his papers are currently under consideration for publication in Nano Letters and ACS Nano. After receiving his Ph.D., Pratik will join Intel Corporation in Portland, Oregon as senior R&D process engineer.